Analysis and Synthesis of Collaborative Opportunistic Navigation Systems

by

Zaher Kassas, B.E.; M.S.; M.S.E.

DISSERTATION

Presented to the Faculty of the Graduate School of

The University of Texas at Austin

in Partial Fulfillment

of the Requirements

for the Degree of

DOCTOR OF PHILOSOPHY

THE UNIVERSITY OF TEXAS AT AUSTIN

May 2014

The Dissertation Committee for Zaher Kassas
certifies that this is the approved version of the following dissertation:

Analysis and Synthesis of Collaborative Opportunistic Navigation Systems

Committee:

Todd E. Humphreys, Supervisor

Ari Arapostathis, Supervisor

Maruthi Akella

Constantine Caramanis

Brian L. Evans

Dedicated to anyone who got lost and could not find the way home

Acknowledgments

I would like to express my gratitude to a number of people who played a role in my academic journey. First, I thank my advisor Todd Humphreys for his advice and support throughout my doctoral studies. I still remember vividly our first meeting in which he discussed his research vision. I thank him for introducing me to such a captivating field of research and for giving me the freedom to pursue the various intriguing problems of my dissertation.

I also thank my co-advisor Ari Arapostathis for his advice during my M.S.E. and Ph.D. studies. I enjoyed each and every research meeting with him, which have often branched to discussing topics in science, philosophy, and politics. I have learned a great deal from his deep mathematical insight and his approach in formulating fundamental research questions.

I thank my Ph.D. committee members for taking time to serve on my committee. I thank Brian Evans for being an outstanding mentor throughout my academic journey. I thank Maruthi Akella who taught me the Nonlinear Dynamics and Adaptive Control course, which was the most engaging controls course I have taken in my graduate studies. I thank Constantine Caramanis from whom I learned how to tackle any problem through mathematical fundamentals exclusively.

I thank Ahmed Tewfik, Gustavo de Veciana, and Behcet Acikmese for

their advice and support during my faculty search.

I appreciate the generous research funding provided by National Instruments Corp., Boeing Advanced Network and Space Systems, National Science Foundation, Harris Corp., and Northrop Grumman Electronic Systems.

I thank my research colleagues at the UT Radionavigation Laboratory: Kyle Wesson for all the coffee break chats; Jahshan Bhatti for the numerous white board discussions; Ken Pesyna for the Iridium research collaboration; and Daniel Shepard, Andrew Kerns, and Shubhodeep (Deep) Mukherji.

I thank my undergraduate advisor Samer Saab for introducing me to the fascinating world of GPS and for his encouragement and support. I thank my M.S. advisor Ümit Özgüner and my M.S.E. advisor Robert Bishop for supervising my studies and for being role models in academic excellence.

I thank my friend Garo Zarikian for his motivation for the past decade.

I thank my family: dad, mom, Mariam, Ali, Bachir, and Sara for their continuous encouragement and support throughout my long academic journey. My father never pursued a graduate education due to extenuating circumstances. However, he provided me with the financial and more importantly the emotional support to pursue such education.

Lastly, but very importantly, I thank the intelligent, beautiful, encouraging, and loving Zeina. She has been my biggest fan throughout my doctoral journey. I have not said this enough: none of this would have been possible without her support.

Analysis and Synthesis of Collaborative Opportunistic Navigation Systems

Publication No. _____

Zaher Kassas, Ph.D.
The University of Texas at Austin, 2014

Supervisors: Todd E. Humphreys
Ari Arapostathis

Navigation is an invisible utility that is often taken for granted with considerable societal and economic impacts. Not only is navigation essential to our modern life, but the more it advances, the more possibilities are created. Navigation is at the heart of three emerging fields: autonomous vehicles, location-based services, and intelligent transportation systems.

Global navigation satellite systems (GNSS) are insufficient for reliable anytime, anywhere navigation, particularly indoors, in deep urban canyons, and in environments under malicious attacks (e.g., jamming and spoofing). The conventional approach to overcome the limitations of GNSS-based navigation is to couple GNSS receivers with dead reckoning sensors. A new paradigm, termed opportunistic navigation (OpNav), is emerging. OpNav is analogous to how living creatures naturally navigate: by learning their environment. OpNav aims to exploit the plenitude of ambient radio frequency signals of

opportunity (SOPs) in the environment. OpNav radio receivers, which may be handheld or vehicle-mounted, continuously search for opportune signals from which to draw position and timing information, employing on-the-fly signal characterization as necessary. In collaborative opportunistic navigation (COpNav), multiple receivers share information to construct and continuously refine a global signal landscape.

For the sake of motivation, consider the following problem. A number of receivers with no *a priori* knowledge about their own states are dropped in an environment comprising multiple unknown terrestrial SOPs. The receivers draw pseudorange observations from the SOPs. The receivers' objective is to build a high-fidelity signal landscape map of the environment within which they localize themselves in space and time. We then ask: (*i*) Under what conditions is the environment fully observable? (*ii*) In cases where the environment is not fully observable, what are the observable states? (*iii*) How would receiver-controlled maneuvers affect observability? (*iv*) What is the degree of observability of the various states in the environment? (*v*) What motion planning strategy should the receivers employ for optimal information gathering? (*vi*) How effective are receding horizon strategies over greedy for receiver trajectory optimization, and what are their limitations? (*vii*) What level of collaboration between the receivers achieves a minimal price of anarchy?

This dissertation addresses these fundamental questions and validates the theoretical conclusions numerically and experimentally.

Table of Contents

List of Tables

List of Figures

Chapter 1

Introduction

Where am I? Where am I heading? How long will I take to reach my desired destination? These are probably the first questions that puzzled mankind since we found ourselves on this planet. Position determination has been always associated with the concept of navigation. Navigation is defined as the art and science of directing the movement of a person or a craft expeditiously and safely from one point to another. The close relationship between navigation and position determination is attributed to the navigator's need to know the position and velocity at all times in order to steer safely and correctly from one place to another.

1.1 Future Navigation Systems

Not only is navigation essential to our modern life, but the more it advances, the more possibilities are created. Imagine a world in which humans and autonomous vehicles could navigate anytime, anywhere reliably and accurately. In such a world, emergency responders, whether humans or autonomous robots, could navigate hazardous environments, such as buildings after earthquakes or explosions, to perform rescue missions. In such a world,

people could find the most efficient course to navigate any indoor environment, such as airports, hospitals, shopping malls, and campus buildings. In such a world, humans do not have to drive their vehicles anymore, since they could request their own autonomous chauffeur. By tapping their smartphone, the closest autonomous vehicle is directed to the requester's location for pick-up, and later drops-off the requester at the desired destination. During the ride, the requester could relax or perform some productive activity, knowing that the autonomous vehicle is taking the safest and most efficient route. A futuristic Volkswagen (VW) concept autonomous vehicle is illustrated in Figure 1.1. All of this, and more, can only be made possible with the realization of reliable and accurate anytime, anywhere navigation.

Figure 1.1: Futuristic VW concept autonomous vehicle

1.2 Evolution of Navigation Systems

Navigation has come a long way since the days when the Phoenician and Greek traders surfed the Mediterranean Sea and beyond using basic navigational techniques to travel from one port to another. Over the years, various tools were developed to provide more accurate navigational information. By the mid-eighteenth century, astronomical observations with a sextant and a chronometer could establish a ship's position to within a few kilometers. In the twentieth century, refined maps and charts were produced. In addition, radio positioning systems (e.g., Loran-C) as well as electronic navigation systems, such as inertial navigation systems (INS) comprising a computer, motion sensors (e.g., accelerometers), and rotation sensors (e.g., gyroscopes), were developed [1].

From a navigation perspective, the most significant achievement has been the development of the global positioning system (GPS) by the United States Department of Defense in 1973. GPS revolutionized position determination over land, sea, air, and even space. The system with its global coverage is available 24 hours a day every day, providing the navigator with a highly accurate tool, which operates in all weather conditions. The receiver, on the other hand, is compact and relatively inexpensive, allowing its use by anyone from a hiker to an airplane pilot. The GPS also inspired the development of other satellite-based navigation systems, such as the Russian Globalnaya Navigatsionnaya Sputnikovaya Sistema (GLONASS), the European Galileo, and the Chinese Beidou (Compass).

1.3 GNSS Impact

Global navigation satellite system (GNSS) is an invisible utility that is often taken for granted. The aviation, shipping, agriculture, and transportation industries need GNSS to function. The telecommunications, energy, and financial markets depend on GNSS for precision timing and synchronization [2–4]. GNSS has considerable societal and economic impacts. The European Commission determined that close to $1T of the European economy to be dependent on precision navigation or timing from GPS [5]. The European GNSS Agency (GSA) predicted that GNSS-enabled devices will reach 7B devices worldwide by 2022– almost one for every person on the planet [6]. Location-based services (LBS) worldwide market, which is driven by applications like mapping, public safety, discovery and infotainment, location analytics, location-based advertising, social networking, tracking, and augmented reality and gaming is expected to grow to close to $40B by 2019 [7].

1.4 GNSS Limitations

Despite the extraordinary advances in GNSS technology, the weakness of their space-based signals renders GNSS insufficient for reliable and accurate anytime, anywhere navigation, particulary indoors, in deep urban canyons, and in environments under malicious attacks (e.g., jamming and spoofing).

1.4.1 Navigation in Indoors Environments

In outdoor GNSS working conditions, typical values of carrier-to-noise ratios $C/N_0 \geq 44$ dB-Hz are commonly encountered. For indoor scenarios, and depending on the building materials and the receiver location within the building, attenuation losses ranging from tens to more than 40 dB can be experienced [8]. At such low C/N_0, GNSS receivers may not acquire nor track GNSS signals, and subsequently may not produce a navigation solution. This is particulary problematic for emergency responders as more than 70% of E911 calls originate indoors [9].

1.4.2 Navigation in Deep Urban Canyons

A recent study demonstrated that less than 50% of Hong Kong's dense urban environment to have GPS coverage [10]. This is problematic for future intelligent transportation systems (ITS), which require reliable, consistent, tamper-proof, and highly accurate positioning for vehicle-to-vehicle (V2V) communication protocols [11].

1.4.3 Navigation in Environments Under Malicious Attacks

In 2009, a truck driver who had installed a GPS jammer on his truck and traveled along the nearby New Jersey Turnpike (I-95) caused brief daily breaks in reception in the navigation system at Newark Liberty International Airport (EWR) [12]. In addition, civilian GNSS signals are unencrypted, unauthenticated, and specified in publicly-available documents [13]. In 2012,

The University of Texas at Austin Radionavigation Laboratory demonstrated a spoofing attack on an unmanned aerial vehicle (UAV), in which counterfeit GNSS signals were generated for the purpose of manipulating the UAV's reported position, velocity, and time [14].

1.5 Integrated Navigation Systems

The most common approach to overcome the limitation of GNSS-based navigation is to integrate GNSS receivers with dead-reckoning systems. These integrated navigation systems typically use a fusion of multiple, heterogeneous sensors, in particular, GNSS receivers, INS, digital map databases, and different signal processing algorithms [15–18]. Such integration assumes a fixed number of well-modeled sensors, which are fused together through a nonlinear estimator [19, 20]. Current trends in integrated navigation systems include vision-based navigation [21], map- and power-matching [22–25], three-dimensional mapping [26], opportunism [27, 28], and collaboration [29–31].

1.6 Collaborative Opportunistic Navigation

Motivated by the plenitude of ambient radio frequency signals in GNSS-challenged environments, a new paradigm to overcome the limitations of GNSS-based navigation is emerging. This paradigm, termed opportunistic navigation (OpNav), is analogous to how living creatures naturally navigate: by learning their environment. OpNav radio receivers exploit ambient radio frequency signals of opportunity (SOPs) from which they draw navigation and timing

information, employing on-the-fly signal characterization as necessary [32]. Signals from discovered SOPs are downmixed and sampled coherently, yielding a tight coupling between signal streams that permits carrier-phase-level fusion of observables from the various streams within a single or distributed state estimator. SOPs include cellular phone signals [32–36], television signals [37, 38], AM/FM radio signals [39, 40], WiFi signals [41, 42], Iridium satellite signals [43, 44], XM$^{\text{TM}}$ satellite signals [45], ultra-wideband (UWB) orthogonal frequency division multiplexed (OFDM) radar signals [46], and light-emitting diode (LED) signals [47, 48]. In collaborative opportunistic navigation (COpNav), multiple OpNav receivers share information to construct and continuously refine a global signal landscape within which the receivers localize themselves in space and time [49]. Figure 1.2 illustrates a system-level vision of COpNav, in which receivers on a UAV, an unmanned ground vehicle (UGV), and in a handheld device share their observations of various SOPs over a communications network. The shared data is processed at a cloud-hosted signal landscape map database and a fusion center, whose role is to maintain the signal landscape map. Information is fed-back from the fusion center to aid signal tracking at each receiver.

The GPS control segment routinely solves an instance of the COpNav problem: the location and timing offsets of GPS ground stations are simultaneously estimated with orbital and clock parameters of GPS satellites [50]. Compared to the general COpNav problem, the GPS control segment's problem enjoys the constraints imposed by accurate prior estimates of site locations

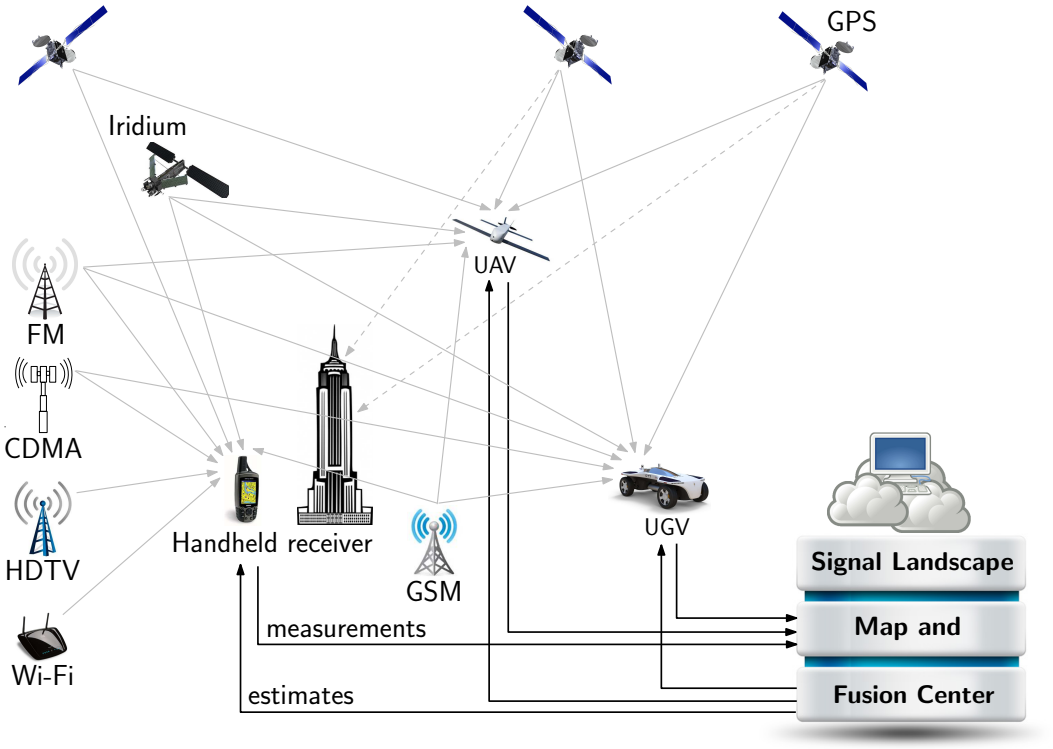

Figure 1.2: A system-level vision of COpNav

and satellite orbits. Moreover, estimation of clock states is aided by the presence of highly-stable atomic clocks in the satellites and at each ground station. In contrast, a COpNav receiver entering a new signal landscape may have less prior information and cannot assume atomic frequency references for itself or for the SOPs. The GPS control segment example highlights the essentially collaborative nature of COpNav.

1.7 OpNav–SLAM Analogy

In its most general form, OpNav treats all ambient signals as potential SOPs, from conventional GNSS signals to communications signals never intended for use as timing or positioning sources. Each signal's relative timing and frequency offsets, transmit location, and frequency stability, are estimated on-the-fly as necessary, with prior information exploited when available. At this level of generality, the OpNav estimation problem is similar to the so-called simultaneous localization and mapping (SLAM) problem in robotics [51, 52]. Both imagine an agent which, starting with incomplete knowledge of its location and surroundings, simultaneously builds a map of its environment and locates itself within that map.

In traditional SLAM, the map that gets constructed as the agent (typically a robot) moves through the environment is composed of landmarks (e.g., walls, posts, etc) with associated positions. OpNav extends this concept to radio frequency signals, with SOPs playing the role of landmarks [53]. In contrast to a SLAM map [54, 55], the OpNav signal landscape is dynamic and more complex. For the case of pseudorange-only OpNav, where observables consist solely of signal time-of-arrival measurements, one must estimate, besides the position and velocity of each SOP transmitter's antenna phase center, each SOP's time offset, rate of change of time offset, and some parameters that characterize the SOP's reference oscillator stability. Even more SOP parameters are required if both pseudorange and carrier phase measurements are ingested into the estimator [32]. In addition to the SOP states, the OpNav

receiver's own position, velocity, clock bias, and clock drift must be estimated. Metaphorically, the signal landscape map can be thought of as a "jello map," with the jello firmer as the oscillators are more stable.

1.8 Dissertation Contributions

The ideas in SOP-based navigation have been inchoate. This dissertation formulates the theoretical framework and answerers fundamental analysis and synthesis questions pertaining to COpNav. Two classes of problems are tackled in this dissertation: (*i*) observability and estimability analyses and (*ii*) motion planning for optimal information gathering. Below is a list of questions this dissertation addresses.

Observability and estimability analyses

1. Under what conditions is a COpNav environment comprising multiple receivers and multiple SOPs fully-observable?
2. For cases where the environment is not fully-observable, what are the observable states, if any?
3. How do receiver-controlled maneuvers affect COpNav observability?
4. What is the degree of observability, also known as estimability, of the various states in the COpNav environment?

Motion planning for optimal information gathering

1. What metric is appropriate for optimizing the receiver's motion for optimal information gathering?
2. What convexity properties can be stated for the receiver motion planning optimization problems?
3. What is the level of superiority of receding horizon, i.e., multi-step look-ahead, motion strategies over greedy, i.e., one-step look-ahead, strategies, and what are the limitations of such superiority?
4. What decision making and information fusion architecture achieves a minimal price of anarchy in collaborative signal landscape mapping with multiple receivers?

The refereed publications resulting from this dissertation are given next.

Journal Publications

[J1] Kassas, Z., & Humphreys, T. (2014). Observability analysis of collaborative opportunistic navigation with pseudorange measurements. *IEEE Transactions on Intelligent Transportation Systems*, (15)1, 260–273.

[J2] Kassas, Z., & Humphreys, T. (2014). Receding horizon trajectory optimization in opportunistic navigation environments. *IEEE Transactions on Aerospace and Electronic Systems*, submitted.

[J3] Kassas, Z., Arapostathis, A., & Humphreys, T. (2014). Greedy motion planning for simultaneous signal landscape mapping and receiver localization. *IEEE Journal of Selected Topics in Signal Processing*, submitted.

Conference Publications

[C1] Kassas, Z., & Humphreys, T. (2012). Observability analysis of opportunistic navigation with pseudorange measurements. *Proceedings of AIAA Guidance, Navigation, and Control Conference* (pp. 4760–4775). Minneapolis, MN.

[C2] Kassas, Z., & Humphreys, T. (2012). Observability and estimability of collaborative opportunistic navigation with pseudorange measurements. *Proceedings of ION Global Navigation Satellite Systems Conference* (pp. 621–630). Nashville, TN.

[C3] Kassas, Z., & Humphreys, T. (2013). Motion planning for optimal information gathering in opportunistic navigation systems. *Proceedings of AIAA Guidance, Navigation, and Control Conference* (pp. 4551-4565). Boston, MA.

[C4] Kassas, Z., Bhatti, J., & Humphreys, T. (2013). Receding horizon trajectory optimization for simultaneous signal landscape mapping and receiver localization. *Proceedings of ION Global Navigation Satellite Systems Conference* (pp. 1962–1969). Nashville, TN.

[C5] Kassas, Z., & Humphreys, T. (2013). The price of anarchy in active signal landscape map building. *Proceedings of IEEE Global Conference on Signal and Information Processing* (pp. 165–168). Austin, TX.

[C6] Kassas, Z., Bhatti, J., & Humphreys, T. (2013). A graphical approach to GPS software-defined receiver implementation. *Proceedings of IEEE Global Conference on Signal and Information Processing* (pp. 1226–1229). Austin, TX.

Magazine Publications

[M1] Kassas, Z. (2013, June). Collaborative opportunistic navigation. *IEEE Aerospace and Electronic Systems Magazine*, (28)6, 38–41.

1.9 Dissertation Outline

This dissertation is organized as follows.

Chapter 2: This chapter presents the receiver and SOP dynamical model as well as the model of observations made by a receiver on an SOP.

Chapter 3: This chapter analyzes the observability of a number of scenarios that a typical COpNav environment could exhibit. Subsequently, the minimal conditions under which the COpNav environment is fully-observable are established. For cases where the environment is not fully-observable, the observable states are specified. Moreover, the effects of allowing receiver-controlled maneuvers on observability are studied. In addition, the degree of observability (estimability) of the various environment states is assessed with particular attention paid to the most and least observable directions in the state space. The theoretical con-

clusions are validated via numerical simulations and an experimental demonstration.

Chapter 4: This chapter synthesizes receiver motion planning algorithms for optimal information gathering in COpNav environments. To this end, several classical information-based optimization criteria are derived and novel innovation-based optimization criteria are proposed. The performance of information-based and innovation-based criteria are compared analytically and numerically. Moreover, it is shown that the innovation-based criteria possess strong convexity properties making the solutions of their associated optimization problems computationally efficient. In addition, the superiority and limitations of receding horizon motion planning strategies over greedy are assessed. Finally, collaborative signal landscape mapping with multiple receivers is studied, and several decision making and information fusion architectures are synthesized. It is demonstrated that a hierarchical strategy achieves a minimal price of anarchy.

Chapter 5: This chapter summarizes the contributions of this dissertation and highlights the major discoveries.

Chapter 6: This chapter outlines a number of future research directions that build upon this dissertation.

Chapter 2

Collaborative Opportunistic Navigation Environment Model Description

This chapter describes the COpNav environment model. Section 2.1 presents the receiver and SOP dynamical model, whereas Section 2.2 specifies the model of the pseudorange observations made by a receiver on an SOP.

2.1 Dynamics Model

2.1.1 Clock Dynamics Model

The receiver and SOP clock error dynamics will be modeled according to the two-state model composed of the clock bias δt and clock drift $\dot{\delta t}$, as depicted in Figure 2.1. The clock error states evolve according to

$$\dot{\boldsymbol{x}}_{\text{clk}}(t) = \mathbf{A}_{\text{clk}}\, \boldsymbol{x}_{\text{clk}}(t) + \tilde{\boldsymbol{w}}_{\text{clk}}(t),$$

$$\boldsymbol{x}_{\text{clk}} = \begin{bmatrix} \delta t \\ \dot{\delta t} \end{bmatrix}, \quad \tilde{\boldsymbol{w}}_{\text{clk}} = \begin{bmatrix} \tilde{w}_{\delta t} \\ \tilde{w}_{\dot{\delta t}} \end{bmatrix}, \quad \mathbf{A}_{\text{clk}} = \begin{bmatrix} 0 & 1 \\ 0 & 0 \end{bmatrix},$$

where the elements of $\tilde{\boldsymbol{w}}_{\text{clk}}$ are modeled as zero-mean, mutually independent white noise processes and the power spectral density of $\tilde{\boldsymbol{w}}_{\text{clk}}$ is given by $\tilde{\mathbf{Q}}_{\text{clk}} = \text{diag}\left[S_{\tilde{w}_{\delta t}}, S_{\tilde{w}_{\dot{\delta t}}}\right]$. The power spectra $S_{\tilde{w}_{\delta t}}$ and $S_{\tilde{w}_{\dot{\delta t}}}$ can be related to the power-law coefficients $\{h_\alpha\}_{\alpha=-2}^{2}$, which have been shown through laboratory experiments to be adequate to characterize the power spectral density of

the fractional frequency deviation $y(t)$ of an oscillator from nominal frequency, which takes the form $S_y(f) = \sum_{\alpha=-2}^{2} h_\alpha f^\alpha$ [56, 57]. It is common to approximate the clock error dynamics by considering only the frequency random walk coefficient h_{-2} and the white frequency coefficient h_0, which lead to $S_{\tilde{w}_{\delta t}} \approx \frac{h_0}{2}$ and $S_{\tilde{w}_{\dot{\delta} t}} \approx 2\pi^2 h_{-2}$ [58, 59].

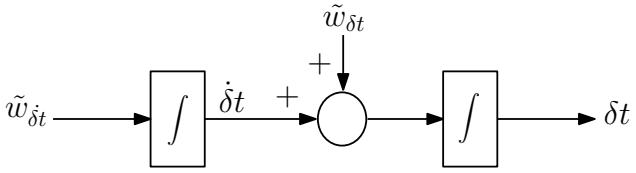

Figure 2.1: Clock error states dynamical model

2.1.2 Receiver Dynamics Model

The receiver's position and velocity will be assumed to evolve according to a controlled velocity random walk dynamics. An object moving as such in a generic coordinate ξ has the dynamics

$$\ddot{\xi}(t) = u_\xi(t) + \tilde{w}_\xi(t),$$

where u_ξ is the control input in the form of an acceleration command and $\tilde{w}_\xi$ is a zero-mean white noise process with power spectral density $\tilde{q}_\xi$, i.e.,

$$\mathbb{E}\left[\tilde{w}_\xi(t)\right] = 0, \quad \mathbb{E}\left[\tilde{w}_\xi(t)\tilde{w}_\xi(\tau)\right] = \tilde{q}_\xi\, \delta(t-\tau),$$

where $\delta(t)$ is the Dirac delta function. Note that in the absence of the control input, the above model reduces to a velocity random walk.

The receiver's state vector will be defined by augmenting the receiver's planar position $\boldsymbol{r}_r$ and velocity $\dot{\boldsymbol{r}}_r$ with its clock error states $\boldsymbol{x}_{\text{clk},r}$ to yield the continuous-time (CT) state space realization

$$\dot{\boldsymbol{x}}_r(t) = \mathbf{A}_r\, \boldsymbol{x}_r(t) + \mathbf{B}_r\, \boldsymbol{u}_r(t) + \mathbf{D}_r\, \tilde{\boldsymbol{w}}_r(t), \tag{2.1}$$

where $\boldsymbol{x}_r = \left[\boldsymbol{r}_r^{\mathsf{T}},\, \dot{\boldsymbol{r}}_r^{\mathsf{T}},\, \boldsymbol{x}_{\text{clk},r}\right]^{\mathsf{T}}$, $\boldsymbol{r}_r = [x_r,\, y_r]^{\mathsf{T}}$, $\tilde{\boldsymbol{w}}_r = \left[\tilde{w}_x,\, \tilde{w}_y,\, \tilde{w}_{\delta t_r},\, \tilde{w}_{\dot{\delta} t_r}\right]^{\mathsf{T}}$, $\boldsymbol{u}_r = [u_1,\, u_2]^{\mathsf{T}}$, and

$$\mathbf{A}_r = \begin{bmatrix} \mathbf{0}_{2\times2} & \mathbf{I}_{2\times2} & \mathbf{0}_{2\times2} \\ \mathbf{0}_{2\times2} & \mathbf{0}_{2\times2} & \mathbf{0}_{2\times2} \\ \mathbf{0}_{2\times2} & \mathbf{0}_{2\times2} & \mathbf{A}_{\text{clk}} \end{bmatrix}, \quad \mathbf{B}_r = \begin{bmatrix} \mathbf{0}_{2\times2} \\ \mathbf{I}_{2\times2} \\ \mathbf{0}_{2\times2} \end{bmatrix}, \quad \mathbf{D}_r = \begin{bmatrix} \mathbf{0}_{2\times4} \\ \mathbf{I}_{4\times4} \end{bmatrix}.$$

The receiver's dynamics in (2.1) is discretized at a constant sampling period T. Assuming zero-order hold of the control inputs, i.e., $\{\, u(t) = u(kT),\ kT \le t < (k+1)T \,\}$, and dropping T in the sequel for simplicity of notation yields the discrete-time (DT) model [60]

$$\boldsymbol{x}_r\,(k+1) = \mathbf{F}_r\, \boldsymbol{x}_r(k) + \mathbf{G}_r\, \boldsymbol{u}_r(k) + \boldsymbol{w}_r(k), \quad k = 0, 1, 2, \ldots \tag{2.2}$$

where $\boldsymbol{w}_r = \left[\boldsymbol{w}_{\text{pv}}^{\mathsf{T}},\, \boldsymbol{w}_{\text{clk},r}^{\mathsf{T}}\right]^{\mathsf{T}}$ is a DT zero-mean white noise sequence with covariance $\mathbf{Q}_r$, and

$$\mathbf{F}_r = \begin{bmatrix} \mathbf{I}_{2\times2} & T\mathbf{I}_{2\times2} & \mathbf{0}_{2\times2} \\ \mathbf{0}_{2\times2} & \mathbf{I}_{2\times2} & \mathbf{0}_{2\times2} \\ \mathbf{0}_{2\times2} & \mathbf{0}_{2\times2} & \mathbf{F}_{\text{clk}} \end{bmatrix},\ \mathbf{G}_r = \begin{bmatrix} \frac{T^2}{2}\mathbf{I}_{2\times2} \\ T\,\mathbf{I}_{2\times2} \\ \mathbf{0}_{2\times2} \end{bmatrix},\ \mathbf{F}_{\text{clk}} = \begin{bmatrix} 1 & T \\ 0 & 1 \end{bmatrix},\ \mathbf{Q}_r = \begin{bmatrix} \mathbf{Q}_{\text{pv}} & \mathbf{0}_{4\times2} \\ \mathbf{0}_{2\times4} & \mathbf{Q}_{\text{clk},r} \end{bmatrix}$$

$$\mathbf{Q}_{\text{pv}} = \begin{bmatrix} \tilde{q}_x\frac{T^3}{3} & 0 & \tilde{q}_x\frac{T^2}{2} & 0 \\ 0 & \tilde{q}_y\frac{T^3}{3} & 0 & \tilde{q}_y\frac{T^2}{2} \\ \tilde{q}_x\frac{T^2}{2} & 0 & \tilde{q}_xT & 0 \\ 0 & \tilde{q}_y\frac{T^2}{2} & 0 & \tilde{q}_yT \end{bmatrix}, \quad \mathbf{Q}_{\text{clk},r} = \begin{bmatrix} S_{\tilde{w}_{\delta t_r}}T + S_{\tilde{w}_{\dot{\delta} t_r}}\frac{T^3}{3} & S_{\tilde{w}_{\dot{\delta} t_r}}\frac{T^2}{2} \\ S_{\tilde{w}_{\dot{\delta} t_r}}\frac{T^2}{2} & S_{\tilde{w}_{\dot{\delta} t_r}}T \end{bmatrix}.$$

2.1.3 SOP Dynamics Model

The SOP will be assumed to emanate from a spatially-stationary terrestrial transmitter whose state consists of its planar position $\boldsymbol{r}_s$ and clock error states $\boldsymbol{x}_{\text{clk},s}$. Hence, the SOP's dynamics is described by the state space model

$$\dot{\boldsymbol{x}}_s(t) = \mathbf{A}_s\, \boldsymbol{x}_s(t) + \mathbf{D}_s \tilde{\boldsymbol{w}}_s(t), \tag{2.3}$$

where $\boldsymbol{x}_s = \left[\boldsymbol{r}_s^{\mathsf{T}},\, \boldsymbol{x}_{\text{clk},s}\right]^{\mathsf{T}}$, $\boldsymbol{r}_s = [x_s,\, y_s]^{\mathsf{T}}$, $\tilde{\boldsymbol{w}}_s = \left[\tilde{w}_{\delta t_s},\, \tilde{w}_{\dot{\delta} t_s}\right]^{\mathsf{T}}$, and

$$\mathbf{A}_s = \begin{bmatrix} \mathbf{0}_{2\times 2} & \mathbf{0}_{2\times 2} \\ \mathbf{0}_{2\times 2} & \mathbf{A}_{\text{clk}} \end{bmatrix}, \quad \mathbf{D}_s = \begin{bmatrix} \mathbf{0}_{2\times 2} \\ \mathbf{I}_{2\times 2} \end{bmatrix}.$$

Discretizing the SOP's dynamics (2.3) at a sampling interval T yields the DT-equivalent model

$$\boldsymbol{x}_s\,(k+1) = \mathbf{F}_s\, \boldsymbol{x}_s(k) + \boldsymbol{w}_s(k), \tag{2.4}$$

where $\boldsymbol{w}_s = \boldsymbol{w}_{\text{clk},s}$ is a DT zero-mean white noise sequence with covariance $\mathbf{Q}_s$, and

$$\mathbf{F}_s = \text{diag}\left[\mathbf{I}_{2\times 2},\, \mathbf{F}_{\text{clk}}\right], \quad \mathbf{Q}_s = \text{diag}\left[\mathbf{0}_{2\times 2},\, \mathbf{Q}_{\text{clk},s}\right],$$

where $\mathbf{Q}_{\text{clk},s}$ is identical to $\mathbf{Q}_{\text{clk},r}$, except that $S_{\tilde{w}_{\delta t_r}}$ and $S_{\tilde{w}_{\dot{\delta} t_r}}$ are now replaced with SOP-specific spectra, $S_{\tilde{w}_{\delta t_s}}$ and $S_{\tilde{w}_{\dot{\delta} t_s}}$, respectively.

2.2 Observation Model

The observation made by a receiver on a particular SOP is assumed to be a pseudorange observation. To properly model a pseudorange observation,

one must consider three different time systems. The first is true time, denoted by t, which can be considered equivalent to GPS system time. The second time system is that of the receiver's clock and is denoted t_r. The third time system is that of the SOP's clock and is denoted t_s. The three time systems are related to each other according to

$$t = t_r - \delta t_r(t), \qquad t = t_s - \delta t_s(t), \tag{2.5}$$

where $\delta t_r(t)$ and $\delta t_s(t)$ are the amount by which the receiver and SOP clocks are different from true time, respectively.

The pseudorange observation made by the receiver on a particular SOP is made in the receiver time and is modeled according to

$$\begin{aligned} \rho(t_r) &= \|\boldsymbol{r}_r\left[t_r - \delta t_r(t_r)\right] - \boldsymbol{r}_s\left[t_r - \delta t_r(t_r) - \delta t_{\mathrm{TOF}}\right]\|_2 + \\ &\quad c\,.\,\{\delta t_r(t_r) - \delta t_s\left[t_r - \delta t_r(t_r) - \delta t_{\mathrm{TOF}}\right]\} + \tilde{v}_\rho(t_r), \end{aligned} \tag{2.6}$$

where c is the speed of light, δt_{TOF} is the time of flight of the signal from the SOP to the receiver, and $\tilde{v}_\rho$ is the error in the pseudorange measurement due to modeling and measurement errors. The error $\tilde{v}_\rho$ is modeled as a zero-mean white Gaussian noise process with power spectral density $\tilde{r}$ [61]. In (2.6), the clock offsets δt_r and δt_s were assumed to be small and slowly changing, in which case $\delta t_r(t) = \delta t_r\left[t_r - \delta t_r(t)\right] \approx \delta t_r(t_r)$. The first term in (2.6) is the true range between the receiver's position at time of reception and the SOP's position at time of transmission of the signal, while the second term arises due to the offsets from true time in the receiver and SOP clocks.

The observation model in the form of (2.6) is inappropriate for our upcoming analysis and synthesis as it suffers from two shortcomings: (i) it is in a time system that is different from the one considered in deriving the system dynamics, and (ii) the observation model is a nonlinear function of the delayed system states. The first shortcoming can be dealt with by converting the observation model to true time. The second problem is commonly referred to as the output delay problem, in which the observations (outputs) are a delayed version, deterministic or otherwise, of the system state. A common approach to deal with this problem entails discretization and state augmentation [62, 63]. For simplicity, and in order not to introduce additional states in our model, proper approximations will be invoked to deal with the second shortcoming.

To this end, the pseudorange observation model in (2.6) is converted to true time by invoking the relationship (2.5) to get an observation model for $\rho[t+\delta t_r(t)]$. The resulting observation model is delayed by $\delta t_r(t)$ to get an observation model for $\rho(t)$. Assuming the receiver's position to be approximately stationary within a time interval of $\delta t_r(t)$, i.e., $\boldsymbol{r}_r\left[t-\delta t_r(t)\right] \approx \boldsymbol{r}_r(t)$, and using the fact that the SOP's position is stationary, i.e., $\boldsymbol{r}_s\left[t-\delta t_r(t)-\delta t_{\mathrm{TOF}}\right] = \boldsymbol{r}_s(t)$, yields

$$\rho(t) \;\approx\; \|\boldsymbol{r}_r(t)-\boldsymbol{r}_s(t)\|_2 + c\,.\,\{\delta t_r(t) - \delta t_s\left[t-\delta t_r(t)-\delta t_{\mathrm{TOF}}\right]\} + \tilde{v}_\rho(t).$$

Next, it is argued that $\delta t_s\left[t-\delta t_r(t)-\delta t_{\mathrm{TOF}}\right] \approx \delta t_s\left(t\right)$. The validity of this argument depends on the size of δt_r and of δt_{TOF} and on the rate of change of δt_s. For ground-based SOP transmitters up to 1 km away, the time of

flight δt_{TOF} is less than $3.34\,\mu$s. Likewise, the offset δt_r can be assumed to be on the order of microseconds. It is reasonable to assume the SOP clock bias δt_s to have an approximately constant value over microsecond time intervals. Therefore, the pseudorange observation model can be further simplified and expressed as a nonlinear function of the state as

$$\begin{aligned} z(t) &= \rho(t) \triangleq y(t) + \tilde{v}_\rho(t) \\ &\approx \|\boldsymbol{r}_r(t) - \boldsymbol{r}_s(t)\|_2 + c \cdot [\delta t_r(t) - \delta t_s(t)] + \tilde{v}_\rho(t), \end{aligned} \tag{2.7}$$

where y is the noise-free observation. Discretizing the observation equation (2.7) at a constant sampling interval T yields the DT-equivalent observation model

$$\begin{aligned} z(k) &= y(k) + v_\rho(k) \\ &= \|\boldsymbol{r}_r(k) - \boldsymbol{r}_s(k)\|_2 + c \cdot [\delta t_r(k) - \delta t_s(k)] + v_\rho(k), \end{aligned} \tag{2.8}$$

where v_ρ is a DT zero-mean white Gaussian sequence with variance $r = \tilde{r}/T$ [60].

It is worth noting that the main sources of error affecting pseudorange observations include uncertainties associated with the propagation medium (path delay and loss), receiver noise, multipath propagation, non-line of sight (NLOS) propagation, multiple access interference, and near-far effects. The effects of such error sources and mitigation methods are beyond the scope of this dissertation, but relevant discussions can be found in [8, 33, 35, 36, 64] and the references therein.

Chapter 3

Observability and Estimability Analyses

This chapter analyzes the observability and estimability of COpNav environments. The objective of the observability analysis is threefold: (*i*) determine the conditions under which the COpNav environment is fully-observable, (*ii*) whenever the environment is not fully-observable, determine the observable states, if any, and (*iii*) determine the effects of receiver-controlled maneuvers on observability. The objective of the estimability analysis is to assess the degree of observability of the various states with particular attention paid to the most and least observable directions in the state space.

This chapter is organized as follows. Section 3.1 summarizes various observability notions of dynamical systems, which are of relevance in analyzing COpNav environments. Section 3.2 analyzes the observability of a simplified environment through nonlinear, linear, and linear piecewise constant system (PWCS) observability tools and describes the misapplication of the linear PWCS test encountered in the literature. Section 3.3 discusses receiver trajectories that yield observability singularity. Section 3.4 outlines a number of scenarios, which a typical COpNav environment could exhibit, whose observability is analyzed. Sections 3.5 and 3.6 analyze the observability of

COpNav environments through linear and nonlinear observability tools, respectively. Section 3.7 presents simulation results to assess the estimability of the observable COpNav scenarios. Section 3.8 presents experimental results illustrating an important outcome of the observability analysis.

3.1 Theoretical Background: Observability of Dynamical Systems

Conceptually, observability of a dynamical system is a question of solvability of the state from a set of observations that are linearly or nonlinearly related to the state, and where the state evolves according to a set of linear or nonlinear difference or differential equations. In particular, observability is concerned with determining whether the state of the system can be consistently estimated from a set of observations taken over a period of time.

3.1.1 Observability of Nonlinear Systems

For the sake of clarity, various notions of nonlinear observability are defined in this subsection [65]. Two fundamental contrasts between observability of nonlinear and linear systems are [66]:

(i) *Choice of inputs.* In the linear case, if any input $\boldsymbol{u}$ makes the system observable, then every input does so; hence, it suffices to consider the case $\boldsymbol{u} \equiv \mathbf{0}$. In nonlinear systems, this is not the case. Specifically, there may exist certain inputs that could turn an observable system into unobservable. Hence, sensing and actuation in nonlinear systems may be coupled, and they need to

be studied simultaneously.

(*ii*) *Length of observations.* For observable CT linear systems, observing the outputs $\boldsymbol{y}$ over any arbitrary time interval is sufficient. In nonlinear systems, it may be necessary to observe $\boldsymbol{y}$ over a long, even infinite, time intervals.

Definition 3.1.1. Consider the CT nonlinear dynamical system

$$\Sigma_{\text{NL}} : \begin{cases} \dot{\boldsymbol{x}}(t) = \boldsymbol{f}\left[\boldsymbol{x}(t), \boldsymbol{u}(t)\right], \quad \boldsymbol{x}(t_0) = \boldsymbol{x}_0 \\ \boldsymbol{y}(t) = \boldsymbol{h}\left[\boldsymbol{x}(t)\right], \end{cases} \tag{3.1}$$

with solution $\boldsymbol{x}(t) = \boldsymbol{g}\left(t, \boldsymbol{x}_0, \boldsymbol{u}\right)$, where $\boldsymbol{x} \in \mathbb{R}^n$ is the system state vector, $\boldsymbol{u} \in \mathbb{R}^r$ is the control input vector, $\boldsymbol{y} \in \mathbb{R}^m$ is the observation vector, and $\boldsymbol{x}_0$ is an arbitrary initial condition. Two states $\boldsymbol{x}_1$ and $\boldsymbol{x}_2$ are said to be indistinguishable if $\boldsymbol{h}[\boldsymbol{g}\left(t, \boldsymbol{x}_1, \boldsymbol{u}\right)] = \boldsymbol{h}[\boldsymbol{g}\left(t, \boldsymbol{x}_2, \boldsymbol{u}\right)]$, $\forall t \geq 0$ and $\forall \boldsymbol{u}$. The set of all points indistinguishable from a particular state $\boldsymbol{x}$ is denoted as $\mathbb{I}(\boldsymbol{x})$.

Definition 3.1.2. Let $\mathfrak{N}$ be a subset (neighborhood) in the state space $\mathbb{R}^n$ and $\boldsymbol{x}_1, \boldsymbol{x}_2 \in \mathfrak{N}$. Two states $\boldsymbol{x}_1$ and $\boldsymbol{x}_2$ are said to be $\mathfrak{N}$-indistinguishable if every control $\boldsymbol{u}$, whose trajectories from $\boldsymbol{x}_1$ and $\boldsymbol{x}_2$ both lie in $\mathfrak{N}$, fails to distinguish between $\boldsymbol{x}_1$ and $\boldsymbol{x}_2$. The set of all $\mathfrak{N}$-indistinguishable states from a particular state $\boldsymbol{x}$ is denoted as $\mathbb{I}_{\mathfrak{N}}(\boldsymbol{x})$.

Definition 3.1.3. The system Σ_{NL} is said to be observable at $\boldsymbol{x}_0$ if $\mathbb{I}(\boldsymbol{x}_0) = \{\boldsymbol{x}_0\}$. The system Σ_{NL} is said to be observable if $\mathbb{I}(\boldsymbol{x}_0) = \{\boldsymbol{x}_0\}$, $\forall \boldsymbol{x}_0 \in \mathbb{R}^n$.

Note that observability is a global concept. It might be necessary to travel a considerable distance or for a long period of time to distinguish between initial conditions in $\mathbb{R}^n$. Moreover, observability of Σ_{NL} does not imply that every input $\boldsymbol{u}$ distinguishes initial conditions in $\mathbb{R}^n$.

Definition 3.1.4. The system Σ_{NL} is said to be locally observable at $\boldsymbol{x}_0$ if $\mathbb{I}_{\mathfrak{N}}(\boldsymbol{x}_0) = \{\boldsymbol{x}_0\}$ for every open neighborhood $\mathfrak{N}$ of $\boldsymbol{x}_0$.

Note that local observability is stronger than observability. Local observability requires distinguishability of the initial conditions without going too far. In particular, trajectories need to lie in *any* open subset of $\mathbb{R}^n$.

Definition 3.1.5. The system Σ_{NL} is said to be weakly observable at $\boldsymbol{x}_0$ if there exists a neighborhood $\mathfrak{N}$ such that $\mathbb{I}(\boldsymbol{x}_0) \bigcap \mathfrak{N} = \{\boldsymbol{x}_0\}$.

Note that weak observability is weaker than observability. Weak observability requires the existence of an open subset in $\mathbb{R}^n$ within which the only initial condition that is indistinguishable from $\boldsymbol{x}_0$ is $\boldsymbol{x}_0$ itself. Note that in weakly observable systems, trajectories may need to travel far enough for distinguishability of the initial conditions.

Definition 3.1.6. The system Σ_{NL} is said to be locally weakly observable at $\boldsymbol{x}_0$ if there exists an open neighborhood $\mathfrak{N}$ of $\boldsymbol{x}_0$ such that for every open neighborhood $\mathfrak{M}$ of $\boldsymbol{x}_0$ with $\mathfrak{M} \subset \mathfrak{N}$, $\mathbb{I}_{\mathfrak{M}}(\boldsymbol{x}_0) = \{\boldsymbol{x}_0\}$.

Intuitively, Σ_{NL} is locally weakly observable if $\boldsymbol{x}_0$ can be instantaneously distinguished from its neighbors. The various notions of observability are related to each other according to the following relationships

$$\begin{array}{ccc} \text{locally observable} & \Rightarrow & \text{observable} \\ \Downarrow & & \Downarrow \\ \text{locally weakly observable} & \Rightarrow & \text{weakly observable.} \end{array}$$

For nonlinear systems, establishing global system properties, such as observability, is typically difficult to achieve. Hence, local properties are typically sought. An algebraic test exists for establishing local weak observability of a specific form of the nonlinear system Σ_{NL} in (3.1), known as the control affine form [67], given by

$$\Sigma_{\mathrm{NL,a}} : \begin{cases} \dot{\boldsymbol{x}}(t) = \boldsymbol{f}_0\left[\boldsymbol{x}(t)\right] + \sum_{i=1}^{r} \boldsymbol{f}_i\left[\boldsymbol{x}(t)\right] u_i, \quad \boldsymbol{x}(t_0) = \boldsymbol{x}_0 \\ \boldsymbol{y}(t) = \boldsymbol{h}\left[\boldsymbol{x}(t)\right]. \end{cases} \tag{3.2}$$

This test is based on constructing the so-called nonlinear observability matrix defined next.

Definition 3.1.7. The first-order Lie derivative of a scalar function h with respect to a vector-valued function $\boldsymbol{f}$ is

$$\mathfrak{L}^1_{\boldsymbol{f}} h(\boldsymbol{x}) \triangleq \sum_{j=1}^{n} \frac{\partial h(\boldsymbol{x})}{\partial x_j} f_j(\boldsymbol{x}) = \left\langle \nabla_{\boldsymbol{x}} h(\boldsymbol{x}), \boldsymbol{f}(\boldsymbol{x}) \right\rangle, \tag{3.3}$$

where $\boldsymbol{f}(\boldsymbol{x}) \triangleq [f_1(\boldsymbol{x}), \ldots, f_n(\boldsymbol{x})]^{\mathsf{T}}$. The zeroth-order Lie derivative of any function is the function itself, i.e., $\mathfrak{L}^0_{\boldsymbol{f}} h(\boldsymbol{x}) = h(\boldsymbol{x})$. The second-order Lie derivative can be computed recursively as

$$\mathfrak{L}^2_{\boldsymbol{f}} h(\boldsymbol{x}) = \mathfrak{L}_{\boldsymbol{f}}\left[\mathfrak{L}^1_{\boldsymbol{f}} h(\boldsymbol{x})\right] = \left\langle \left[\nabla_{\boldsymbol{x}} \mathfrak{L}^1_{\boldsymbol{f}} h(\boldsymbol{x})\right], \boldsymbol{f}(\boldsymbol{x}) \right\rangle. \tag{3.4}$$

Higher-order Lie derivatives can be computed similarly. Mixed-order Lie derivatives of $h(\boldsymbol{x})$ with respect to different functions $\boldsymbol{f}_i$ and $\boldsymbol{f}_j$, given the derivative with respect to $\boldsymbol{f}_i$, can be defined as

$$\mathfrak{L}^2_{\boldsymbol{f}_i \boldsymbol{f}_j} h(\boldsymbol{x}) \triangleq \mathfrak{L}^1_{\boldsymbol{f}_j}\left[\mathfrak{L}^1_{\boldsymbol{f}_i} h(\boldsymbol{x})\right] = \left\langle \left[\nabla_{\boldsymbol{x}} \mathfrak{L}^1_{\boldsymbol{f}_i} h(\boldsymbol{x})\right], \boldsymbol{f}_j(\boldsymbol{x}) \right\rangle.$$

The nonlinear observability matrix, denoted $\mathfrak{O}_{\mathrm{NL}}$, of $\Sigma_{\mathrm{NL,a}}$ defined in (3.2) is a matrix whose rows are the gradients of Lie derivatives, specifically

$$\mathfrak{O}_{\mathrm{NL}} \triangleq \left\{ \nabla_{\boldsymbol{x}}^{\mathsf{T}} \left[\mathfrak{L}^{p}_{\boldsymbol{f}_i,\ldots,\boldsymbol{f}_j} h_l(\boldsymbol{x}) \right] \,\middle|\, i,j = 0,\ldots,p;\; p = 0,\ldots,\, n-1; l = 1,\ldots,m \right\},$$

where $\boldsymbol{h}(\boldsymbol{x}) \triangleq [h_1(\boldsymbol{x}),\ldots,h_m(\boldsymbol{x})]^{\mathsf{T}}$.

The significance of the nonlinear observability matrix is that it can be employed to furnish necessary and sufficient conditions for local weak observability [65]. In particular, if $\mathfrak{O}_{\mathrm{NL}}$ is full-rank, then the system $\Sigma_{\mathrm{NL,a}}$ is said to satisfy the observability rank condition.

Theorem 3.1.1. *If the nonlinear system in control affine form $\Sigma_{\mathrm{NL,a}}$ satisfies the observability rank condition, then the system is locally weakly observable.*

Theorem 3.1.2. *If a system $\Sigma_{\mathrm{NL,a}}$ is locally weakly observable, then the observability rank condition is satisfied generically.*

The term "generically" means that the observability matrix is full-rank everywhere, except possibly within a subset of the domain of $\boldsymbol{x}$ [66]. Therefore, if $\mathfrak{O}_{\mathrm{NL}}$ is not of sufficient rank for all values of $\boldsymbol{x}$, the system is not locally weakly observable [68].

3.1.2 Observability of Linear Systems

For linear time-invariant (LTI) systems, the four notions of nonlinear observability are equivalent. Observability of linear time-varying (LTV) systems is defined next [69].

Definition 3.1.8. Consider the DT LTV dynamical system

$$\Sigma_{\mathrm{L}} : \begin{cases} \boldsymbol{x}(k+1) = \mathbf{F}(k)\boldsymbol{x}(k) + \mathbf{G}(k)\boldsymbol{u}(k), & \boldsymbol{x}(k_0) = \boldsymbol{x}_0 \\ \boldsymbol{y}(k) \quad = \mathbf{H}(k)\boldsymbol{x}(k), & k \in [k_0, k_f], \end{cases} \tag{3.5}$$

where $\mathbf{F} \in \mathbb{R}^{n\times n}$, $\mathbf{G} \in \mathbb{R}^{n\times r}$, and $\mathbf{H} \in \mathbb{R}^{m\times n}$. The LTV system Σ_{L} is said to be observable in a time interval $[k_0, k_f]$, if the initial state $\boldsymbol{x}_0$ is uniquely determined by the zero-input response $\boldsymbol{y}(k)$ for $k \in [k_0, k_f - 1]$. If this property holds regardless of the initial time k_0 or the initial state $\boldsymbol{x}_0$, the system is said to be completely observable.

Observability of LTV systems Σ_{L} is typically established through studying the rank of either the so-called observability Grammian or the observability matrix. The following theorem states a necessary and sufficient condition for observability of LTV systems through the l-step observability matrix [69].

Theorem 3.1.3. *The LTV system Σ_{L} is l-step observable if and only if the l-step observability matrix, defined as*

$$\mathfrak{O}_L(k, k+l) \triangleq \begin{bmatrix} \mathbf{H}(k) \\ \mathbf{H}(k+1)\mathbf{\Phi}(k+1,k) \\ \vdots \\ \mathbf{H}(k+l-1)\mathbf{\Phi}(k+l-1,k) \end{bmatrix} \tag{3.6}$$

is full-rank, i.e., $\operatorname{rank}[\mathfrak{O}_L(k, k+l)] = n$. *The matrix function $\mathbf{\Phi}$ is the DT transition matrix, defined as*

$$\mathbf{\Phi}(k,j) \triangleq \begin{cases} \mathbf{F}(k-1)\mathbf{F}(k-2)\cdots\mathbf{F}(j), & k \geq j+1; \\ \mathbf{I}, & k = j. \end{cases}$$

Linear observability tools may be applied to nonlinear systems by expressing the nonlinear system in its linearized error form. In this formulation, the state vector $\Delta\boldsymbol{x}$, control input vector $\Delta\boldsymbol{u}$, and observation vector $\Delta\boldsymbol{y}$, are defined as the difference between the true and nominal states, between the true and nominal inputs, and between the true and nominal observations, respectively. The discretized version of the linearized error form of Σ_{NL} in (3.1) is given by

$$\begin{aligned} \Delta\boldsymbol{x}\,(k+1) &= \mathbf{F}(k)\,\Delta\boldsymbol{x}\,(k) + \mathbf{G}(k)\,\Delta\boldsymbol{u}\,(k) \\ \Delta\boldsymbol{y}(k) &= \mathbf{H}(k)\Delta\boldsymbol{x}\,(k)\,, \end{aligned} \tag{3.7}$$

where $\mathbf{F}$, $\mathbf{G}$, and $\mathbf{H}$ are the dynamics, input, and observation Jacobian matrices, respectively, evaluated at the nominal states and inputs. The observability results achieved in this case are only valid locally.

3.1.3 Observability of Linear Piecewise Constant Systems

Another test to to establish observability of the LTV system Σ_{L} can be derived if the LTV system is piecewise constant. Observability of linear PWCSs has been analyzed for CT and DT systems [70] and is summarized next.

Definition 3.1.9. An LTV system

$$\Sigma_{\mathrm{L,pwcs}} : \begin{cases} \boldsymbol{x}(k+1) = \mathbf{F}_j(k)\,\boldsymbol{x}(k) + \mathbf{B}_j(k)\,\boldsymbol{u}(k), \quad \boldsymbol{x}(0) = \boldsymbol{x}_0 \\ \boldsymbol{y}(k) = \mathbf{H}_j(k)\,\boldsymbol{x}(k), \end{cases} \tag{3.8}$$

where $j = 1, \ldots, s$, is said to be piecewise constant if for every time segment j, the matrices $\mathbf{F}_j$, $\mathbf{B}_j$, and $\mathbf{H}_j$ are constant, i.e., $\mathbf{F}_j(k) = \mathbf{F}_j$, $\mathbf{B}_j(k) = \mathbf{B}_j$, and $\mathbf{H}_j(k) = \mathbf{H}_j$. These matrices may vary from one segment to another.

Definition 3.1.10. The instantaneous observability matrix of the PWCS $\Sigma_{\text{L,pwcs}}$ in segment j is defined as

$$\mathfrak{O}_j = \begin{bmatrix} \mathbf{H}_j \\ \mathbf{H}_j\mathbf{F}_j \\ \mathbf{H}_j\mathbf{F}_j^2 \\ \vdots \\ \mathbf{H}_j\mathbf{F}_j^{n-1} \end{bmatrix}. \tag{3.9}$$

Definition 3.1.11. The total observability matrix (TOM) of the PWCS $\Sigma_{\text{L,pwcs}}$ up to segment s is defined as

$$\mathfrak{O}_{\text{TOM}}(s) = \begin{bmatrix} \mathfrak{O}_1 \\ \mathfrak{O}_2\mathbf{F}_1^{n-1} \\ \mathfrak{O}_3\mathbf{F}_2^{n-1}\mathbf{F}_1^{n-1} \\ \vdots \\ \mathfrak{O}_s\mathbf{F}_{s-1}^{n-1}\mathbf{F}_{s-2}^{n-1}\cdots\mathbf{F}_1^{n-1} \end{bmatrix}. \tag{3.10}$$

Theorem 3.1.4. *The DT PWCS system $\Sigma_{\text{L,pwcs}}$ is observable if and only if the TOM is full-rank, i.e.,* $\text{rank}\,[\mathfrak{O}_{\text{TOM}}(s)] = n$.

3.1.4 Stochastic Observability via Fisher Information

From an estimation theoretic point of view, the Fisher information matrix (FIM) quantifies the maximum existing information in observations about the system's random state. A singular FIM implies that the Cramér-Rao lower bound does not exist, as the FIM's inverse has one or more infinite eigenvalues, which means total uncertainty in a subspace of the state space. This amounts to the information being insufficient for the estimation problem under consideration [58]. Under Gaussian assumptions and minimum mean squared error estimation, the FIM is the inverse of the estimation error covariance matrix.

Hence, another assessment of observability can be achieved by analyzing the information form of the Kalman filter (KF). If the system is observable, then the information matrix will eventually become invertible.

3.1.5 Degree of Observability: Estimability

Whereas the notion of observability is a Boolean property, i.e., it specifies whether the system is observable or not; for estimation purposes, the question of estimability is of considerable importance. Estimability assesses the "degree of observability" of the various states. Estimability can be assessed by the condition number of the FIM, thus measuring whether an observable system is poorly estimable due to the gradient vectors comprising the FIM being nearly collinear [58].

An alternative method for assessing estimability of the different states was proposed in [71]. This method is based on analyzing the eigenvalues and eigenvectors of a normalized estimation error covariance matrix of the KF. The normalization of the estimation error covariance serves two purposes. First, it forces the transformed estimation error vector to be dimensionless. This dimensional homogeneity makes comparison among the eigenvalues meaningful. Such transformation can be accomplished through the congruent transformation

$$\mathbf{P}'(k|k) = \left[\sqrt{\mathbf{P}(0|-1)}\right]^{-1} \mathbf{P}(k|k) \left[\sqrt{\mathbf{P}(0|-1)}\right]^{-1},$$

where $\mathbf{P}(0|-1)$ is the initial estimation error covariance and $\mathbf{P}(k|k)$ is the posterior estimation error covariance. Second, it sets a bound for the eigenvalues

such that they are bounded between zero and n. This can be accomplished through

$$\mathbf{P}^{''}(k|k) = \frac{n}{\text{tr}\,[\mathbf{P}^{'}(k|k)]}\mathbf{P}^{'}(k|k). \tag{3.11}$$

The largest eigenvalue of $\mathbf{P}^{''}(k|k)$ corresponds to the variance of the state or linear combination of states that is poorly observable. On the other hand, the state or linear combination of states that is most observable is indicated by the smallest eigenvalue. The appropriate linear combination of states yielding the calculated degree of observability is given by the respective eigenvectors. Of course, there are cases where the eigenvalues distribution is uninteresting and nothing startling is revealed by this method. However, wide dispersion of the eigenvalues indicate cases of exceptionally good or poor observability of certain linear combinations of the states [71].

3.2 Motivating Example

A study of COpNav observability benefits from the COpNav-SLAM analogy. Although the question of observability was not addressed for more than a decade after SLAM was introduced, the recent SLAM literature has come around to considering fundamental properties of the SLAM problem, including observability [72–82]. The effects of partial observability in planar SLAM with range and bearing measurements were first analyzed via linearization in [72, 73]. These papers came to the counterintuitive conclusion that the two-dimensional planar wold-centric (absolute reference frame) SLAM problem is fully-observable when the location of a single landmark is known *a priori*.

With a nonlinear observability analysis, this result was subsequently disproved and it was shown that at least two anchor landmarks with known positions are required for local weak observability [75]. Later analysis of the SLAM problem's FIM confirmed the result of the nonlinear analysis [76]. However, an apparent discrepancy between linear and nonlinear SLAM observability re-emerged in [77], where it was shown that a linear analysis based on PWCS theory again predicted global planar SLAM observability in the case of a single known anchor landmark, whereas a nonlinear analysis in the same paper indicated that two known anchor landmarks were required for local weak observability. However, no explanation for the reasons behind such discrepancies were offered. The linear PWCS result appears flawed, since an observability test based on linearization should never predict observability in a case where a nonlinear test indicates lack of observability.

Next, the nonlinear, linear, and linear PWCS observability tests discussed in Subsections 3.1.1, 3.1.2, and 3.1.3, respectively, will be applied to a simplified environment whose observability can be readily assessed via physical intuition. The objective of this motivating example is to explain the observability discrepancies reported in the SLAM literature.

Consider an environment with one unknown receiver and one fully-known anchor SOP, i.e., an SOP with a known initial state vector. Assume that the receiver and SOP clocks are perfect, in which case the environment's state vector consists of the receiver's position and velocity and the SOP's position, namely $\boldsymbol{x} = [x_r,\, y_r,\, \dot{x}_r,\, \dot{y}_r,\, x_{s,a},\, y_{s,a}]^{\mathsf{T}}$. The observation in this case

is the true range between the receiver and the SOP. Hence, the observation vector has the form $\boldsymbol{y}(t) = [\, x_{s,a}(t),\, y_{s,a}(t),\, \|\boldsymbol{r}_r(t) - \boldsymbol{r}_{s,a}(t)\|_2 \,]^{\mathsf{T}}$, where the two fictitious observations $x_{s,a}$ and $y_{s,a}$ were augmented to the observation vector to indicate knowledge of the position of the anchor SOP.

First, the nonlinear observability analysis is considered. The nonlinear observability matrix $\mathfrak{O}_{\mathrm{NL}}$ for this environment has rank 5. Since $\mathfrak{O}_{\mathrm{NL}}$ is rank-deficient, then by Theorem 3.1.2 we conclude that the environment is unobservable. Even though the notion of an "unobservable subspace" cannot be strictly defined for this system, by examining the physical interpretation of the basis of $\mathfrak{O}_{\mathrm{NL}}^{\perp}$, i.e., the basis of the unobservable subspace, we will gain useful information. A basis for the subspace $\mathfrak{O}_{\mathrm{NL}}^{\perp}$ is given by

$$\mathfrak{O}_{\mathrm{NL}}^{\perp} = \mathrm{span}\left[\begin{array}{ccccccc} \frac{-y_r+y_{s,a}}{\dot{x}_r} & \frac{x_r-x_{s,a}}{\dot{x}_r} & -\frac{\dot{y}_r}{\dot{x}_r} & 1 & 0 & 0 \end{array}\right]^{\mathsf{T}}.$$

The fact that the last two elements are zeros imply that the states $x_{s,a}$ and $y_{s,a}$ are orthogonal to the unobservable subspace; hence, they are observable, which is true by construction.

To employ the linear observability tools, the environment model will be expressed in its linearized error form described in (3.7). Next, the LTV observability analysis through the l-step observability matrix $\mathfrak{O}_L(k, k+l)$ is considered. Performing such analysis yields a 1-step observability matrix $\mathfrak{O}_L(0,1)$ whose rank is 3, a 2-step observability matrix $\mathfrak{O}_L(0,2)$ whose rank is 4, and a 3-step observability matrix $\mathfrak{O}_L(0,3)$ whose rank is 5. Adding more time-steps does not improve the observability any further, and the l-step observability

matrix will always be rank-deficient by 1, suggesting that the system is unobservable. In fact, the resulting null-space of $\mathfrak{O}_L(0,l)$, $\forall l \geq 3$, is identical to the subspace $\mathfrak{O}_{\text{NL}}^{\perp}$.

Third, the observability analysis based on linear PWCS theory is considered. Performing such analysis yields a TOM for the first time segment $\mathfrak{O}_{\text{TOM}}(1)$ whose rank is 4. The null-space for such matrix is given by

$$\mathcal{N}\left[\mathfrak{O}_{\text{TOM}}(1)\right] = \text{span}\begin{bmatrix} 0 & 0 & -\frac{y_r - y_{s,a} + T\dot{y}_r}{x_r - x_{s,a} + T\dot{x}_r} & 1 & 0 & 0 \\ -\frac{y_r - y_{s,a} + T\dot{y}_r}{x_r - x_{s,a} + T\dot{x}_r} & 1 & 0 & 0 & 0 & 0 \end{bmatrix}^{\mathsf{T}}.$$

Adding a second time segment results in a full-rank $\mathfrak{O}_{\text{TOM}}(2)$; hence, according to Theorem 3.1.4, the system is observable. Not only this conclusion contradicts the nonlinear and LTV observability analyses, but it also defies physical intuition.

For this simple environment, from physical intuition we know that the environment is fully-observable with the knowledge of at least two known anchor SOPs. Indeed, performing the nonlinear and the LTV observability tests with two known anchor SOPs results in full-rank $\mathfrak{O}_{\text{NL}}$ and $\mathfrak{O}_L(k, k+l)$, respectively, which indicates that the receiver's state vector could be determined from the observations. Such determination will, however, be ambiguous, since there exists two indistinguishable initial conditions that would result in the same observations.

As a concrete example, consider the scenario depicted in Figure 3.1. Here, SOP_1 and SOP_2 are of known positions and the receiver is moving along

the dashed line according to velocity random walk dynamics. In this case, a receiver that starts from the initial state $(x_r(0), y_r(0))$ and one that starts from the initial state $(x_r(0), -y_r(0))$ will produce identical range measurements. Hence, these initial conditions are indistinguishable given the range measurements made by the receiver on both SOPs. In fact, it can be demonstrated that as long an estimator, e.g., extended Kalman filter (EKF), is initialized with an initial estimate that lies in the same half-plane ($y > 0$ or $y < 0$) as the true initial state, the estimate will converge to the true state trajectory, whereas if the initial estimate is set to be in the opposite half-plane, it will converge to the opposite (incorrect) trajectory.

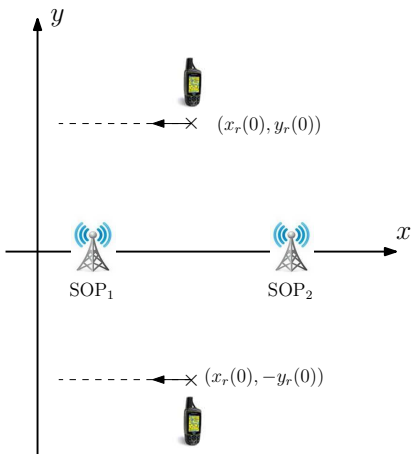

Figure 3.1: Environment with an unknown receiver and two fully-known anchor SOPs

In particular, consider an environment with $\boldsymbol{x}_r(0) = [250, 250, -10, 0]^\mathsf{T}$, $\boldsymbol{x}_{s,a_1}(0) = [0, 0]^\mathsf{T}$, $\boldsymbol{x}_{s,a_2}(0) = [500, 0]^\mathsf{T}$, $\tilde{q}_x = \tilde{q}_x = 0.01\,(\frac{m}{s^2})^2$, $\tilde{r} = 25\,\text{m}^2$, and $T = 0.1\,\text{s}$. Figure 3.2(a) shows the estimation error $\tilde{\boldsymbol{x}}(k|k) \triangleq \boldsymbol{x}(k) - \hat{\boldsymbol{x}}(k|k)$

along with the estimation error variances achieved through an EKF with an initial state estimate $\hat{\boldsymbol{x}}(0|-1) = [150, 150, -5, 5]^{\mathsf{T}}$ and an initial estimation error covariance $\mathbf{P}(0|-1) = (10^3)\,\mathbf{I}_{4\times 4}$. Note that the estimates converged to the true state trajectories and that the estimation errors remained bounded. In contrast, initializing the initial state estimate at $\hat{\boldsymbol{x}}(0|-1) = [150, -150, -5, 5]^{\mathsf{T}}$ yielded the estimation error trajectories illustrated in Figure 3.2(b). Note that while the estimation error trajectory $\tilde{y}(k|k)$ converged and remained bounded, it converged to an incorrect trajectory– one corresponding to a receiver with an initial condition $\boldsymbol{x}_r(0) = [250, -250, -10, 0]^{\mathsf{T}}$.

Of course, adding a third fully-known SOP resolves this ambiguity. Why are the nonlinear and linear observability analyses revealing that only two fully-known anchor SOPs are needed? On one hand, the nonlinear observability analysis only guarantees weak local observability, namely the existence of a neighborhood within which the initial states are distinguishable. For the scenario depicted in Figure 3.1, such neighborhood turns out to be a half-plane around the initial condition. On the other hand, the fact that we are linearizing the nonlinear observations first implies that the LTV observability results are only valid locally, i.e., in the neighborhood where the linearizations are valid.

Another important conclusion from this motivating example is that the observability analysis through the linear PWCS theory, as applied, is not appropriate for analyzing COpNav environments. The confusion arising from the observability conclusions of this theory, which is demonstrated in this

simple example, are similar to the ones encountered in the SLAM literature [72–77]. The reason behind these discrepancies is that one cannot simply take the time segment j to coincide with the discretization instant k. Rather, each time segment j must contain at least n measurement samples during the collection of which the Jacobian matrices $\mathbf{F}$, $\mathbf{G}$, and $\mathbf{H}$ can be accurately modeled as constant.

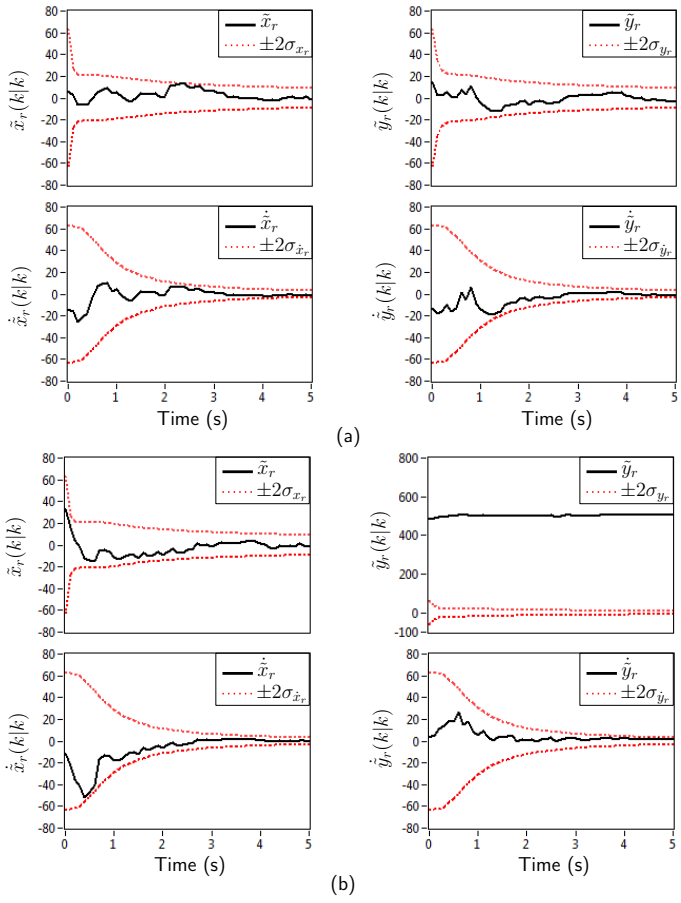

Figure 3.2: Estimation error trajectories for the environment depicted in Figure 3.1 with initial state estimate (a) $\hat{\boldsymbol{x}}(0|-1) = [150, 150, -5, 5]^{\mathsf{T}}$ and (b) $\hat{\boldsymbol{x}}(0|-1) = [150, -150, -5, 5]^{\mathsf{T}}$

3.3 Receiver Trajectory Singularity

In the upcoming analysis, it is assumed that the receiver is not stationary, specifically $\dot{x}_r(0) \neq 0$ and $\dot{y}_r(0) \neq 0$. Moreover, it is assumed that the receiver's trajectory is not collinear with the vectors connecting the receiver and any of the SOPs. Specifically, it is assumed that $\nexists\ \alpha \in \mathbb{R}$ such that $\dot{x}_r(k+1) = \alpha\,[x_r(k) - x_s(k)]$ and $\dot{y}_r(k+1) = \alpha\,[y_r(k) - y_s(k)]$. This ensures that the bearing angle between the receiver and the SOPs is never constant along the receiver trajectory. This assumption ensures that the observability matrix will not lose rank due to the receiver's motion path.

To illustrate why this case must be excluded, consider a simplified scenario in which the receiver and SOP clocks are ideal, i.e., with no bias nor drift, such that the observations are given by $y(k) = \|\boldsymbol{r}_r(k) - \boldsymbol{r}_s(k)\|_2$. In this case, the environment state vector is given by $\boldsymbol{x} = \left[\boldsymbol{r}_r^\mathsf{T},\, \dot{\boldsymbol{r}}_r^\mathsf{T}, \boldsymbol{r}_s^\mathsf{T}\right]^\mathsf{T}$ and the corresponding observability matrix is given by

$$\boldsymbol{\mathcal{O}}(0,l) = \begin{bmatrix} \mathbf{h}_{a,r,s}^\mathsf{T}(0) & \mathbf{0}_{1\times 2} & -\mathbf{h}_{a,r,s}^\mathsf{T}(0) \\ \mathbf{h}_{a,r,s}^\mathsf{T}(1) & T\mathbf{h}_{a,r,s}^\mathsf{T}(1) & -\mathbf{h}_{a,r,s}^\mathsf{T}(1) \\ \vdots & \vdots & \vdots \\ \mathbf{h}_{a,r,s}^\mathsf{T}(l-1) & T(l-1)\mathbf{h}_{a,r,s}^\mathsf{T}(l-1) & -\mathbf{h}_{a,r,s}^\mathsf{T}(l-1) \end{bmatrix},$$

where $\mathbf{h}_{a,r,s}^\mathsf{T}(k) \triangleq \left[\frac{x_r(k)-x_s(k)}{\|\boldsymbol{r}_r(k)-\boldsymbol{r}_s(k)\|_2},\, \frac{y_r(k)-y_s(k)}{\|\boldsymbol{r}_r(t_k)-\boldsymbol{r}_s(k)\|_2}\right]$. An alternative expression for $\mathbf{h}_{a,r,s}^\mathsf{T}(k)$ is given by $\mathbf{h}_{a,r,s}^\mathsf{T}(k) = [\,\cos\theta_{r,s}(k),\, \sin\theta_{r,s}(k)\,]$, where $\theta_{r,s}(k)$ is the angle between the x-axis and the range vector connecting the receiver and the SOP at time instant k. In this representation, it is obvious that $\boldsymbol{\mathcal{O}}_L(0,l)$ has a rank of 3, since $\boldsymbol{\mathcal{O}}_1 = -\boldsymbol{\mathcal{O}}_5$, $\boldsymbol{\mathcal{O}}_2 = -\boldsymbol{\mathcal{O}}_6$, and $\sum_{i=1}^{4} \alpha_i\, \boldsymbol{\mathcal{O}}_i = \mathbf{0}$, with

$\alpha_1 \triangleq \frac{-y_r(0)+y_s(0)}{\dot{x}_r(0)}$, $\alpha_2 \triangleq \frac{x_r(0)-x_s(0)}{\dot{x}_r(0)}$, $\alpha_3 \triangleq \frac{-\dot{y}_r(0)}{\dot{x}_r(0)}$, and $\alpha_4 \triangleq 1$, where $\mathfrak{O}_i$ is the ith column of $\mathfrak{O}_L(0,l)$. The null-space of $\mathfrak{O}_L(0,l)$ for $l \geq 3$ can be shown to be

$$\mathcal{N}\left[\mathfrak{O}_L(0,l)\right] = \text{span}\left[\begin{array}{ccc} \boldsymbol{a}_1 & \boldsymbol{a}_2 & \boldsymbol{a}_3 \end{array}\right],$$

$$\boldsymbol{a}_1 \triangleq \boldsymbol{e}_1 + \boldsymbol{e}_5, \quad \boldsymbol{a}_2 \triangleq \boldsymbol{e}_2 + \boldsymbol{e}_6, \quad \boldsymbol{a}_3 \triangleq \sum_{i=1}^{4} \alpha_i \boldsymbol{e}_i,$$

where $\boldsymbol{e}_i$ is the standard basis vector consisting of a 1 in the ith element and zeros elsewhere. However, when the receiver's motion path is collinear with the SOP, the rank of $\mathfrak{O}_L(0,l)$ drops to 2, since in this case $\theta_{r,s}(0) = \cdots = \theta_{r,s}(l-1)$.

3.4 Scenarios Overview

The various scenarios considered in the observability analysis are outlined Table 3.1, where $n, m \in \mathbb{N}$. In Table 3.1, unknown means that no *a priori* knowledge about any of the states is available, whereas fully-known means that all the initial states are known. Thus, a fully-known receiver is one with known $\boldsymbol{x}_r(0)$, whereas a fully-known SOP is one with known $\boldsymbol{x}_s(0)$. On the other hand, partially-known means that only the initial position states are known. Thus, a partially-known receiver is one with known $\boldsymbol{r}_r(0)$, whereas a partially-known SOP is one with known $\boldsymbol{r}_s(0)$. For the cases of multiple SOPs, it is assumed that the SOPs are not colocated. Moreover, it is assumed that each SOP's classification, whether unknown, partially-known, or fully-known, is known to any receiver making use of that SOP.

Table 3.1: COpNav observability analysis scenarios considered

Case	Receiver(s)	SOP(s)
1	1 Unknown	1 Unknown
2	1 Unknown	m Partially-known
3	1 Unknown	1 Fully-known
4	1 Unknown	1 Fully-known & 1 Partially-known
5	n Partially-known	1 Unknown
6	n Partially-known	m Partially-known
7	1 Partially-known	1 Fully-known
8	1 Fully-known	1 Unknown

3.5 Linear Observability Analysis

This section analyzes the observability of the scenarios outlined in Table 3.1 for receivers with velocity random walk dynamics, i.e., $\boldsymbol{u} = 0$ in (2.2), through the linear observability test discussed in Subsection 3.1.2 [83, 84].

3.5.1 Preliminary Facts

The following facts will be invoked in the upcoming linear observability proofs. The rank of an arbitrary matrix $\mathbf{A} \in \mathbb{R}^{m \times n}$ is the maximal number of linearly independent rows or columns; more specifically, $\text{rank}[\mathbf{A}] \leq \min\{m, n\}$.

In a COpNav environment comprising n receivers and m SOPs, the state transition matrix raised to the kth power can be shown to be

$$\mathbf{F}^k = \text{diag}\left[\, \mathbf{F}_{r_1}^k, \ldots, \mathbf{F}_{r_n}^k, \mathbf{F}_{s_1}^k, \ldots, \mathbf{F}_{s_m}^k \,\right], \tag{3.12}$$

where $\mathbf{F}_{r_i}$ and $\mathbf{F}_{s_j}$ are the state transition matrices for the ith receiver and jth SOP, respectively.

Moreover, it can be readily verified that

$$\boldsymbol{e}_i^{\mathsf{T}}\mathbf{F}_r^k = \begin{cases} \boldsymbol{e}_i^{\mathsf{T}} + kT\boldsymbol{e}_{i+2}^{\mathsf{T}}, & i = 1, 2; \\ \boldsymbol{e}_i^{\mathsf{T}} + kT\boldsymbol{e}_{i+1}^{\mathsf{T}}, & i = 5; \\ \boldsymbol{e}_i^{\mathsf{T}}, & i = 3, 4, 6 \end{cases} \tag{3.13}$$

$$\boldsymbol{e}_i^{\mathsf{T}}\mathbf{F}_s^k = \begin{cases} \boldsymbol{e}_i^{\mathsf{T}}, & i = 1, 2, 4; \\ \boldsymbol{e}_i^{\mathsf{T}} + kT\boldsymbol{e}_{i+1}^{\mathsf{T}}, & i = 3. \end{cases} \tag{3.14}$$

The Jacobian vector of the observation corresponding to the pseudorange measurement made by receiver i on SOP j will have the structure

$$\mathbf{H}(k) = \begin{bmatrix} \mathbf{0} & \cdots & \mathbf{0} & \mathbf{h}_{b,r_i,s_j}^{\mathsf{T}}(k) & \mathbf{0} & \cdots & \mathbf{0} & \mathbf{h}_{c,r_i,s_j}^{\mathsf{T}}(k) & \mathbf{0} & \cdots & \mathbf{0} \end{bmatrix} \tag{3.15}$$

$$\begin{aligned} \mathbf{h}_{b,r_i,s_j}^{\mathsf{T}}(k) &\triangleq \begin{bmatrix} \mathbf{h}_{a,r_i,s_j}^{\mathsf{T}}(k) & \mathbf{0}_{1\times 2} & c & 0 \end{bmatrix} \\ \mathbf{h}_{c,r_i,s_j}^{\mathsf{T}}(k) &\triangleq \begin{bmatrix} -\mathbf{h}_{a,r_i,s_j}^{\mathsf{T}}(k) & -c & 0 \end{bmatrix}, \end{aligned}$$

where $\mathbf{h}_{a,r_i,s_j}^{\mathsf{T}}(k) = \left[\frac{x_{r_i}(k)-x_{s_j}(k)}{\|\boldsymbol{r}_{r_i}(k)-\boldsymbol{r}_{s_j}(k)\|_2}, \frac{y_{r_i}(k)-y_{s_j}(k)}{\|\boldsymbol{r}_{r_i}(k)-\boldsymbol{r}_{s_j}(k)\|_2}\right]$. It can be readily verified that

$$\mathbf{h}_{b,r_i,s_j}^{\mathsf{T}}(k)\mathbf{F}_r^k = \mathbf{h}_{d,r_i,s_j}^{\mathsf{T}}(k) \tag{3.16}$$

$$\mathbf{h}_{c,r_i,s_j}^{\mathsf{T}}(k)\mathbf{F}_s^k = \mathbf{h}_{e,r_i,s_j}^{\mathsf{T}}(k) \tag{3.17}$$

$$\begin{aligned} \mathbf{h}_{d,r_i,s_j}^{\mathsf{T}}(k) &\triangleq \begin{bmatrix} \mathbf{h}_{a,r_i,s_j}^{\mathsf{T}}(k) & kT\mathbf{h}_{a,r_i,s_j}^{\mathsf{T}}(k) & c & kT \end{bmatrix} \\ \mathbf{h}_{e,r_i,s_j}^{\mathsf{T}}(k) &\triangleq \begin{bmatrix} -\mathbf{h}_{a,r_i,s_j}^{\mathsf{T}}(k) & -c & -kT \end{bmatrix}. \end{aligned}$$

3.5.2 Linear Observability Results

Theorem 3.5.1. *A COpNav environment with one unknown receiver and one unknown SOP is unobservable. Moreover, the observability matrix $\mathbf{O}_L(0, l)$ is rank-deficient by 5, $\forall\, l \geq 5$.*

Proof. The state vector for this case is given by $\boldsymbol{x} = \left[\boldsymbol{x}_r^{\mathsf{T}}, \boldsymbol{x}_s^{\mathsf{T}}\right]^{\mathsf{T}}$. Invoking (3.12) and (3.15)-(3.17), it can be seen that the rank of $\boldsymbol{\mathcal{O}}_L(0,l)$ is one at the first time segment, and the rank increments by one as each additional time segment is appended up to $l = 5$, since the corresponding additional rows are linearly independent. At the fifth time segment, $\text{rank}[\boldsymbol{\mathcal{O}}_L(0,5)] = 5$, and the rank never increases further, since only $\boldsymbol{\mathcal{O}}_i$, $i = 1, 2, 3, 5, 6$, are linearly independent, $\forall l \geq 5$. This can be shown by noting that $\boldsymbol{\mathcal{O}}_1 = -\boldsymbol{\mathcal{O}}_7$, $\boldsymbol{\mathcal{O}}_2 = -\boldsymbol{\mathcal{O}}_8$, $\boldsymbol{\mathcal{O}}_5 = -\boldsymbol{\mathcal{O}}_9$, $\boldsymbol{\mathcal{O}}_6 = -\boldsymbol{\mathcal{O}}_{10}$, and $\sum_{i=1}^{4} \alpha_i \boldsymbol{\mathcal{O}}_i = \boldsymbol{0}$, with $\alpha_1 \triangleq \frac{-y_r(0)+y_s(0)}{\dot{x}_r(0)}$, $\alpha_2 \triangleq \frac{x_r(0)-x_s(0)}{\dot{x}_r(0)}$, $\alpha_3 \triangleq \frac{-\dot{y}_r(0)}{\dot{x}_r(0)}$, and $\alpha_4 \triangleq 1$. The null-space of $\boldsymbol{\mathcal{O}}_L(0,l)$ for $l \geq 5$ can be shown to be

$$\mathcal{N}\left[\boldsymbol{\mathcal{O}}_L(0,l)\right] = \text{span}\left[\begin{array}{ccccc} \boldsymbol{n}_1 & \boldsymbol{n}_2 & \boldsymbol{n}_3 & \boldsymbol{n}_4 & \boldsymbol{n}_5 \end{array}\right],$$

$$\boldsymbol{n}_1 \triangleq \boldsymbol{e}_6 + \boldsymbol{e}_{10},\ \boldsymbol{n}_2 \triangleq \boldsymbol{e}_5 + \boldsymbol{e}_9,\ \boldsymbol{n}_3 \triangleq \boldsymbol{e}_2 + \boldsymbol{e}_8,\ \boldsymbol{n}_4 \triangleq \boldsymbol{e}_1 + \boldsymbol{e}_7,\ \boldsymbol{n}_5 \triangleq \sum_{i=1}^{4} \alpha_i \boldsymbol{e}_i.$$

□

The structure of $\mathcal{N}\left[\boldsymbol{\mathcal{O}}_L(0,l)\right]$ reveals the following conclusions. First, the absence of a row of zeros in the matrix of null-space basis vectors $\{\boldsymbol{n}_i\}_{i=1}^{5}$ indicates that none of the states is orthogonal to the unobservable subspace, which means that all the states lie within the unobservable subspace. Therefore, none of the states is directly observable. Second, a shift of the receiver and SOP positions by ε_x units in the x-direction and ε_y units in the y-direction, where $\varepsilon_x, \varepsilon_y \in \mathbb{R}$, is unobservable, since this shift, denoted as $\boldsymbol{\lambda} = \varepsilon_y \boldsymbol{n}_3 + \varepsilon_x \boldsymbol{n}_4$ lies in the null-space of $\boldsymbol{\mathcal{O}}_L(0,l)$. The same interpretation can be made with

respect to a shift in the δt-$\dot{\delta} t$ space being unobservable as a result of $\boldsymbol{n}_1$ and $\boldsymbol{n}_2$. Third, a rotation by an angle ϕ around the SOP is unobservable. To see this, without loss of generality, assume that the SOP is located at the origin. A rotation at an angle ϕ will transform the coordinate frame from (x, y) to (x', y'). Therefore, the position and velocity states in the new coordinate frame can be computed from

$$\begin{bmatrix} \boldsymbol{r}'_r \\ \dot{\boldsymbol{r}}'_r \end{bmatrix} = \begin{bmatrix} \mathbf{T}(\phi) & \mathbf{0} \\ \mathbf{0} & \mathbf{T}(\phi) \end{bmatrix} \begin{bmatrix} \boldsymbol{r}_r \\ \dot{\boldsymbol{r}}_r \end{bmatrix}, \quad \mathbf{T}(\phi) \triangleq \begin{bmatrix} \cos\phi & -\sin\phi \\ \sin\phi & \cos\phi \end{bmatrix}.$$

For small ϕ, the small angle approximations $\cos\phi \approx 1$ and $\sin\phi \approx \phi$ can be invoked in the rotation matrix $\mathbf{T}(\phi)$. Consequently, it can be readily shown that the transformed state vector can be expressed as $\boldsymbol{x}' = \boldsymbol{x} + \frac{\phi}{\dot{x}_r(0)}\boldsymbol{n}_5$. Since $\boldsymbol{n}_5 \in \mathcal{N}\left[\mathfrak{O}_L(0, l)\right]$, then $\frac{\phi}{\dot{x}_r(0)}\boldsymbol{n}_5 \in \mathcal{N}\left[\mathfrak{O}_L(0, l)\right]$, and such term will be unobservable from the measurements.

Theorem 3.5.2. *A COpNav environment with one unknown receiver and m partially-known SOPs is unobservable. Moreover, the observability matrix $\mathfrak{O}_L(0, l)$ is rank-deficient by 3 for $m = 1$, $\forall\, l \geq 5$, and rank-deficient by 2 for $m \geq 2$, $\forall\, l \geq 4$.*

Proof. The state vector for this case is given by $\boldsymbol{x} = \left[\, \boldsymbol{x}_r^{\mathsf{T}},\, \boldsymbol{x}_{s_1}^{\mathsf{T}},\, \ldots,\, \boldsymbol{x}_{s_m}^{\mathsf{T}} \,\right]^{\mathsf{T}}$. Knowledge of the SOPs' positions is equivalent to having an observation Jacobian matrix of the form

$$\mathbf{H}(k) = \begin{bmatrix} \mathbf{h}_{b,r,s_1}^{\mathsf{T}}(k) & \mathbf{h}_{c,r,s_1}^{\mathsf{T}}(k) & \mathbf{0} & \cdots & \mathbf{0} \\ \mathbf{h}_{b,r,s_2}^{\mathsf{T}}(k) & \mathbf{0} & \mathbf{h}_{c,r,s_2}^{\mathsf{T}}(k) & \cdots & \mathbf{0} \\ \vdots & \vdots & \vdots & \ddots & \vdots \\ \mathbf{h}_{b,r,s_m}^{\mathsf{T}}(k) & \mathbf{0} & \mathbf{0} & \cdots & \mathbf{h}_{c,r,s_m}^{\mathsf{T}}(k) \\ \mathbf{0} & [\mathbf{I}_{2\times 2}\ \mathbf{0}_{2\times 2}] & \mathbf{0} & \cdots & \mathbf{0} \\ \mathbf{0} & \mathbf{0} & [\mathbf{I}_{2\times 2}\ \mathbf{0}_{2\times 2}] & \cdots & \mathbf{0} \\ \vdots & \vdots & \mathbf{0} & \ddots & \vdots \\ \mathbf{0} & \mathbf{0} & \mathbf{0} & \cdots & [\mathbf{I}_{2\times 2}\ \mathbf{0}_{2\times 2}] \end{bmatrix}.$$

Noting that $\mathbf{H}(k) \in \mathbb{R}^{(3m)\times(4m+6)}$ and invoking (3.12)-(3.17), it can be be seen that $\text{rank}\,[\boldsymbol{\mathfrak{O}}_L(0,1)] = 3m$, $\forall m$, since all the rows are linearly independent. Adding a second time segment results in an observability matrix with $\text{rank}\,[\boldsymbol{\mathfrak{O}}_L(0,2)] = 4m$, $\forall m$, since the first $4m$ rows are linearly independent, while rows $m+1,\ldots,3m$ are identical to rows $4m+1,\ldots,6m$, respectively. Adding a third time segment results in an observability matrix with

$$\text{rank}\,[\boldsymbol{\mathfrak{O}}_L(0,3)] = \begin{cases} 5m, & m \leq 3; \\ 4m+4, & m > 3. \end{cases} \tag{3.18}$$

For $m \leq 3$, (3.18) can be shown by noting that rows $1,\ldots,4m$ and $6m+i$, where $i = 1,2,\ldots,m$ are linearly independent, while rows $m+1,\ldots,3m$ are identical to rows $4m+1,\ldots,6m$ and rows $7m+1,\ldots,9m$, respectively. For $m > 3$, (3.18) can be shown by noting that columns $1,\ldots,4m+4$ are linearly independent, while the last 2 columns are linearly dependent, namely $\boldsymbol{\mathfrak{O}}_{4m+5} = -\sum_{i=0}^{m-1} \boldsymbol{\mathfrak{O}}_{4i+5}$ and $\boldsymbol{\mathfrak{O}}_{4m+6} = -\sum_{i=0}^{m-1} \boldsymbol{\mathfrak{O}}_{4i+6}$. Adding a fourth time segment results in an observability matrix with

$$\text{rank}\,[\boldsymbol{\mathfrak{O}}_L(0,4)] = \begin{cases} 6, & m = 1; \\ 4m+4, & m \geq 2. \end{cases} \tag{3.19}$$

For $m = 1$, (3.19) can be shown by noting that rows $1, 2, 3, 4, 7, 10$ are linearly independent, while rows $2 + 3i$ and rows $3 + 3i$, for $i = 0, 1, 2, 3$ are identical. For $m \geq 2$, (3.19) can be shown by noting that columns $1, \ldots, 4m + 4$ are linearly independent, while the last 2 columns are linearly dependent, namely $\mathfrak{O}_{4m+5} = -\sum_{i=0}^{m-1} \mathfrak{O}_{4i+5}$ and $\mathfrak{O}_{4m+6} = -\sum_{i=0}^{m-1} \mathfrak{O}_{4i+6}$. For $m \geq 2$, adding more time segments does not improve the rank any further as the last two columns will always be linearly dependent on the previous columns. However, for $m = 1$ a fifth time segment increases the rank by one, while adding additional time segments beyond 5 does not improve the rank any further. This can be shown by noting that $\mathfrak{O}_i$, $i = 1, 2, 3, 5, 6, 7, 8$, are linearly independent, while $\mathfrak{O}_5 = -\mathfrak{O}_9$, $\mathfrak{O}_6 = -\mathfrak{O}_{10}$, and $\sum_{i=1}^{4} \alpha_i \mathfrak{O}_i = \mathbf{0}$.

For $m = 1$, the null-space of $\mathfrak{O}_L(0, l)$, $l \geq 5$, can be shown to be

$$\mathcal{N}[\mathfrak{O}_L(0,l)] \;=\; \text{span}\left[\begin{array}{ccc} \boldsymbol{n}_1 & \boldsymbol{n}_2 & \boldsymbol{n}_5 \end{array}\right].$$

For $m \geq 2$, the null-space of $\mathfrak{O}_L(0, l)$, $l \geq 4$, can be shown to be

$$\mathcal{N}[\mathfrak{O}_L(0,l)] \;=\; \text{span}\left[\begin{array}{cc} \boldsymbol{n}_6 & \boldsymbol{n}_7 \end{array}\right],$$

$$\begin{aligned}
\boldsymbol{n}_6 &\triangleq \left[\begin{array}{cccccc} \boldsymbol{n}_{6,r}^{\mathsf{T}} & \boldsymbol{n}_{6,s_1}^{\mathsf{T}} & \boldsymbol{n}_{6,s_2}^{\mathsf{T}} & \cdots & \boldsymbol{n}_{6,s_m}^{\mathsf{T}} \end{array}\right]^{\mathsf{T}} \\
\boldsymbol{n}_7 &\triangleq \left[\begin{array}{cccccc} \boldsymbol{n}_{7,r}^{\mathsf{T}} & \boldsymbol{n}_{7,s_1}^{\mathsf{T}} & \boldsymbol{n}_{7,s_2}^{\mathsf{T}} & \cdots & \boldsymbol{n}_{7,s_m}^{\mathsf{T}} \end{array}\right]^{\mathsf{T}} \\
\boldsymbol{n}_{6,r}^{\mathsf{T}} &\triangleq \gamma \boldsymbol{e}_5^{\mathsf{T}} - \mu \boldsymbol{e}_6^{\mathsf{T}}, \quad \boldsymbol{n}_{7,r}^{\mathsf{T}} \triangleq \mu \boldsymbol{e}_5^{\mathsf{T}} + \gamma \boldsymbol{e}_6^{\mathsf{T}} \\
\boldsymbol{n}_{6,s_i}^{\mathsf{T}} &\triangleq \gamma \boldsymbol{e}_3^{\mathsf{T}} - \mu \boldsymbol{e}_4^{\mathsf{T}}, \quad \boldsymbol{n}_{7,s_i}^{\mathsf{T}} \triangleq \mu \boldsymbol{e}_5^{\mathsf{T}} + \gamma \boldsymbol{e}_6^{\mathsf{T}}, \quad i = 1, 2, \ldots, m \\
\gamma &\triangleq \frac{-y_r(0) + \sum_{i=1}^{m} y_{s_i}(0)}{\dot{y}_r(0)}, \quad \mu \triangleq \frac{x_r(0) - \sum_{i=1}^{m} x_{s_i}(0)}{\dot{x}_r(0)}.
\end{aligned}$$

□

The structure of $\mathcal{N}\left[\mathfrak{O}_L(0,l)\right]$ reveals that for $m=1$, none of the states is directly observable except x_{s_i} and y_{s_i}, which are observable by construction. However, for $m \geq 2$, the receiver's position and velocity states, x_r, y_r, $\dot{x}_r$, and $\dot{y}_r$, become observable, but the receiver and SOPs clock bias and drift states, δt_r, $\dot{\delta} t_r$, δt_{s_i}, and $\dot{\delta} t_{s_i}$, remain unobservable.

Theorem 3.5.3. *A COpNav environment with one unknown receiver and one fully-known SOP is unobservable. Moreover, the observability matrix* $\mathfrak{O}_L(0,l)$ *is rank-deficient by* 1, $\forall\, l \geq 5$.

Proof. The state vector for this case is given by $\boldsymbol{x} = \left[\, \boldsymbol{x}_r^{\mathsf{T}},\, \boldsymbol{x}_s^{\mathsf{T}} \,\right]^{\mathsf{T}}$. Full knowledge of the SOP is equivalent to having an observation Jacobian matrix

$$\mathbf{H}(k) = \begin{bmatrix} \mathbf{h}_{b,r,s}^{\mathsf{T}}(k) & \mathbf{h}_{c,r,s}^{\mathsf{T}}(k) \\ \mathbf{0} & \mathbf{I}_{4\times 4} \end{bmatrix}. \tag{3.20}$$

Invoking (3.12)-(3.17), it can be be seen that $\operatorname{rank}\left[\mathfrak{O}_L(0,l)\right] = 5$ at the first time segment, since the rows are linearly independent. The rank increments by one as each additional time segment is appended up to $l=5$, since rows 2, 3, 4, and 5 are identical to rows $2+5(l-1)$, $3+5(l-1)$, $4+5(l-1)$, and $5+5(l-1)$, respectively, while the first five rows are linearly independent of rows $1+5(l-1)$. The rank stops improving at the fifth time segment, whereat $\operatorname{rank}[\mathfrak{O}_L(0,5)] = 9$. The rank never increases further, since $\mathfrak{O}_4 = -\sum_{i=1}^{3} \alpha_i\, \mathfrak{O}_i$. The null-space of $\mathfrak{O}_L(0,l)$, $l \geq 5$, can be shown to be

$$\mathcal{N}\left[\mathfrak{O}_L(0,l)\right] \;=\; \operatorname{span}\left[\; \boldsymbol{n}_5 \;\right].$$

□

The structure of $\mathcal{N}[\boldsymbol{\mathfrak{O}}_L(0,l)]$ reveals that of the receiver's states, only the receiver clock bias δt_r and clock drift $\dot{\delta t}_r$ are observable as they are orthogonal to the unobservable subspace, while SOP states are observable by construction.

Theorem 3.5.4. *A COpNav environment with one unknown receiver, one fully-known SOP, and one partially-known SOP is observable,* $\forall\, l \geq 4$.

Proof. The state vector for this case is given by $\boldsymbol{x} = \left[\, \boldsymbol{x}_r^{\mathsf{T}},\, \boldsymbol{x}_{s_1}^{\mathsf{T}}, \boldsymbol{x}_{s_2}^{\mathsf{T}} \,\right]^{\mathsf{T}}$. Full knowledge of one SOP and partial knowledge of the other is equivalent to having an observation Jacobian matrix of the form

$$\mathbf{H}(k) = \begin{bmatrix} \mathbf{h}_{b,r,s_1}^{\mathsf{T}}(k) & \mathbf{h}_{c,r,s_1}^{\mathsf{T}}(k) & \mathbf{0} \\ \mathbf{h}_{b,r,s_2}^{\mathsf{T}}(k) & \mathbf{0} & \mathbf{h}_{c,r,s_2}^{\mathsf{T}}(k) \\ \mathbf{0} & \mathbf{I}_{4\times 4} & \mathbf{0} \\ \mathbf{0} & \mathbf{0} & [\mathbf{I}_{2\times 2}\ \mathbf{0}_{2\times 2}] \end{bmatrix}. \tag{3.21}$$

Invoking (3.12)-(3.17), it can be seen that the observability matrix $\boldsymbol{\mathfrak{O}}_L(0,l)$ has a rank of 8 at the first time segment, since all the rows are linearly independent. The rank keeps increments by two as each additional time segment is appended up to $l = 4$. Adding a fourth time segment results in an observability matrix whose rank is 14 (full-rank). This can be shown by noting that the first 8 rows are linearly independent along with rows $9+8(l-2)$ and $10+8(l-2)$, for $l = 2,3,4$. Moreover, rows $i+8(l-1)$ for $i = 3,4,6,7,8$ and $l = 1$ are identical to the corresponding rows for $l = 2,3,\ldots$. Finally, $\boldsymbol{\mathfrak{O}}_{13+8(l-2)}^{\mathsf{T}} = \boldsymbol{\mathfrak{O}}_5^{\mathsf{T}} + T(l-1)\boldsymbol{\mathfrak{O}}_6^{\mathsf{T}}$, for $l = 2,3,\ldots$, where $\boldsymbol{\mathfrak{O}}_i^{\mathsf{T}}$ is the ith row of the corresponding observability matrix $\boldsymbol{\mathfrak{O}}_L(0,l)$. □

Theorem 3.5.5. *A COpNav environment with n partially-known receivers and one unknown SOP is unobservable. Moreover, the observability matrix $\mathfrak{O}_L(0,l)$ is rank-deficient by 2, $\forall\, l \geq 3$.*

Proof. The state vector for this case is given by $\boldsymbol{x} = \left[\, \boldsymbol{x}_{r_1}^{\mathsf{T}}, \ldots, \boldsymbol{x}_{r_n}^{\mathsf{T}}, \boldsymbol{x}_{s}^{\mathsf{T}} \,\right]^{\mathsf{T}}$. Partial knowledge of the n receivers is equivalent to having an observation Jacobian matrix of the form

$$\mathbf{H}(k) = \begin{bmatrix} \mathbf{h}_{b,r_1,s}^{\mathsf{T}}(k) & \mathbf{0} & \cdots & \mathbf{0} & \mathbf{h}_{c,r_1,s}^{\mathsf{T}}(k) \\ [\mathbf{I}_{2\times 2}\, \mathbf{0}_{2\times 4}] & \mathbf{0} & \cdots & \mathbf{0} & \mathbf{0} \\ \vdots & \vdots & \ddots & \vdots & \vdots \\ \mathbf{0} & \mathbf{0} & \cdots & \mathbf{h}_{b,r_n,s}^{\mathsf{T}}(k) & \mathbf{h}_{c,r_n,s}^{\mathsf{T}}(k) \\ \mathbf{0} & \mathbf{0} & \cdots & [\mathbf{I}_{2\times 2}\, \mathbf{0}_{2\times 4}] & \mathbf{0} \end{bmatrix}.$$

Noting that $\mathbf{H}(k) \in \mathbb{R}^{(3n)\times(6n+4)}$ and invoking (3.12)-(3.17), it can be be seen that $\operatorname{rank}[\mathfrak{O}_L(0,1)] = 3n$ and $\operatorname{rank}[\mathfrak{O}_L(0,2)] = 6n$, since in both cases all rows are linearly independent. Adding more time segments results in $\operatorname{rank}[\mathfrak{O}_L(0,l)] = 6n+2$, $\forall\, l \geq 3$, since columns $1, 2, \ldots, 6n+2$ are linearly independent, whereas the last two columns are linearly dependent. In particular, $\mathfrak{O}_{6n+3} = -\sum_{i=1}^{n} \mathfrak{O}_{6i+5}$ and $\mathfrak{O}_{6n+4} = -\sum_{i=1}^{n} \mathfrak{O}_{6i+6}$. The null-space of $\mathfrak{O}_L(0,l)$, $l \geq 3$, can be shown to be

$$\mathcal{N}[\mathfrak{O}_L(0,l)] \;=\; \operatorname{span}\left[\; \boldsymbol{n}_8 \quad \boldsymbol{n}_9 \;\right],$$

$$\begin{aligned} \boldsymbol{n}_8 &\triangleq \left[\; \boldsymbol{n}_{8,r_1}^{\mathsf{T}} \quad \boldsymbol{n}_{8,r_2}^{\mathsf{T}} \quad \cdots \quad \boldsymbol{n}_{8,r_n}^{\mathsf{T}} \quad \boldsymbol{n}_{8,s}^{\mathsf{T}} \;\right]^{\mathsf{T}} \\ \boldsymbol{n}_9 &\triangleq \left[\; \boldsymbol{n}_{9,r_1}^{\mathsf{T}} \quad \boldsymbol{n}_{9,r_2}^{\mathsf{T}} \quad \cdots \quad \boldsymbol{n}_{9,r_n}^{\mathsf{T}} \quad \boldsymbol{n}_{9,s}^{\mathsf{T}} \;\right]^{\mathsf{T}} \\ \boldsymbol{n}_{8,r_i}^{\mathsf{T}} &\triangleq \xi \boldsymbol{e}_5^{\mathsf{T}} - \eta \boldsymbol{e}_6^{\mathsf{T}}, \quad \boldsymbol{n}_{9,r_i}^{\mathsf{T}} \triangleq \eta \boldsymbol{e}_5^{\mathsf{T}} + \xi \boldsymbol{e}_6^{\mathsf{T}}, \quad i = 1, 2, \ldots, n \\ \boldsymbol{n}_{8,s}^{\mathsf{T}} &\triangleq \xi \boldsymbol{e}_3^{\mathsf{T}} - \eta \boldsymbol{e}_4^{\mathsf{T}}, \quad \boldsymbol{n}_{9,s}^{\mathsf{T}} \triangleq \eta \boldsymbol{e}_3^{\mathsf{T}} + \xi \boldsymbol{e}_4^{\mathsf{T}} \end{aligned}$$

$$\xi \triangleq \frac{-\left[\sum_{i=1}^{n} y_{r_i}(0)\right] + y_s(0)}{\sum_{i=1}^{n} \dot{y}_{r_i}(0)}, \quad \eta \triangleq \frac{\left[\sum_{i=1}^{n} x_{r_i}(0)\right] - x_s(0)}{\sum_{i=1}^{n} \dot{x}_{r_i}(0)}.$$

□

The structure of $\mathcal{N}\left[\boldsymbol{\mathcal{O}}_L(0,l)\right]$ reveals that the receivers velocity states and the SOP's position states are observable. However, the receivers' and the SOP's clock bias and drift states are not observable. Recall that the receivers' position states are observable by construction.

Theorem 3.5.6. *A COpNav environment with n partially-known receivers and m partially-known SOPs is unobservable. Moreover, the observability matrix* $\boldsymbol{\mathcal{O}}_L(0,l)$ *is rank-deficient by* 2, $\forall\, l \geq 2$.

Proof. The state vector for this case is given by $\boldsymbol{x} = \left[\boldsymbol{x}_{r_1}^{\mathsf{T}}, \ldots, \boldsymbol{x}_{r_n}^{\mathsf{T}}, \boldsymbol{x}_{s_1}^{\mathsf{T}}, \ldots, \boldsymbol{x}_{s_m}^{\mathsf{T}}\right]^{\mathsf{T}}$. Partial knowledge of the receivers and SOPs is equivalent to having an observation Jacobian matrix of the form

$$\mathbf{H}(k) = \begin{bmatrix} \mathbf{H}_{b,r_1,s} & \mathbf{0} & \mathbf{0} & \mathbf{H}_{c,r_1,s} & \mathbf{0} & \mathbf{0} \\ \mathbf{0} & \ddots & \vdots & \mathbf{0} & \ddots & \mathbf{0} \\ \mathbf{0} & \cdots & \mathbf{H}_{b,r_n,s} & \mathbf{0} & \cdots & \mathbf{H}_{c,r_n,s} \\ \mathbf{0} & \cdots & \mathbf{0} & [\mathbf{I}_{2\times 2} \;\; \mathbf{0}_{2\times 2}] & \mathbf{0} & \mathbf{0} \\ \vdots & \ddots & \vdots & \mathbf{0} & \ddots & \vdots \\ \mathbf{0} & \cdots & \mathbf{0} & \mathbf{0} & \cdots & [\mathbf{I}_{2\times 2} \;\; \mathbf{0}_{2\times 2}] \end{bmatrix}$$

$$\mathbf{H}_{b,r_i,s}(k) \triangleq \begin{bmatrix} \mathbf{h}_{b,r_i,s_1}^{\mathsf{T}}(k) \\ \vdots \\ \mathbf{h}_{b,r_i,s_m}^{\mathsf{T}}(k) \\ \mathbf{I}_{2\times 2} \;\; \mathbf{0}_{2\times 4} \end{bmatrix}, \; \mathbf{H}_{c,r_i,s}(k) \triangleq \begin{bmatrix} \mathbf{h}_{c,r_i,s_1}^{\mathsf{T}}(k) \\ \vdots \\ \mathbf{h}_{c,r_i,s_m}^{\mathsf{T}}(k) \\ \mathbf{0}_{2\times 4} \end{bmatrix}, \; i = 1, \ldots, n.$$

Noting that $\mathbf{H}(k) \in \mathbb{R}^{(mn+2n+2m)\times(6n+4m)}$ and invoking (3.12)-(3.17), it can be seen that $\operatorname{rank}\left[\boldsymbol{\mathcal{O}}_L(0,1)\right] = 3n + 3m - 1$. This can be shown by noting that the columns of $\boldsymbol{\mathcal{O}}(0,1)$ have the following properties:

- linearly independent columns: $\mathfrak{O}_{1+6i}$, $\mathfrak{O}_{2+6i}$, $\mathfrak{O}_{5+6i}$, $\mathfrak{O}_{6n+1+4j}$, $\mathfrak{O}_{6n+2+4j}$, and $\mathfrak{O}_{6n+3+4(l-1)}$; with $i = 0, 1, \ldots, n$, $j = 0, 1, \ldots, m$, and $l = 1, 2, \ldots, j$.
- columns of zeros: $\mathfrak{O}_{3+6i}$, $\mathfrak{O}_{4+6i}$, $\mathfrak{O}_{6+6i}$, $\mathfrak{O}_{6n+4+4j}$; with $i = 0, 1, \ldots, n$, and $j = 0, 1, \ldots, m$
- linearly dependent columns: $\mathfrak{O}_{6n+3+4j} = -\left[\sum_{l=1}^{n} \mathfrak{O}_{6l-1} + \sum_{l=0}^{j-1} \mathfrak{O}_{6n+3+4l}\right]$; with $j = 0, \ldots, m$

Next, it is noted that $\mathfrak{O}_L(0,l) \in \mathbb{R}^{[l(mn+2n+2m)]\times(6n+4m)}$; hence the rank of $\mathfrak{O}_L(0,l)$ will be determined by the number of linearly independent columns, since the matrix will have more rows than columns $\forall l \geq 2$. It can be seen that $\text{rank}\,[\mathfrak{O}_L(0,l)] = 6n+4m-2, \forall l \geq 2$, i.e. the l-step observability matrix is rank-deficient by 2. This can be shown by noting that the first $6n+4m-2$ columns are linearly independent, while the last two columns are linearly dependent, such that

$$\mathfrak{O}_{6n+4m-q} \;=\; -\left[\sum_{l=1}^{n} \mathfrak{O}_{6l-q} + \sum_{l=0}^{j-1} \mathfrak{O}_{6n+4-q+4l}\right],$$

where $q = 0, 1$ and $j = 0, 1, \ldots, m$. The null-space of $\mathfrak{O}_L(0,l)$, $l \geq 3$, can be shown to be

$$\mathcal{N}\left[\mathfrak{O}_L(0,l)\right] \;=\; \text{span}\left[\begin{array}{cc} \boldsymbol{n}_{10} & \boldsymbol{n}_{11} \end{array}\right],$$

$$\begin{aligned}
\boldsymbol{n}_{10} &\triangleq \left[\begin{array}{ccccccc} \boldsymbol{n}_{10,r_1}^{\mathsf{T}} & \cdots & \boldsymbol{n}_{10,r_n}^{\mathsf{T}} & \boldsymbol{n}_{10,s_1}^{\mathsf{T}} & \cdots & \boldsymbol{n}_{10,s_m}^{\mathsf{T}} \end{array}\right]^{\mathsf{T}} \\
\boldsymbol{n}_{11} &\triangleq \left[\begin{array}{ccccccc} \boldsymbol{n}_{11,r_1}^{\mathsf{T}} & \cdots & \boldsymbol{n}_{11,r_n}^{\mathsf{T}} & \boldsymbol{n}_{11,s_1}^{\mathsf{T}} & \cdots & \boldsymbol{n}_{11,s_m}^{\mathsf{T}} \end{array}\right]^{\mathsf{T}} \\
\boldsymbol{n}_{10,r_i}^{\mathsf{T}} &\triangleq \beta \boldsymbol{e}_5^{\mathsf{T}} - \zeta \boldsymbol{e}_6^{\mathsf{T}}, \quad \boldsymbol{n}_{9,r_i}^{\mathsf{T}} \triangleq \zeta \boldsymbol{e}_5^{\mathsf{T}} + \beta \boldsymbol{e}_6^{\mathsf{T}}, \quad i = 1, 2, \ldots, n \\
\boldsymbol{n}_{11,s_j}^{\mathsf{T}} &\triangleq \beta \boldsymbol{e}_3^{\mathsf{T}} - \zeta \boldsymbol{e}_4^{\mathsf{T}}, \quad \boldsymbol{n}_{9,s_j}^{\mathsf{T}} \triangleq \zeta \boldsymbol{e}_3^{\mathsf{T}} + \beta \boldsymbol{e}_4^{\mathsf{T}}, \quad j = 1, 2, \ldots, m
\end{aligned}$$

$$\beta \triangleq \frac{-\left[\sum_{i=1}^{n} y_{r_i}(0)\right] + \left[\sum_{j=1}^{m} y_{s_i}(0)\right]}{\sum_{i=1}^{n} \dot{y}_{r_i}(0)}, \quad \zeta \triangleq \frac{\left[\sum_{i=1}^{n} x_{r_i}(0)\right] - \left[\sum_{j=1}^{m} x_{s_i}(0)\right]}{\sum_{i=1}^{n} \dot{x}_{r_i}(0)}.$$

□

The structure of $\mathcal{N}\left[\mathfrak{O}_L(0,l)\right]$ reveals that the receivers velocity states are observable. However, the receivers' and SOPs' clock bias and drift states are not observable. Recall that the receivers' position states are observable by construction.

Theorem 3.5.7. *A COpNav environment with one partially-known receiver and one fully-known SOP is observable,* $\forall\, l \geq 2$.

Proof. The state vector for this case is given by $\boldsymbol{x} = \left[\, \boldsymbol{x}_r^{\mathsf{T}}, \boldsymbol{x}_s^{\mathsf{T}} \,\right]^{\mathsf{T}}$. Partial knowledge of the receiver and full knowledge of the SOP is equivalent to having an observation Jacobian matrix of the form

$$\mathbf{H}(k) = \begin{bmatrix} \mathbf{h}_{b,r,s}^{\mathsf{T}}(k) & \mathbf{h}_{c,r,s}^{\mathsf{T}}(k) \\ [\mathbf{I}_{2\times 2}\, \mathbf{0}_{2\times 4}] & \mathbf{0} \\ \mathbf{0} & \mathbf{I}_{4\times 4} \end{bmatrix}. \tag{3.22}$$

Invoking (3.12)-(3.17), it can be be seen that $\operatorname{rank}\left[\mathfrak{O}_L(0,1)\right] = 7$, since all the rows are linearly independent. Adding more time segments yields a full-rank $\mathfrak{O}_L(0,l)$, namely $\operatorname{rank}\left[\mathfrak{O}_L(0,l)\right] = 10$, $\forall l \geq 2$, since the first ten rows are linearly independent, while rows $4+7(l-1)$, $5+7(l-1)$, and $7+7(l-1)$ for $l = 1$ are identical to the corresponding rows for $l = 2, 3, \ldots$, and rows $\mathfrak{O}_{6+7(l-1)}^{\mathsf{T}}$ are linearly dependent, such that $\mathfrak{O}_{6+7(l-1)}^{\mathsf{T}} = \mathfrak{O}_6^{\mathsf{T}} + T(l-1)\mathfrak{O}_7^{\mathsf{T}}$. □

Theorem 3.5.8. *A COpNav environment with one fully-known receiver and one unknown SOP is observable,* $\forall\, l \geq 4$.

Proof. The state vector for this case is given by $\boldsymbol{x} = \left[\, \boldsymbol{x}_r^{\mathsf{T}}, \boldsymbol{x}_s^{\mathsf{T}} \,\right]^{\mathsf{T}}$. Full knowledge of the receiver is equivalent to having an observation Jacobian matrix of the form

$$\mathbf{H}(k) = \begin{bmatrix} \mathbf{h}_{b,r,s}^{\mathsf{T}}(k) & \mathbf{h}_{c,r,s}^{\mathsf{T}}(k) \\ \mathbf{I}_{6\times 6} & \mathbf{0} \end{bmatrix}. \tag{3.23}$$

Invoking (3.12)-(3.17), it can be be seen that the observability matrix $\mathfrak{O}_L(0,l)$ has a rank of 7 at the first time segment, since all the rows are linearly independent. The rank increments by one as each additional segment is appended up to $l = 4$. Adding a fourth time segment results in an observability matrix whose rank is 10 (full-rank). This can be shown by noting that the first 7 rows are linearly independent along with rows $8+7(l-2)$, for $l = 2, 3, 4$. Moreover, rows $i + 7(l-1)$ for $i = 4, 5, 7$ and $l = 1, 2, \ldots,$ are identical, respectively. Finally, $\mathfrak{O}_{9+7(l-2)}^{\mathsf{T}} = \mathfrak{O}_2^{\mathsf{T}} + T(l-1)\mathfrak{O}_4^{\mathsf{T}}$, $\mathfrak{O}_{10+7(l-2)}^{\mathsf{T}} = \mathfrak{O}_3^{\mathsf{T}} + T(l-1)\mathfrak{O}_5^{\mathsf{T}}$, and $\mathfrak{O}_{13+7(l-2)}^{\mathsf{T}} = \mathfrak{O}_6^{\mathsf{T}} + T(l-1)\mathfrak{O}_7^{\mathsf{T}}$, for $l = 2, 3, \ldots$ □

The results concluded from theorems 3.5.1–3.5.8 are summarized in Table 3.2, where observable states refer to those in an orthogonal complement to the unobservable subspace, and time-step l refers to the time-step at which the observability matrix rank reaches a steady-state value. It is worth noting that the observability results for the scenarios considered in Table 3.1 constitute the minimal set of observability requirements in the sense that knowing the results for these scenarios, one can predict the observability of an arbitrary scenario with n receivers and m SOPs and any type of prior knowledge (none, partial, or full) for the receivers and SOPs.

Table 3.2: Linear COpNav observability analysis results

Case	**Observable?**	**Observable States**	**Time-Step l**
1	no	none	5
2	no	$m = 1$: none	5
		$m \geq 2$: x_r, y_r, $\dot{x}_r$, $\dot{y}_r$	4
3	no	δt_r, $\dot{\delta} t_r$	5
4	yes	all	4
5	no	$\dot{x}_{r_i}$, $\dot{y}_{r_i}$, x_s, y_s, $\quad i = 1, \ldots, n$	3
6	no	$\dot{x}_{r_i}$, $\dot{y}_{r_i}$, $\quad i = 1, \ldots, n$	2
7	yes	all	2
8	yes	all	4

3.6 Nonlinear Observability Analysis

For nonlinear systems, it is more appropriate to analyze the observability through nonlinear observability tools rather than linearizing the nonlinear system and applying linear observability tools. This is due to two reasons: (i) nonlinear observability tools capture the nonlinearities of the dynamics and observations, and (ii) while the control inputs are never considered in the linear observability analysis, they are explicitly taken into account in the nonlinear observability analysis.

This section analyzes the observability of the scenarios outlined in Table 3.1 for receivers with controlled velocity random walk dynamics, i.e., $\boldsymbol{u} \neq 0$ in (2.2), through the nonlinear observability test discussed in Subsection 3.1.1 [85, 86].

3.6.1 Preliminary Facts

The following facts will be invoked in the nonlinear observability proofs corresponding to Table 3.1. First, when constructing $\mathfrak{O}_{\mathrm{NL}}$, one can stop calculating further derivatives of the output function at the first instance of linear dependence among the gradients, since after this point additional rows will not affect the rank of $\mathfrak{O}_{\mathrm{NL}}$. Second, the observable states in a COpNav environment, if any, can be found by computing the basis vectors spanning the null space of $\mathfrak{O}_{\mathrm{NL}}$, denoted $\mathcal{N}[\mathfrak{O}_{\mathrm{NL}}]$, and arranging the basis vectors into a matrix. The presence of a row of zeros in this matrix indicates that the corresponding state element is observable, since this state element is orthogonal to the unobservable subspace. Third, having prior knowledge about some of the COpNav environment states is equivalent to augmenting the observation vector with fictitious observations that are identical to these known states. For instance, an environment with a partially-known receiver and an unknown SOP can be associated with an observation vector $\boldsymbol{y} = [x_r, y_r, \rho]^{\mathsf{T}}$.

The remainder of this subsection discusses pertinent properties of the rows of $\mathfrak{O}_{\mathrm{NL}}$ in preparation for the nonlinear observability proofs that will follow. Consider an environment with one receiver making a pseudorange observation on one SOP. The vectors $\{\boldsymbol{f}_i\}_{i=0}^{r}$ corresponding to $\Sigma_{\mathrm{NL,a}}$ in (3.2) become $\boldsymbol{f}_0 = \dot{x}_r\boldsymbol{e}_1 + \dot{y}_r\boldsymbol{e}_2 + \dot{\delta}t_r\boldsymbol{e}_5 + \dot{\delta}t_s\boldsymbol{e}_9$, $\boldsymbol{f}_1 = \boldsymbol{e}_3$, and $\boldsymbol{f}_2 = \boldsymbol{e}_4$, where $\boldsymbol{e}_i$ is the standard basis vector consisting of a 1 in the ith element and zeros elsewhere. Consider the vector $\boldsymbol{h} = \left[x_r, y_r, \dot{x}_r, \dot{y}_r, \delta t_r, \dot{\delta}t_r, x_s, y_s, \delta t_s, \dot{\delta}t_s, \rho\right]^{\mathsf{T}}$.

It can be shown that the gradients of the zeroth-order Lie derivatives

of $\{h_l(\boldsymbol{x})\}_{l=1}^{11}$ with respect to $\boldsymbol{f}_i$ are given by

$$\nabla_{\boldsymbol{x}}^{\mathsf{T}}\left[\mathfrak{L}_{\boldsymbol{f}_i}^0 h_l(\boldsymbol{x})\right] = \begin{cases} g_1^0\cdot(\boldsymbol{e}_1^{\mathsf{T}}-\boldsymbol{e}_7^{\mathsf{T}}) + g_2^0\cdot(\boldsymbol{e}_2^{\mathsf{T}}-\boldsymbol{e}_8^{\mathsf{T}}) + c\cdot(\boldsymbol{e}_5^{\mathsf{T}}-\boldsymbol{e}_9^{\mathsf{T}}), & l=11; \\ \boldsymbol{e}_l^{\mathsf{T}}, & \text{otherwise;} \end{cases}$$

for $i=0,1,2$, where $g_1^0 \triangleq \frac{x_r-x_s}{\|\boldsymbol{r}_r-\boldsymbol{r}_s\|_2}$, $g_2^0 \triangleq \frac{y_r-y_s}{\|\boldsymbol{r}_r-\boldsymbol{r}_s\|_2}$.

The gradients of the first-order Lie derivatives are $\nabla_{\boldsymbol{x}}^{\mathsf{T}}\left[\mathfrak{L}_{\boldsymbol{f}_i}^1 h_l(\boldsymbol{x})\right] = \boldsymbol{0}$, for $i=1,2$ and $\forall l$; and

$$\nabla_{\boldsymbol{x}}^{\mathsf{T}}\left[\mathfrak{L}_{\boldsymbol{f}_0}^1 h_l(\boldsymbol{x})\right] = \begin{cases} \boldsymbol{e}_3^{\mathsf{T}}, & l=1; \\ \boldsymbol{e}_4^{\mathsf{T}}, & l=2; \\ \boldsymbol{e}_6^{\mathsf{T}}, & l=5; \\ \boldsymbol{e}_{10}^{\mathsf{T}}, & l=9; \\ g_1^1\cdot(\boldsymbol{e}_1^{\mathsf{T}}-\boldsymbol{e}_7^{\mathsf{T}}) + g_2^1\cdot(\boldsymbol{e}_2^{\mathsf{T}}-\boldsymbol{e}_8^{\mathsf{T}}) & \\ \quad + g_3^1\,\boldsymbol{e}_3^{\mathsf{T}} + g_4^1\,\boldsymbol{e}_4^{\mathsf{T}} + c\cdot(\boldsymbol{e}_6^{\mathsf{T}}-\boldsymbol{e}_{10}^{\mathsf{T}}), & l=11 \\ \boldsymbol{0}, & \text{otherwise;} \end{cases}$$

where $g_q^1 \triangleq \frac{\partial}{\partial\alpha}\left(\dot{x}_r\, g_1^0 + \dot{y}_r\, g_2^0\right)$, and $\alpha = x_r$ for $q=1$, $\alpha = y_r$ for $q=2$, $\alpha = \dot{x}_r$ for $q=3$, and $\alpha = \dot{y}_r$ for $q=4$.

The gradients of the second-order Lie derivatives are $\nabla_{\boldsymbol{x}}^{\mathsf{T}}\left[\mathfrak{L}_{\boldsymbol{f}_i}^2 h_l(\boldsymbol{x})\right] = \boldsymbol{0}$, for $i=1,2$ and $\forall l$; and

$$\nabla_{\boldsymbol{x}}^{\mathsf{T}}\left[\mathfrak{L}_{\boldsymbol{f}_0}^2 h_l(\boldsymbol{x})\right] = \begin{cases} g_1^2\cdot(\boldsymbol{e}_1^{\mathsf{T}}-\boldsymbol{e}_7^{\mathsf{T}}) + g_2^2\cdot(\boldsymbol{e}_2^{\mathsf{T}}-\boldsymbol{e}_8^{\mathsf{T}}) + g_3^2\,\boldsymbol{e}_3^{\mathsf{T}} + g_4^2\,\boldsymbol{e}_4^{\mathsf{T}}, & l=11; \\ \boldsymbol{0}, & \text{otherwise;} \end{cases}$$

where $g_q^2 \triangleq \frac{\partial}{\partial\alpha}\left(\dot{x}_r\, g_1^1 + \dot{y}_r\, g_2^1\right)$, and $\alpha = x_r$ for $q=1$, $\alpha = y_r$ for $q=2$, $\alpha = \dot{x}_r$ for $q=3$, and $\alpha = \dot{y}_r$ for $q=4$,

$$\nabla_{\boldsymbol{x}}^{\mathsf{T}}\left[\mathfrak{L}_{\boldsymbol{f}_0\boldsymbol{f}_i}^2 h_l(\boldsymbol{x})\right] = \begin{cases} g_\beta^2\cdot(\boldsymbol{e}_1^{\mathsf{T}}-\boldsymbol{e}_7^{\mathsf{T}}) + g_{\beta+1}^2\cdot(\boldsymbol{e}_2^{\mathsf{T}}-\boldsymbol{e}_8^{\mathsf{T}}), & l=11; \\ \boldsymbol{0}, & \text{otherwise;} \end{cases}$$

where $\beta=5$ if $i=1$ and $\beta=7$ if $i=2$; and $g_\beta^2 \triangleq \frac{\partial}{\partial x_r} g_{i+2}^1$ and $g_{\beta+1}^2 \triangleq \frac{\partial}{\partial y_r} g_{i+2}^1$.

3.6.2 Nonlinear Observability Results

Theorem 3.6.1. *A COpNav environment with one unknown receiver, without controlled maneuvers, and one unknown SOP has no observable states. Allowing controlled maneuvers makes the receiver velocity states observable.*

Proof. The observation vector is $\boldsymbol{y} = [\,\rho\,]$ and $\boldsymbol{x} \in \mathbb{R}^{10}$. Without control, the only linearly independent rows are $\left\{\nabla_{\boldsymbol{x}}^{\mathsf{T}}\left[\mathfrak{L}_{\boldsymbol{f}_0}^{p} h(\boldsymbol{x})\right], p = 0, \ldots, 4\right\}$; hence, $\operatorname{rank}[\mathfrak{O}_{\mathrm{NL}}] = 5$, and

$$\mathcal{N}[\mathfrak{O}_{\mathrm{NL}}] = \operatorname{span}\{\boldsymbol{n}_1, \boldsymbol{n}_2, \boldsymbol{n}_3, \boldsymbol{n}_4, \boldsymbol{n}_5\},$$

where $\boldsymbol{n}_1 \triangleq \boldsymbol{e}_1 + \boldsymbol{e}_7$, $\boldsymbol{n}_2 \triangleq \boldsymbol{e}_2 + \boldsymbol{e}_8$, $\boldsymbol{n}_3 \triangleq \boldsymbol{e}_5 + \boldsymbol{e}_9$, $\boldsymbol{n}_4 \triangleq \boldsymbol{e}_6 + \boldsymbol{e}_{10}$, $\boldsymbol{n}_5 \triangleq \sum_{i=1}^{4} \gamma_i \boldsymbol{e}_i$, and $\gamma_1 \triangleq \frac{-y_r + y_s}{\dot{x}_r}$, $\gamma_2 \triangleq \frac{x_r - x_s}{\dot{x}_r}$, $\gamma_3 \triangleq \frac{-\dot{y}_r}{\dot{x}_r}$, $\gamma_4 \triangleq 1$.

Allowing controlled maneuvers introduces an additional linearly independent row: $\left\{\nabla_{\boldsymbol{x}}^{\mathsf{T}}\left[\mathfrak{L}_{\boldsymbol{f}_0 \boldsymbol{f}_i}^{2} h(\boldsymbol{x})\right], i = 1 \text{ or } 2\right\}$, yielding $\operatorname{rank}[\mathfrak{O}_{\mathrm{NL}}] = 6$ and removing $\boldsymbol{n}_5$ from $\mathcal{N}[\mathfrak{O}_{\mathrm{NL}}]$. □

Theorem 3.6.2. *A COpNav environment with one unknown receiver, without controlled maneuvers, and m partially-known SOPs has no observable states for $m = 1$. The receiver position and velocity states become observable for $m \geq 2$. Allowing controlled maneuvers makes the receiver position and velocity states observable $\forall\, m \geq 1$.*

Proof. The observation vector is $\boldsymbol{y} = [\,\boldsymbol{r}_{s_1}, \ldots, \boldsymbol{r}_{s_m},\ \ \rho_{s_1}, \ldots, \rho_{s_m}\,]$ and $\boldsymbol{x} \in \mathbb{R}^{6+4m}$. Without control, and for $m = 1$, the only linearly independent

rows are $\left\{\nabla_{\boldsymbol{x}}^{\mathsf{T}}\left[\mathfrak{L}_{\boldsymbol{f}_0}^0 h_l(\boldsymbol{x})\right], l=1,\ldots,3; \nabla_{\boldsymbol{x}}^{\mathsf{T}}\left[\mathfrak{L}_{\boldsymbol{f}_0}^p h_3(\boldsymbol{x})\right], p=1,\ldots,4\right\}$; hence, $\operatorname{rank}[\mathfrak{O}_{\mathrm{NL}}]=7$, and

$$\mathcal{N}[\mathfrak{O}_{\mathrm{NL}}]=\operatorname{span}\{\boldsymbol{n}_3,\,\boldsymbol{n}_4,\,\boldsymbol{n}_5\}.$$

For $m\geq 2$, the only linearly independent rows are $\left\{\nabla_{\boldsymbol{x}}^{\mathsf{T}}\left[\mathfrak{L}_{\boldsymbol{f}_0}^0 h_l(\boldsymbol{x})\right], l=1,\ldots,3m; \nabla_{\boldsymbol{x}}^{\mathsf{T}}\left[\mathfrak{L}_{\boldsymbol{f}_0}^1 h_l(\boldsymbol{x})\right], l=2m+1,\ldots 3m\right\}$, with the following additional linearly independent rows:

- $m=2$: $\left\{\nabla_{\boldsymbol{x}}^{\mathsf{T}}\left[\mathfrak{L}_{\boldsymbol{f}_0}^p h_l(\boldsymbol{x})\right], p=2,3, l=5,6\right\}$
- $m=3$: $\left\{\nabla_{\boldsymbol{x}}^{\mathsf{T}}\left[\mathfrak{L}_{\boldsymbol{f}_0}^2 h_l(\boldsymbol{x})\right], l=7,8,9; \nabla_{\boldsymbol{x}}^{\mathsf{T}}\left[\mathfrak{L}_{\boldsymbol{f}_0}^3 h_7(\boldsymbol{x})\right]\right\}$,
- $m\geq 4$: $\left\{\nabla_{\boldsymbol{x}}^{\mathsf{T}}\left[\mathfrak{L}_{\boldsymbol{f}_0}^2 h_l(\boldsymbol{x})\right], l=3m-4,\ldots,3m\right\}$.

Hence, $\operatorname{rank}[\mathfrak{O}_{\mathrm{NL}}]=4m+4$, and

$$\mathcal{N}[\mathfrak{O}_{\mathrm{NL}}]=\operatorname{span}\{\boldsymbol{n}_6,\boldsymbol{n}_7\},$$

where $\boldsymbol{n}_6\triangleq\boldsymbol{e}_5+\sum_{i=1}^m\boldsymbol{e}_{5+4i}$ and $\boldsymbol{n}_7\triangleq\boldsymbol{e}_7+\sum_{i=1}^m\boldsymbol{e}_{6+4i}$.

Allowing controlled maneuvers, for $m\geq 1$, introduces an additional linearly independent row: $\left\{\nabla_{\boldsymbol{x}}^{\mathsf{T}}\left[\mathfrak{L}_{\boldsymbol{f}_0\boldsymbol{f}_i}^2 h_{2m+1}(\boldsymbol{x})\right], i=1 \text{ or } 2\right\}$, yielding $\operatorname{rank}[\mathfrak{O}_{\mathrm{NL}}]=4m+4$, and

$$\mathcal{N}[\mathfrak{O}_{\mathrm{NL}}]=\operatorname{span}\{\boldsymbol{n}_6,\,\boldsymbol{n}_7\}.$$

□

Theorem 3.6.3. *A COpNav environment with one unknown receiver, without controlled maneuvers, and one fully-known SOP only has observable the receiver clock bias and drift states. Allowing controlled maneuvers makes all the states observable.*

Proof. The observation vector is $\boldsymbol{y} = [\,\boldsymbol{x}_s, \rho\,]$ and $\boldsymbol{x} \in \mathbb{R}^{10}$. Without control, the only linearly independent rows are $\left\{\nabla_{\boldsymbol{x}}^{\mathsf{T}}\left[\mathfrak{L}_{\boldsymbol{f}_0}^{0} h_l(\boldsymbol{x})\right], l = 1,\ldots,5;\ \nabla_{\boldsymbol{x}}^{\mathsf{T}}\left[\mathfrak{L}_{\boldsymbol{f}_0}^{p} h_5(\boldsymbol{x})\right], p = 1,\ldots,4\right\}$; hence, $\operatorname{rank}[\mathfrak{O}_{\mathrm{NL}}] = 9$, and

$$\mathcal{N}[\mathfrak{O}_{\mathrm{NL}}] = \operatorname{span}\{\boldsymbol{n}_5\}.$$

Allowing controlled maneuvers introduces an additional linearly independent row: $\left\{\nabla_{\boldsymbol{x}}^{\mathsf{T}}\left[\mathfrak{L}_{\boldsymbol{f}_0\boldsymbol{f}_i}^{2} h_5(\boldsymbol{x})\right], i = 1 \text{ or } 2\right\}$, yielding $\operatorname{rank}[\mathfrak{O}_{\mathrm{NL}}] = 10$. □

Theorem 3.6.4. *A COpNav environment with one unknown receiver, without controlled maneuvers, one fully-known SOP, and one partially-known SOP is fully-observable. Allowing controlled maneuvers does not affect observability.*

Proof. The observation vector is $\boldsymbol{y} = [\,\boldsymbol{x}_{s_1}, \boldsymbol{r}_{s_2}, \rho_{s_1}, \rho_{s_2}\,]$ and $\boldsymbol{x} \in \mathbb{R}^{14}$. Without control, the only linearly independent rows are $\left\{\nabla_{\boldsymbol{x}}^{\mathsf{T}}\left[\mathfrak{L}_{\boldsymbol{f}_0}^{0} h_l(\boldsymbol{x})\right], l = 1,\ldots,8;\ \nabla_{\boldsymbol{x}}^{\mathsf{T}}\left[\mathfrak{L}_{\boldsymbol{f}_0}^{p} h_l(\boldsymbol{x})\right], p = 1,\ldots,3,\ l = 7,8\right\}$, and $\operatorname{rank}[\mathfrak{O}_{\mathrm{NL}}] = 14$. Allowing controlled maneuvers does not add linearly independent rows. □

Theorem 3.6.5. *A COpNav environment with n partially-known receivers, without controlled maneuvers, and one unknown SOP only has observable the receivers' velocity states and the SOP's position states. Allowing controlled maneuvers does not affect observability.*

Proof. The observation vector is $\boldsymbol{y} = [\,\boldsymbol{r}_{r_1}, \ldots, \boldsymbol{r}_{r_n}, \rho_{r_1}, \ldots, \rho_{r_n}\,]$ and $\boldsymbol{x} \in \mathbb{R}^{6n+4}$. Without control, the only linearly independent rows are $\left\{\nabla_{\boldsymbol{x}}^{\mathsf{T}}\left[\mathfrak{L}_{\boldsymbol{f}_0}^{p} h_l(\boldsymbol{x})\right], p = 0,1, l = 1,\ldots,3n\right\}$, with the following additional linearly independent rows:

- $n = 1$: $\left\{\nabla_{\boldsymbol{x}}^{\mathsf{T}}\left[\mathfrak{L}_{\boldsymbol{f}_0}^{p} h_3(\boldsymbol{x})\right], p = 2, 3\right\}$,
- $n \geq 2$: $\left\{\nabla_{\boldsymbol{x}}^{\mathsf{T}}\left[\mathfrak{L}_{\boldsymbol{f}_0}^{2} h_l(\boldsymbol{x})\right], l = 2n+1, 2n+2\right\}$.

Hence, $\operatorname{rank}[\mathfrak{O}_{\mathrm{NL}}] = 6n + 2$, and

$$\mathcal{N}[\mathfrak{O}_{\mathrm{NL}}] = \operatorname{span}\left\{\boldsymbol{e}_5 + \sum_{i=1}^{n} \boldsymbol{e}_{5+6i},\ \boldsymbol{e}_6 + \sum_{i=1}^{n} \boldsymbol{e}_{6+6i}\right\}.$$

Allowing controlled maneuvers does not improve the rank any further, since the control inputs will introduce additional rows into $\mathfrak{O}_{\mathrm{NL}}$ whose columns are linearly independent according to: $\mathfrak{O}_{6n+3} = -\sum_{i=0}^{n-1} \mathfrak{O}_{5+6i}$ and $\mathfrak{O}_{6n+4} = -\sum_{i=0}^{n-1} \mathfrak{O}_{6+6i}$, where $\mathfrak{O}_i$ corresponds to the ith column of $\mathfrak{O}_{\mathrm{NL}}$. □

Theorem 3.6.6. *A COpNav environment with n partially-known receivers, without controlled maneuvers, and m partially-known SOPs only has observable the receivers' velocity states. Allowing controlled maneuvers does not affect observability.*

Proof. The observation vector is $\boldsymbol{y} = [\boldsymbol{r}_{r_1}, \ldots, \boldsymbol{r}_{r_n}, \boldsymbol{r}_{s_1}, \ldots, \boldsymbol{r}_{s_m}, \rho_{r_1,s_1}, \ldots, \rho_{r_n,s_m}]$ and $\boldsymbol{x} \in \mathbb{R}^{6n+4m}$. Without control, the only linearly independent rows are $\left\{\nabla_{\boldsymbol{x}}^{\mathsf{T}}\left[\mathfrak{L}_{\boldsymbol{f}_0}^{0} h_l(\boldsymbol{x})\right], l = 1, \ldots, 2n+2m+nm; \nabla_{\boldsymbol{x}}^{\mathsf{T}}\left[\mathfrak{L}_{\boldsymbol{f}_0}^{1} h_l(\boldsymbol{x})\right], l = 2m+1, \ldots, 4n+4m-nm-2\right\}$; hence, $\operatorname{rank}[\mathfrak{O}_{\mathrm{NL}}] = 6n + 4m - 2$, and

$$\begin{aligned}\mathcal{N}[\mathfrak{O}_{\mathrm{NL}}] \;=\; \operatorname{span}\Bigg\{ & \boldsymbol{e}_{6n+4m-1} + \sum_{l=1}^{n} \boldsymbol{e}_{6l-1} + \sum_{l=0}^{m-2} \boldsymbol{e}_{6n+4l+3}, \\ & \boldsymbol{e}_{6n+4m} + \sum_{l=1}^{n} \boldsymbol{e}_{6l} + \sum_{l=0}^{m-2} \boldsymbol{e}_{6n+4l+4} \Bigg\},\end{aligned}$$

Allowing controlled maneuvers does not improve the rank any further, since the control inputs will introduce additional rows into $\mathfrak{O}_{\text{NL}}$ whose columns are linearly independent according to: $\mathfrak{O}_{6n+4m-1} = -\left[\sum_{l=1}^{n} \mathfrak{O}_{6l-1} + \sum_{l=0}^{m-2} \mathfrak{O}_{6n+4l+3}\right]$ and $\mathfrak{O}_{6n+4m} = -\left[\sum_{l=1}^{n} \mathfrak{O}_{6l} + \sum_{l=0}^{m-2} \mathfrak{O}_{6n+4l+4}\right]$. □

Theorem 3.6.7. *A COpNav environment with one partially-known receiver, without controlled maneuvers, and one fully-known SOP is fully-observable. Allowing controlled maneuvers does not affect observability.*

Proof. The observation vector is $\boldsymbol{y} = [\,\boldsymbol{r}_r, \boldsymbol{x}_s, \rho\,]$ and $\boldsymbol{x} \in \mathbb{R}^{10}$. Without control, the only linearly independent rows are $\left\{\nabla_{\boldsymbol{x}}^{\mathsf{T}}\left[\mathfrak{L}_{\boldsymbol{f}_0}^{0} h_l(\boldsymbol{x})\right], l = 1,\ldots,7;\ \nabla_{\boldsymbol{x}}^{\mathsf{T}}\left[\mathfrak{L}_{\boldsymbol{f}_0}^{1} h_l(\boldsymbol{x})\right], l = 1,2,7\right\}$ and $\operatorname{rank}[\mathfrak{O}_{\text{NL}}] = 10$, i.e., full-rank. □

Theorem 3.6.8. *A COpNav environment with one fully-known receiver, without controlled maneuvers, and one unknown SOP is fully-observable. Allowing controlled maneuvers does not affect observability.*

Proof. The observation vector is $\boldsymbol{y} = [\,\boldsymbol{x}_r, \rho\,]$ and $\boldsymbol{x} \in \mathbb{R}^{10}$. Without control, the only linearly independent rows are $\left\{\nabla_{\boldsymbol{x}}^{\mathsf{T}}\left[\mathfrak{L}_{\boldsymbol{f}_0}^{0} h_l(\boldsymbol{x})\right], l = 1,\ldots,7;\ \nabla_{\boldsymbol{x}}^{\mathsf{T}}\left[\mathfrak{L}_{\boldsymbol{f}_0}^{1} h_l(\boldsymbol{x})\right], l = 1,2,7\right\}$ and $\operatorname{rank}[\mathfrak{O}_{\text{NL}}] = 10$, i.e., full-rank. □

Table 3.3 summarizes the nonlinear observability results. The following conclusions can be drawn from these results. (i) The observability results achieved from the linear observability analysis in 3.5 for receivers with velocity random walk dynamics were identical to the ones achieved through the more

rigorous nonlinear observability tools for receivers with uncontrolled maneuvers. (*ii*) Allowing receiver-controlled maneuvers reduces the required *a priori* knowledge about the environment for observability. (*iii*) The control inputs are necessary to make Case 3 fully-observable, since the Lie derivative contributions of $\boldsymbol{f}_1$ or $\boldsymbol{f}_2$ are needed to make $\mathfrak{O}_{\text{NL}}$ full-rank. While the inputs corresponding to $\boldsymbol{f}_1$ or $\boldsymbol{f}_2$ can be specified in infinitely many ways, the only requirement is that such inputs be non-zero.

Table 3.3: Nonlinear COpNav observability analysis results: Observable states

Case	**Without Control**	**With Control**
1	none	$\dot{x}_r$, $\dot{y}_r$
2	$m = 1$: none $m \geq 2$: x_r, y_r, $\dot{x}_r$, $\dot{y}_r$	$m \geq 1$: x_r, y_r, $\dot{x}_r$, $\dot{y}_r$
3	δt_r, $\dot{\delta t}_r$	all
4	all	all
5	$\dot{x}_{r_i}$, $\dot{y}_{r_i}$, x_s, y_s, $\quad i = 1, \ldots, n$	$\dot{x}_{r_i}$, $\dot{y}_{r_i}$, x_s, y_s, $\quad i = 1, \ldots, n$
6	$\dot{x}_{r_i}$, $\dot{y}_{r_i}$, $\quad i = 1, \ldots, n$	$\dot{x}_{r_i}$, $\dot{y}_{r_i}$, $\quad i = 1, \ldots, n$
7	all	all
8	all	all

The following main result can be concluded from the observability analysis conducted in Sections 3.5 and 3.6.

Theorem 3.6.9. *A planar COpNav environment comprising multiple receivers with velocity random walk dynamics making pseudorange observations on multiple terrestrial SOPs is fully-observable if and only if the initial states of at least: (i) one receiver is fully-known, (ii) one receiver is partially-known and one SOP is fully-known, or (iii) one SOP is fully-known and one SOP is*

partially-known. If the receivers control their maneuvers in the form of acceleration commands, the environment is fully-observable if and only if the initial states of at least: (i) one receiver is fully-known or (ii) one SOP is fully-known.

3.7 Simulation Results

This section presents simulation results for the three observable cases corresponding to receivers with uncontrolled maneuvers in Table 3.2: Cases 4, 7, and 8 [84, 87]. For purposes of numerical stability, the clock error states were defined to be $c\delta t$ and $c\dot{\delta t}$, where c is the speed of light. The receiver's clock was assumed to be a temperature-compensated crystal oscillator (TCXO), while the SOPs' clocks were assumed to be oven-controlled crystal oscillators (OCXOs). A simulator was developed to generate the "truth" data for each COpNav environment studied. The simulation settings are specified in Table 3.4.

Table 3.4: Observability & estimability analyses simulation settings

Parameter	**Value**
$\boldsymbol{x}_r(0)$	$[\,0,\,0,\,0,\,25,\,10,\,1\,]^\mathsf{T}$
$\boldsymbol{x}_{s_1}(0)$	$[\,50,\,100,\,1,\,0.1\,]^\mathsf{T}$
$\boldsymbol{x}_{s_2}(0)$	$[\,-50,\,100,\,1,\,0.1\,]^\mathsf{T}$
$\{h_{0,r},\, h_{-2,r}\}$	$\{\,2\times10^{-19},\,2\times10^{-20}\,\}$
$\{h_{0,s_i},\, h_{-2,s_i}\}$	$\{\,8\times10^{-20},\,4\times10^{-23}\,\}, \quad i=1,2$
$\tilde{q}_x, \tilde{q}_y$	$0.1\,(\mathrm{m/s^2})^2$
r	$100\,\mathrm{m}^2$
T	$0.01\,\mathrm{s}$

The noisy pseudorange observations were processed by an EKF to estimate the states of interest. In the following simulations, the system true initial state $\boldsymbol{x}(0)$ was fixed, while the EKF initial state estimate $\hat{\boldsymbol{x}}(0)$ was generated according to $\hat{\boldsymbol{x}}(0) \sim \mathcal{N}[\boldsymbol{x}(0), \mathbf{P}(0|-1)]$, where $\mathbf{P}(0|-1)$ is the EKF initial estimation error covariance. The observability is quantified in terms of the estimation error $\tilde{\boldsymbol{x}} \triangleq \boldsymbol{x} - \hat{\boldsymbol{x}}$ and the corresponding estimation error covariance $\mathbf{P} \triangleq \mathbb{E}\left[\tilde{\boldsymbol{x}}\,\tilde{\boldsymbol{x}}^{\mathsf{T}}\right]$, where $\hat{\boldsymbol{x}}$ is the EKF state estimate. Results for a single-run EKF and rigorous Monte Carlo (MC) analysis are presented. The MC analysis is based on an N-run average of the normalized estimation error squared (NEES) [58]. The ith-run NEES ϵ_i and the average NEES $\bar{\epsilon}$ are defined as

$$\epsilon_i(k) \triangleq \tilde{\boldsymbol{x}}_i^{\mathsf{T}}(k|k)\mathbf{P}_i^{-1}(k|k)\tilde{\boldsymbol{x}}_i(k|k), \quad \bar{\epsilon}(k) \triangleq \frac{1}{N}\sum_{i=1}^{N}\epsilon_i(k).$$

For the single-run EKF, an observable system should yield converging estimation error covariances and the estimation errors should remain bounded. For the N-run EKF, an observable system and a consistent EKF should yield a statistic $N\bar{\epsilon}(k)$ that is approximately chi-squared distributed with Nn degrees of freedom, specifically $N\bar{\epsilon}(k) \sim \chi^2_{Nn}$, where n is the state estimate dimension. An unobservable system should yield an estimation error covariance that never improves with more observations. Thus, the MC analysis boils down to a hypothesis test on $\bar{\epsilon}(k)$ with an acceptance region $[r_1, r_2]$ defined such that $\Pr\{\bar{\epsilon}(k) \in [r_1, r_2] \,|\, H_0\} = 1 - \alpha$, where H_0 is the null hypothesis and α is the size of the test (probability of false alarm).

The simulations for Case 4 considered an environment with an unknown

receiver and two SOPs: one fully-known and one partially-known. The initial estimation error covariance matrices of the receiver and the second SOP were chosen to be $\mathbf{P}_r(0|-1) = (1 \times 10^3)\,\mathrm{diag}\,[\,2, 2, 1, 1, 30, 0.3\,]$ and $\mathbf{P}_{s_2}(0|-1) = (1 \times 10^3)\,\mathrm{diag}\,[\,30, 0.3\,]$, respectively.

The simulations for Case 7 considered an environment with a partially-known receiver and two SOPs: one fully-known and one unknown. The initial estimation error covariance matrices of the receiver and the second SOP were chosen to be $\mathbf{P}_r(0|-1) = (1 \times 10^3)\,\mathrm{diag}\,[\,1, 1, 30, 0.3\,]$ and $\mathbf{P}_{s_2}(0|-1) = (1 \times 10^3)\,\mathrm{diag}\,[\,1, 1, 30, 0.3\,]$, respectively.

The simulations for Case 8 considered an environment with a fully-known receiver and one unknown SOP. The initial estimation error covariance matrix of the SOP was chosen to be $\mathbf{P}_{s_1}(0|-1) = (1 \times 10^3)\mathrm{diag}\,[\,1, 1, 30, 0.3\,]$.

Figures 3.3, 3.4, and 3.5 show the estimation error trajectories $\tilde{x}_i(k|k)$ for a single-run EKF along with the $\pm 2\sigma_i(k|k)$ estimation error variance bounds for Cases 4, 7, and 8, respectively. Note that the estimation error variances converge and that the estimation errors remain bounded, as would be expected for an observable system.

Figures 3.6, 3.7, and 3.8 show the resulting NEES trajectories $\bar{\epsilon}(k)$ for $\alpha = 0.01$ along with r_1 and r_2 for Cases 4, 7, and 8, respectively. Note that the $\bar{\epsilon}(k)$ values reside within the 99% probability region, which is consistent with a well-behaved estimator operating on an observable system.

The eigenvalues associated with the normalized estimation error co-

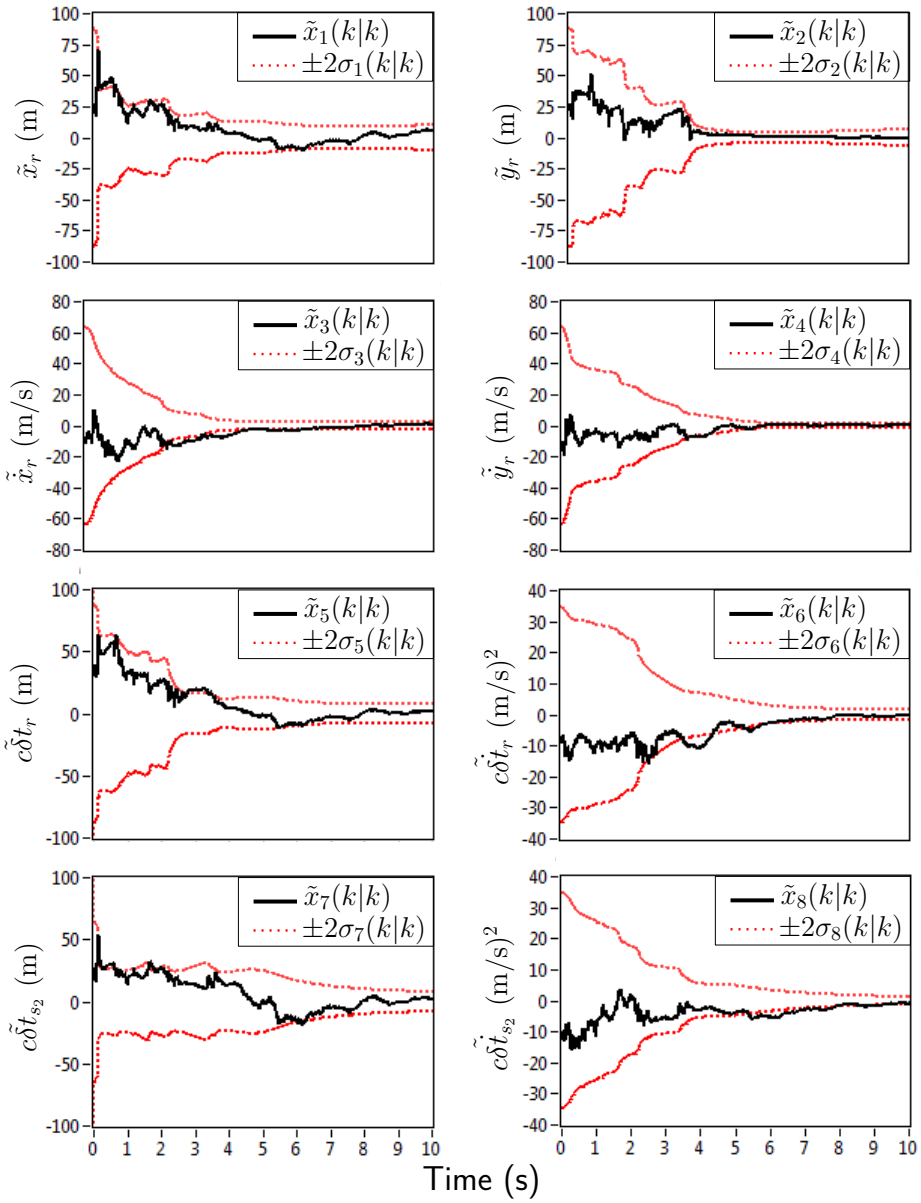

Figure 3.3: Estimation error trajectories and $\pm 2\sigma$-bounds for Case 4 in Table 3.1

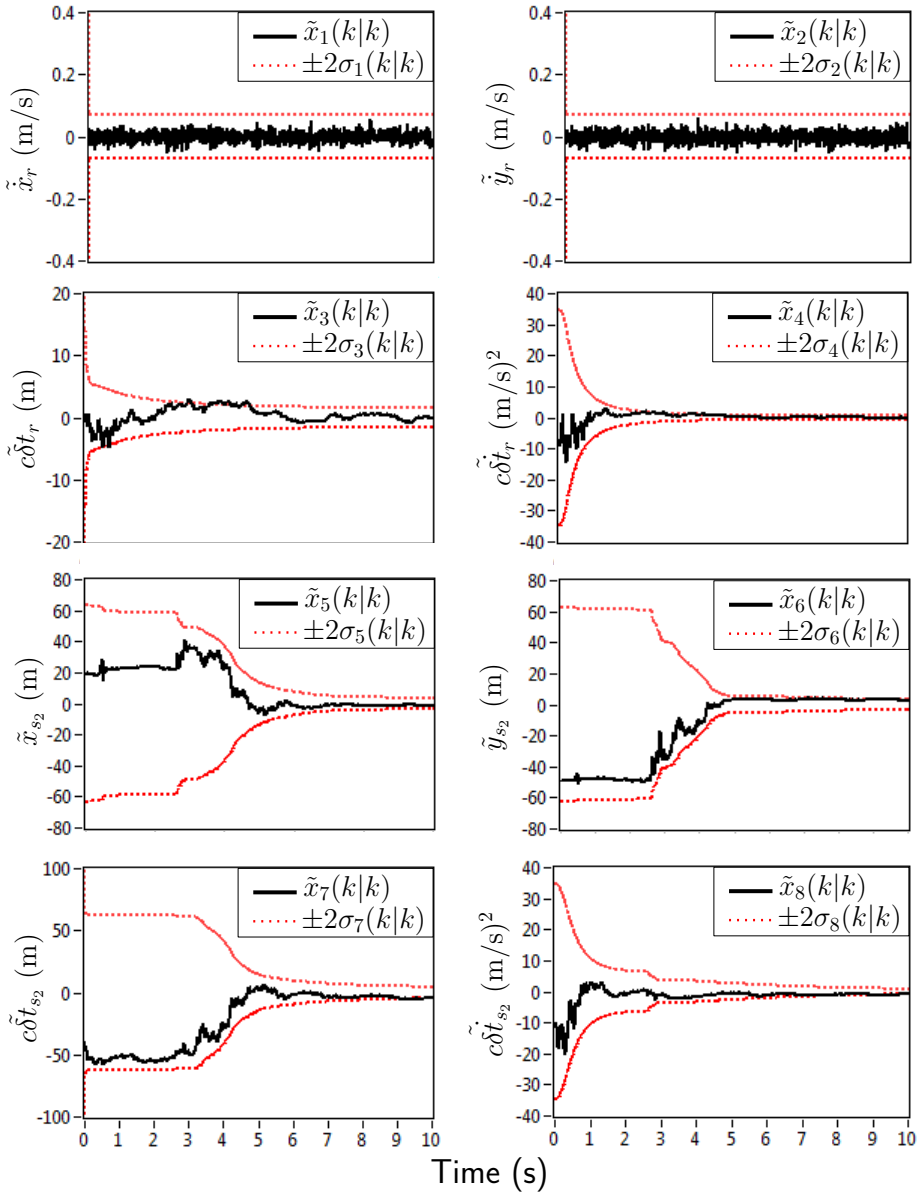

Figure 3.4: Estimation error trajectories and $\pm 2\sigma$-bounds for Case 7 in Table 3.1

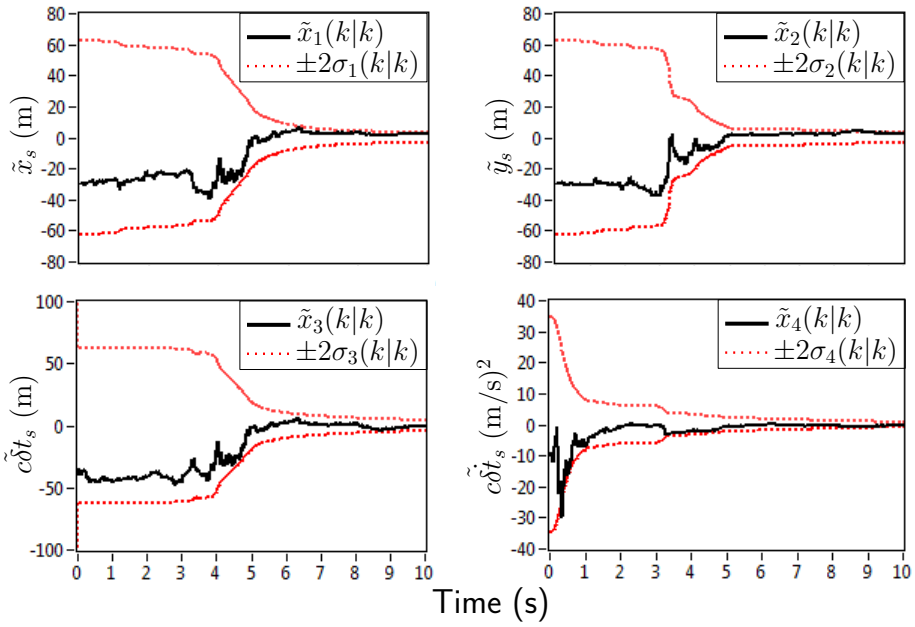

Figure 3.5: Estimation error trajectories and $\pm 2\sigma$-bounds for Case 8 in Table 3.1

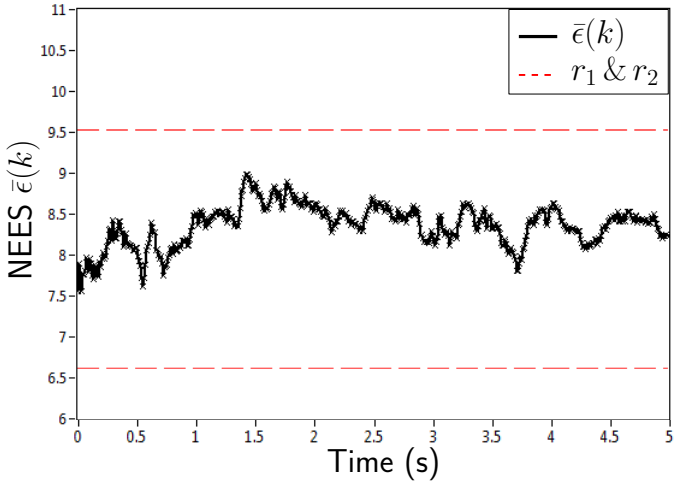

Figure 3.6: NEES and r_1 & r_2 bounds for Case 4 in Table 3.1 with 50 MC runs

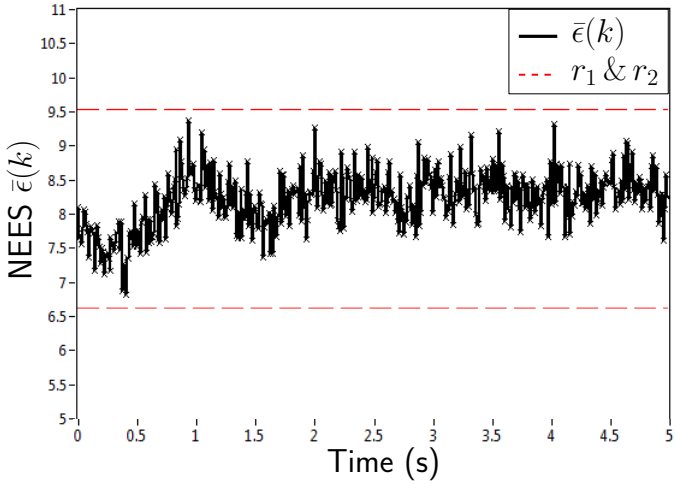

Figure 3.7: NEES and r_1 & r_2 bounds for Case 7 in Table 3.1 with 50 MC runs

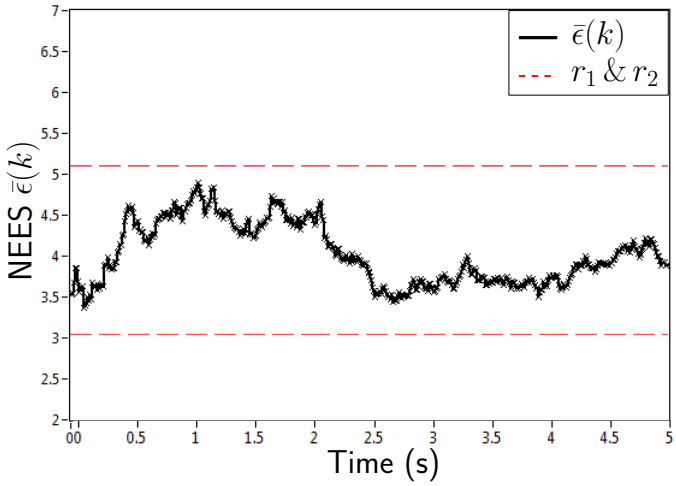

Figure 3.8: NEES and r_1 & r_2 bounds for Case 8 in Table 3.1 with 50 MC runs

variance, defined in (3.11), in ascending order corresponding to the single-run simulation results for Cases 4, 7, and 8 at the end of the simulation are given in Table 3.5. It is noted that in all three cases there is a wide dispersion between the smallest and largest eigenvalues, indicating the existence of modes with exceptionally good and exceptionally poor observability. To determine the directions associated with the modes with good and poor observability, the eigenvectors corresponding to the smallest and largest eigenvalues, respectively, are calculated and plotted in Figures 3.9, 3.10, and 3.11.

Table 3.5: Eigenvalues of normalized estimation error covariance matrix for COpNav observable scenarios

Case	**Eigenvalues**
4	0.002, 0.008, 0.057, 0.065, 0.072, 0.169, 2.272, 5.355
7	0.003, 0.003, 0.005, 0.011, 0.094, 0.428, 2.626, 4.830
8	0.002, 0.026, 1.491, 2.481

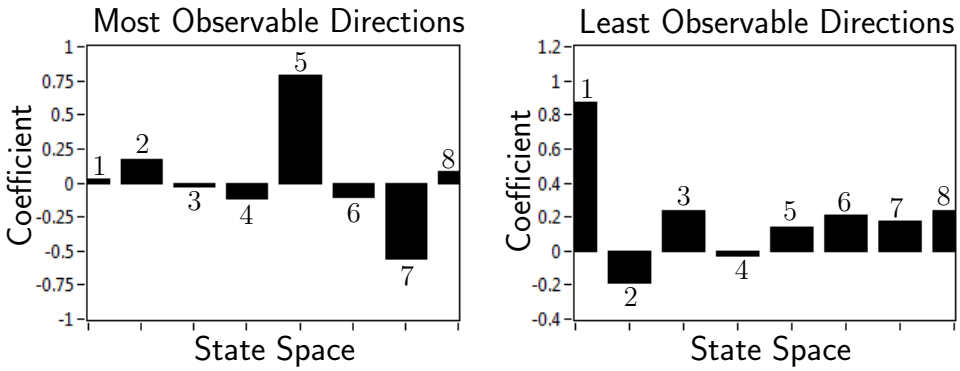

Figure 3.9: Eigenvector along the most and least observable directions in the state space for Case 4 in Table 3.1

From Figure 3.9 it can be concluded that a linear combination of the

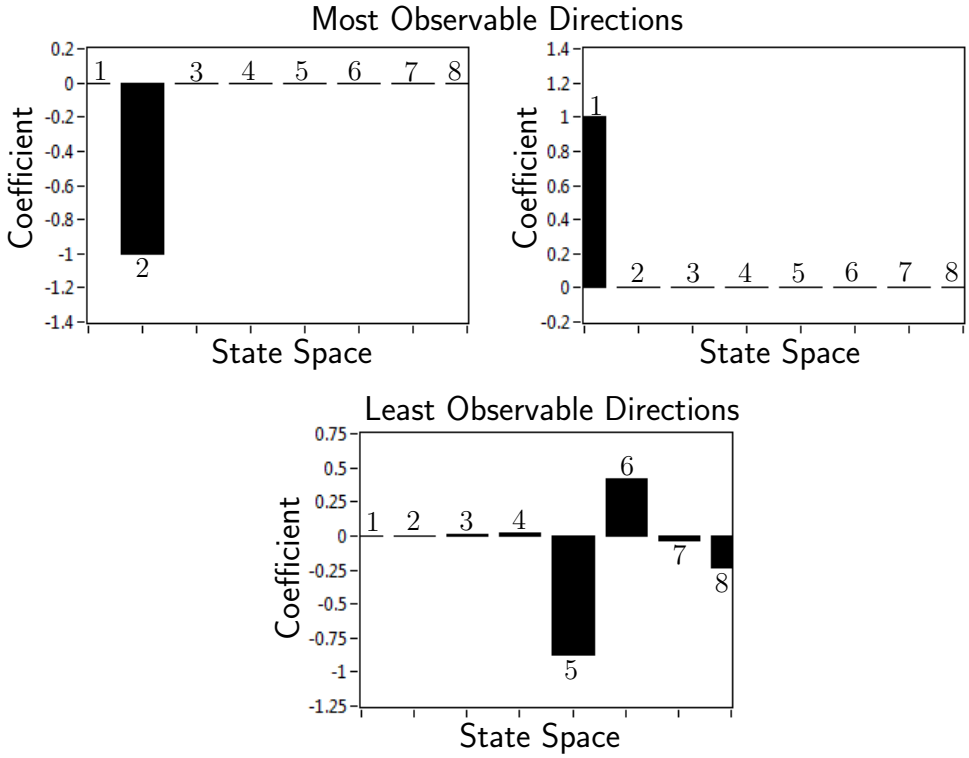

Figure 3.10: Eigenvector along the most and least observable directions in the state space for Case 7 in Table 3.1

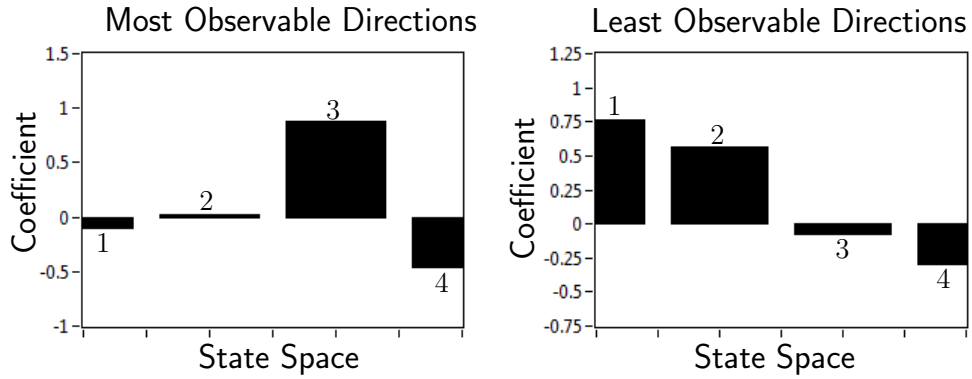

Figure 3.11: Eigenvector along the most and least observable directions in the state space for Case 8 in Table 3.1

fifth and seventh states, corresponding to δt_r and δt_{s_2}, can be estimated exceptionally well with respect to the rest of the states, whereas the first state, corresponding to x_r, is poorly observable. From Figure 3.10 it can be concluded that the first and second states, corresponding to $\dot{x}_r$ and $\dot{y}_r$, can be estimated exceptionally well with respect to the rest of the states, whereas a linear combination of the fifth and sixth states, corresponding to x_{s_2} and y_{s_2}, are poorly observable. From Figure 3.11 it can be concluded that the third state, corresponding to δt_s, can be estimated exceptionally well with respect to the rest of the states, whereas a linear combination of the first and second states, corresponding to x_s and y_s, are poorly observable.

3.8 Experimental Results

A field experimental demonstration was conducted to illustrate one of the observable cases in Table 3.1, namely Case 8 [84]. The objective was to demonstrate that a COpNav receiver with velocity random walk dynamics and knowledge of its initial state can estimate the states of an unknown SOP in its environment. To this end, two antennas were mounted on a vehicle to acquire and track: (i) multiple GPS signals and (ii) a signal from a nearby cellular phone tower whose signal was modulated through code division multiple access (CDMA). The GPS and cellular signals were simultaneously downmixed and synchronously sampled via two National Instruments® vector Radio Frequency Signal Analyzers (RFSAs). These front-ends fed their data to a Generalized Radionavigation Interfusion Device (GRID) software receiver [88], which si-

multaneously tracked all GPS L1 C/A signals in view and the signal from the cellular tower with unknown states, producing pseudorange observables for all tracked signals. The observables were fed into a MATLAB®-based EKF, which estimated the states of the unknown CDMA cellular tower. Figure 3.12 illustrates the hardware setup of the conducted experiment.

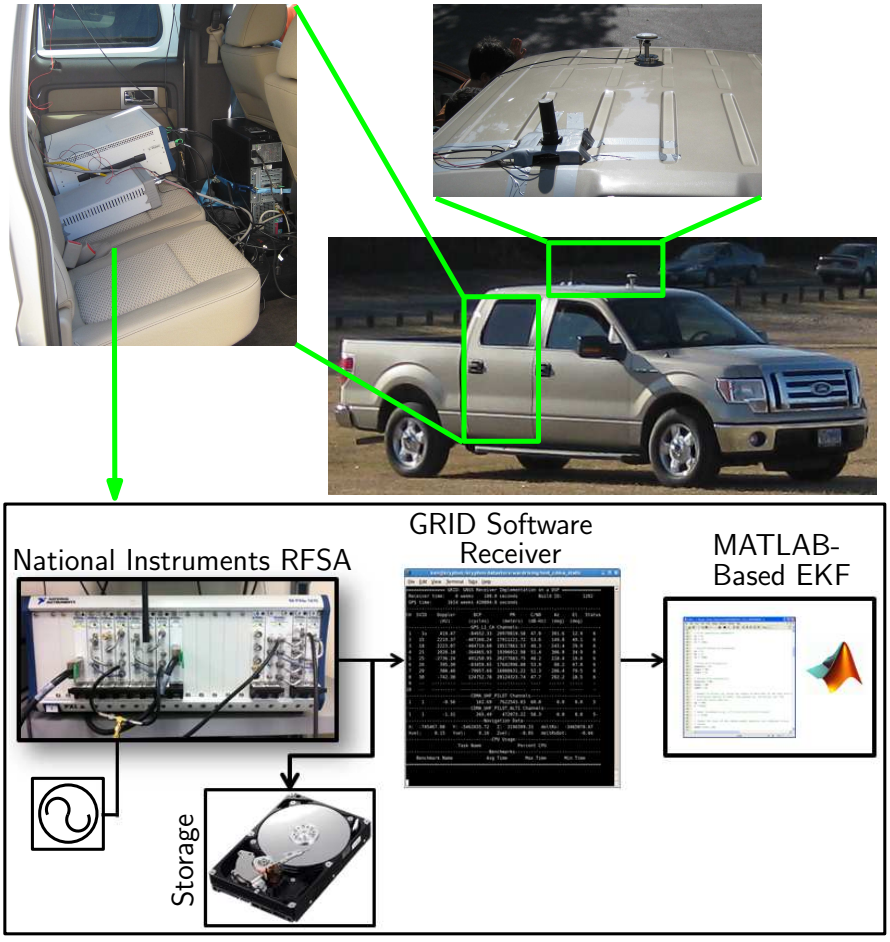

Figure 3.12: Experiment hardware setup

Since the states of the GPS satellite vehicles (SVs) were known, and

since the receiver was tracking more than four GPS SVs throughout the experiment, the receiver's initial state $\boldsymbol{x}_r(0)$ was fully-known. The cellular tower state vector consisted of its planar position states, clock bias, and clock drift, as defined in (2.3). The EKF initial state estimate $\hat{\boldsymbol{x}}(0)$ was generated according to $\hat{\boldsymbol{x}}(0) \sim \mathcal{N}[\,\boldsymbol{x}(0), \mathbf{P}(0|-1)\,]$, where $\boldsymbol{x}(0) \triangleq \left[\,\boldsymbol{r}_s^{\mathsf{T}}(0), c\delta t_s(0), 0\,\right]^{\mathsf{T}}$, where $\boldsymbol{r}_s^{\mathsf{T}} \triangleq [\,x_s(0), y_s(0)\,]$ is the projection of the true cellular tower location from the Earth-Centered Earth-Fixed (ECEF) coordinate frame system to a planar system, $c\delta t_s(0) = \|\boldsymbol{r}_r(0) - \hat{\boldsymbol{r}}_s(0|-1)\|_2 - \rho(0) + c\delta t_r(0)$, $\boldsymbol{r}_r^{\mathsf{T}}(0) \triangleq [\,x_r(0), y_r(0)\,]$ is the planar projection of the receiver's initial location from ECEF, and $\mathbf{P}(0|-1) = \mathrm{diag}\,[\,1\times10^4, 1\times10^4, 3\times10^4, 3\times10^2\,]$ is the EKF initial estimation error covariance matrix. Figure 3.13 shows the receiver traversed trajectory during the collection of the pseudorange observations, the true and estimated location of the cellular phone tower, and the uncertainty ellipse produced by the EKF estimation error covariance. Despite the short COpNav receiver trajectory, the tower location estimate was within about 10 meters of the actual tower and within the estimation uncertainty ellipse. This result is consistent with the theoretical prediction that a COpNav receiver with a fully-known initial state can estimate the states of an unknown SOP.

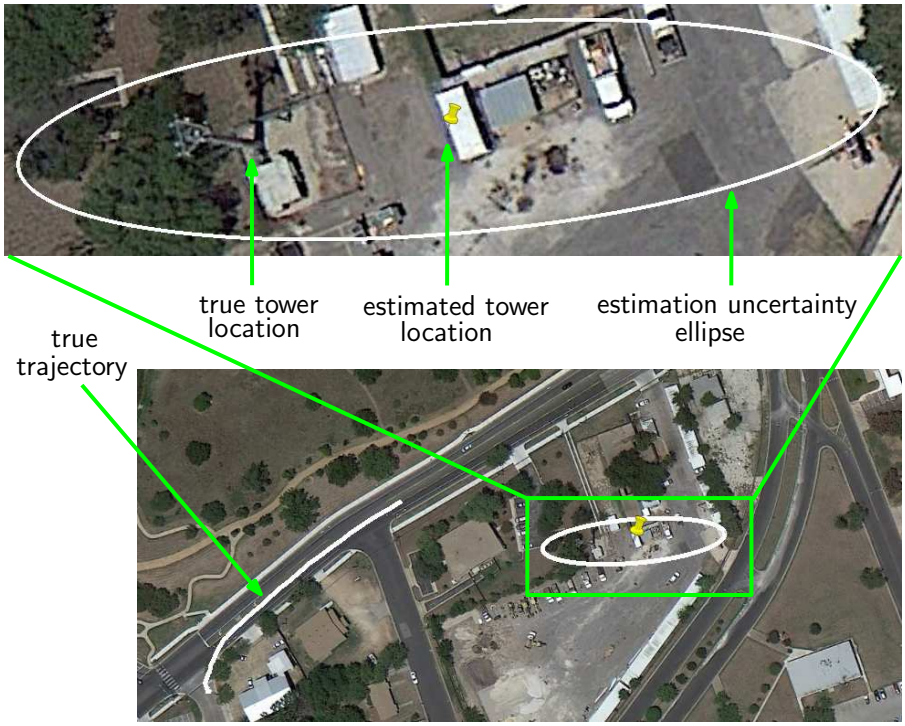

Figure 3.13: Vehicle traversed trajectory during the collection of the GPS and cellular CDMA observations, true location of cellular CDMA tower, and estimated CDMA tower location and associated estimation error ellipse

Chapter 4

Motion Planning for Optimal Information Gathering

Observability, which was studied in Chapter 3, is a Boolean property– it does not specify which trajectories are best for estimability. This chapter synthesizes receiver motion planning algorithms for optimal information gathering in COpNav environments.

This chapter is organized as follows. Section 4.1 summarizes relevant prior work. Section 4.2 focuses on greedy, i.e., one-step look-ahead, receiver motion planning. Several information-based optimization metrics are studied and novel innovation-based optimization metrics are proposed. Convexity properties of all such metrics are analyzed. It is shown that while the information-based metrics possess no desirable convexity properties, the innovation-based optimization problems reduce to search problems over the extreme points of the feasibility region with a computationally efficient solution. Section 4.3 assesses the superiority and limitations of receding horizon, i.e., multi-step look-ahead, strategy over greedy. Section 4.4 studies the problem of collaborative signal landscape mapping with multiple receivers. Several information fusion and decision making architectures are synthesized: centralized,

decentralized, hierarchical without feedback, and hierarchical with feedback. It is demonstrated that the hierarchical with feedback architecture achieves a minimal price of anarchy.

4.1 Relevant Prior Work

Adaptive sensing is the process by which an observer adaptively chooses sensing and motion strategies to maximize the information acquired. Synonymous terms to adaptive sensing include active perception, directed sensing, active information gathering, adaptive sampling, sensor management, path planning, trajectory optimization, and sensor motion control [89].

Optimizing an observer's path in tracking applications has been the subject of extensive research [90–96]. In such problems, the observer, which has perfect knowledge about its own states, is tracking a stationary or a mobile target through its onboard sensors. The trajectory optimization objective is to prescribe optimal trajectories for the observer to follow in order to maintain good estimates about the target's states. Such problems are typically formulated in an optimal control framework.

In SLAM, the problem of trajectory optimization is more involved, due to the coupling between the localization accuracy and the map quality. Initial SLAM research did not take motion control into account and assumed the robot's path to be predetermined or randomly chosen. Of course, not all trajectories a robot can take will be equally beneficial from a localization and mapping accuracy perspective. The problem of trajectory optimization in

SLAM has received considerable attention recently [89, 97–104].

Optimizing the receiver's trajectory in OpNav environments can be thought of as a hybrid of: (*i*) optimizing an observer's path in tracking problems and (*ii*) optimizing the robot's path in SLAM. First, due to the dynamical nature of the clock error states, the SOP's state space is non-stationary, which makes the problem analogous to tracking non-stationary targets. Second, the similarity to SLAM is due to the coupling between the receiver localization accuracy and signal landscape map fidelity.

4.2 Greedy Motion Planning

Recall from Section 3.6 that an OpNav environment comprising a receiver with control over its own maneuvers and multiple terrestrial SOPs is fully-observable if the receiver's initial state vector is fully-known or the initial state vector of one anchor SOP is fully-known. This section focuses on the latter condition, in which case the objective of the receiver's optimal motion planning is to evaluate different sensing actions that the receiver can take, and choose the action that maximizes the information acquired about the SOPs states while simultaneously minimizing the uncertainty about the receiver's own states. The forthcoming discussions can be straightforwardly extended to the former case, in which the objective of the receiver's optimal motion planning is merely signal landscape mapping.

4.2.1 Optimal Greedy Receiver Motion Planning Strategy

The proposed optimal greedy receiver motion planning loop is depicted in Figure 4.1, where $v_{r,\max}$ and $a_{r,\max}$ are the maximum speed and acceleration, respectively, with which the receiver can move. The receiver motion planning loop depicted in Figure 4.1 is composed of the three blocks: (i) OpNav Environment, (ii) Estimator, and (iii) Optimal Greedy Control, which are described next.

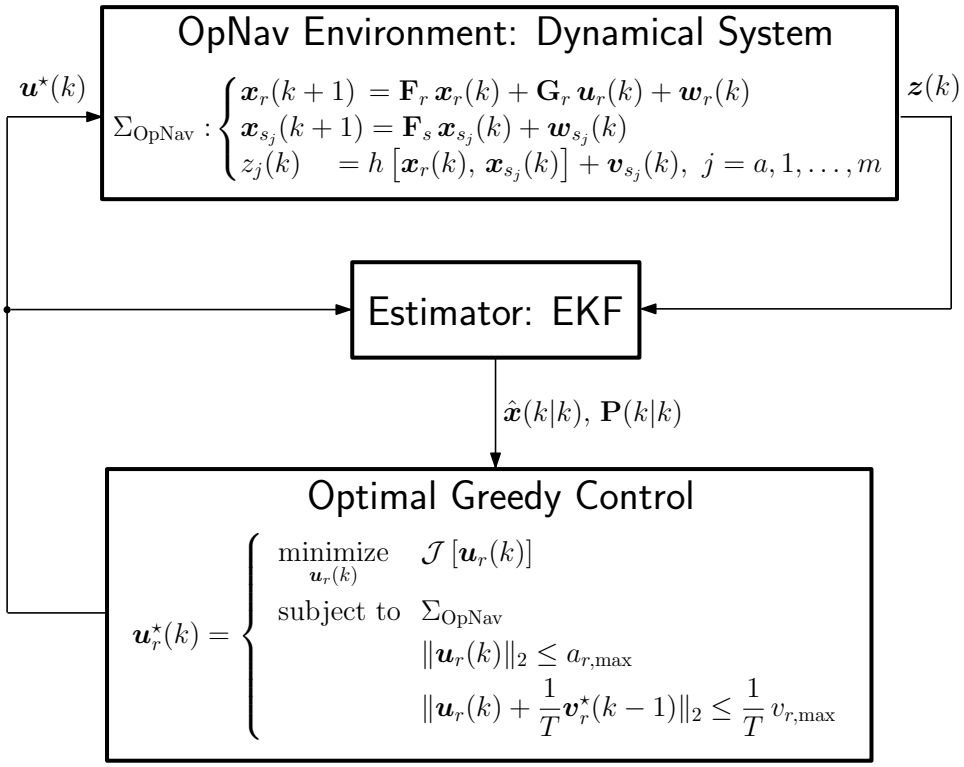

Figure 4.1: Optimal greedy receiver motion planning loop

OpNav Environment This block represents the OpNav environment dynamical and observation models discussed in Chapter 2. The environ-

ment is assumed to comprise a receiver with a state vector $\boldsymbol{x}_r$, a fully-known anchor SOP with a state vector $\boldsymbol{x}_{s_a}$, and m unknown SOPs with state vectors $\{\boldsymbol{x}_{s_i}\}_{i=1}^{m}$.

Estimator The pseudorange observations made by the receiver on all the SOPs, z_{s_j}, where $j = a, 1, \ldots, m$, are fused through an estimator, which is chosen as an EKF for simplicity. Hence, the estimator's dynamics model is given by

$$\boldsymbol{x}\,(k+1) = \mathbf{F}\,\boldsymbol{x}\,(k) + \mathbf{G}\,\boldsymbol{u}\,(k) + \boldsymbol{w}(k),$$

where $\boldsymbol{x} \triangleq \left[\, \boldsymbol{x}_r^{\mathsf{T}}, \boldsymbol{x}_{s_1}^{\mathsf{T}}, \ldots, \boldsymbol{x}_{s_m}^{\mathsf{T}}, \boldsymbol{x}_{\mathrm{clk},s_a}^{\mathsf{T}} \,\right]^{\mathsf{T}}$ is the estimator's state vector, $\{\boldsymbol{x}_{s_i}\}_{i=1}^{m}$ are the state vectors of the m unknown SOPs, $\boldsymbol{x}_{\mathrm{clk},s_a}$ is the clock error states vector of the known anchor SOP, $\boldsymbol{u} \triangleq \boldsymbol{u}_r$ is the control vector, $\mathbf{F} = \mathrm{diag}\,[\,\mathbf{F}_r, \mathbf{F}_s, \ldots, \mathbf{F}_s, \mathbf{F}_{\mathrm{clk}}\,]$, $\mathbf{G} = \left[\, \mathbf{G}_r^{\mathsf{T}}, \mathbf{0}_{2\times 4m+2} \,\right]^{\mathsf{T}}$, and $\boldsymbol{w} \triangleq [\,\boldsymbol{w}_r^{\mathsf{T}}, \boldsymbol{w}_{s_1}^{\mathsf{T}}, \ldots, \boldsymbol{w}_{s_m}^{\mathsf{T}}, \boldsymbol{w}_{\mathrm{clk},s_a}^{\mathsf{T}}\,]^{\mathsf{T}}$ is a zero-mean process noise vector with covariance $\mathbf{Q} = \mathrm{diag}\,[\,\mathbf{Q}_r, \mathbf{Q}_{s_1}, \ldots, \mathbf{Q}_{s_m}, \mathbf{Q}_{\mathrm{clk},s_a}\,]$. The observation vector has the form $\boldsymbol{z} \triangleq [\,\rho_{s_a}, \rho_{s_1}, \ldots, \rho_{s_m}\,]^{\mathsf{T}}$, where ρ_{s_j} is the pseudorange observation made by the receiver on the jth SOP, where $j = a, 1, \ldots, m$. It is assumed that the observation noise elements $v_{\rho_{s_j}}$ are independent; hence, the estimator's observation noise vector is given by $\mathbf{R} = \mathrm{diag}\,[\,r_{s_a}, r_{s_1}, \ldots, r_{s_m}\,]$.

Optimal Greedy Control The state estimate $\hat{\boldsymbol{x}}(k|k)$ and associated estimation error covariance $\mathbf{P}(k|k)$ produced by the EKF are fed to an optimizer, which solves a nonlinear constrained optimization problem

to find the optimal admissible control input $\boldsymbol{u}^\star(k)$, which minimizes a functional $\mathcal{J}$ of the control input, subject to the OpNav environment dynamics and observation models Σ_{OpNav} and velocity and acceleration constraints, specifically

$$\begin{aligned} \underset{\boldsymbol{u}_r(k)}{\text{minimize}} \quad & \mathcal{J}\left[\boldsymbol{u}_r(k)\right] \\ \text{subject to} \quad & \Sigma_{\text{OpNav}} \\ & \|\boldsymbol{u}_r(k)\|_2 \leq a_{r,\max} \\ & \|\boldsymbol{u}_r(k) + \frac{1}{T}\boldsymbol{v}_r^\star(k-1)\|_2 \leq \frac{1}{T}\, v_{r,\max}. \end{aligned}$$

Note that the optimization variable is $\boldsymbol{u}(k)$, whereas $\boldsymbol{v}^\star(k-1)$ is a known constant vector representing the velocity commands that resulted from solving the optimization problem at the previous time-step $k-1$ and has already been applied. The optimal control input $\boldsymbol{u}^\star(k)$ is fed-back to the receiver to command its maneuver and is also communicated with the estimator.

A particular feature of OpNav is that the quality of the estimates not only depends on the spatial trajectory the receiver traverses within the environment, but also on the velocity with which the receiver traverses such trajectory. This can be explained by examining the pseudorange observation model derived in (2.8). Note the term due to the clock biases $c \cdot [\delta t_r(k) - \delta t_s(k)]$, and recall the two state model governing the evolution of the clock bias and drift states over time, which is essentially a double integrator driven by exogenous stochastic processes. Hence, the state space of each SOP contains time-invariant (static) states, x_s and y_s, along with time-varying (dynamic)

states , δt_s and $\dot{\delta} t_s$. This makes the estimation problem similar to that of observers tracking dynamic targets, in which the velocity of the observer (tracker) affects the quality of the estimates. The effect of the receiver's velocity on the quality of the estimates can be also seen by considering a time history of N observations $Z^N \triangleq \{z(1), z(2), \ldots, z(N)\}$, collected at a sampling period T, by a receiver that traversed a particular trajectory at a speed s. If the receiver doubled its speed, i.e., to become $2s$, it could have collected the same number of observations at half the sampling period $T/2$. Recall that the covariance of the process noise characterizing the clock bias and drift $\mathbf{Q}_{\text{clk}}$ is a function of T, T^2, and T^3. Therefore, reducing T effectively reduces $\mathbf{Q}_{\text{clk}}$, which in turn reduces the estimation error.

4.2.2 Information and Innovation Optimization Measures

A fundamental challenge in all optimization-based approaches is the choice of a proper optimization metric. This subsection presents various information- and innovation-based optimization metrics. The main issue with these optimization strategies is the dependency of the objective functional on the parameters to be estimated. This issue is prevalent in the literature and is best described by Cochran as: "You tell me the value of θ, and I promise to design the best experiment for estimating θ [105]."

Information-based metrics are well-established in the literature and are based on the Shannon entropy and Fisher information. Broadly speaking, Shannon entropy is related to the volume of a set containing a specified prob-

ability mass, while Fisher information is related to the surface area of this set [106]. Entropy measures the compactness, and thus the informativeness, of a distribution. The entropy of a random vector $\boldsymbol{x}$ with distribution $p(\boldsymbol{x})$ is defined as [107]

$$H(\boldsymbol{x}) \triangleq -\int_{\infty}^{\infty} p(\boldsymbol{x}) \log[p(\boldsymbol{x})] d\boldsymbol{x}.$$

The mutual information gain after an action $\boldsymbol{u}$ is defined as $\Delta I(\boldsymbol{u}) \triangleq H(\boldsymbol{x}) - H(\boldsymbol{x}|\boldsymbol{u})$, where $H(\boldsymbol{x}|\boldsymbol{u})$ is the conditional entropy after action $\boldsymbol{u}$. Thus, $\Delta I(\boldsymbol{u})$ is a measure of the reduction in the uncertainty in $\boldsymbol{x}$ due to the action $\boldsymbol{u}$. A multi-variate Gaussian random vector $\boldsymbol{x}$ has entropy proportional to the logarithm of the determinant of its covariance matrix $\mathbf{P}$, namely $H(\boldsymbol{x}) = \frac{1}{2}\log[(2\pi e)^n \det(\mathbf{P})]$. Therefore, for a Gaussian random vector $\boldsymbol{x}(k)$ with covariance $\mathbf{P}(k)$, it can be shown that to maximize the mutual information after an action $\boldsymbol{u}(k)$, one needs to solve the optimization problem

$$\underset{\boldsymbol{u}(k)}{\text{maximize}} \quad \log\det\left[\frac{\mathbf{Y}[k+1|\boldsymbol{u}(k)]}{\mathbf{Y}(k)}\right],$$

where $\mathbf{Y}(k) \triangleq \mathbf{P}^{-1}(k)$ is the information matrix and $\mathbf{Y}[k+1|\boldsymbol{u}(k)]$ is the information matrix after action $\boldsymbol{u}(k)$. Recognizing that $\mathbf{Y}(k)$ corresponds to the Fisher information matrix, one can establish the connection between Shannon entropy and Fisher information: minimization of Shannon entropy is equivalent to maximization of Fisher information. This is the basis of the so-called D-optimality criterion. Some of the most common information-based optimization measures are defined next [108].

Definition 4.2.1. Given an information matrix, $\mathbf{Y}$, the D-, A-, and E-optimality criteria are defined as

D-optimality: is equivalent to minimization of the volume of the uncertainty ellipsoid, and is given by

$$\text{minimize } \mathcal{J} = -\log\det\left[\mathbf{Y}\right].$$

A-optimality: is equivalent to minimization of the average variance of the estimates, and is given by

$$\text{minimize } \mathcal{J} = \text{tr}\left[\mathbf{Y}^{-1}\right].$$

E-optimality: is equivalent to minimization of the length of the largest axis of the uncertainty ellipsoid, and is given by

$$\text{minimize } \mathcal{J} = \lambda_{\max}\left[\mathbf{Y}^{-1}\right],$$

where $\lambda_{\max}$ is the largest eigenvalue.

In contrast to the information-based criteria, which sought to minimize a functional of the information matrix, the innovation-based criteria seek to maximize a functional of the innovation matrix. Innovation-based optimization has not received as much attention in the literature as information-based [109, 110]. Intuitively, one seeks the receiver maneuver that yields the most observation innovation, i.e., the "most difficult" observation to predict. The innovation-based optimization criteria: most innovative logarithm-determinant (MILD), most innovative trace (MIT), and most innovative maximum eigenvalue (MIME) are defined next [111].

Definition 4.2.2. Given an innovation matrix, $\mathbf{S}$, the MILD, MIT, and MIME criteria are defined as

MILD: is equivalent to maximization of the volume of the innovation ellipsoid, and is given by

$$\text{maximize } \mathcal{J} = \log\det\left[\mathbf{S}\right].$$

MIT: is equivalent to maximization of the average innovations, and is given by

$$\text{maximize } \mathcal{J} = \text{tr}\left[\mathbf{S}\right].$$

MIME: is equivalent to maximization of the length of the largest axis of the innovation ellipsoid, and is given by

$$\text{maximize } \mathcal{J} = \lambda_{\max}\left[\mathbf{S}\right],$$

where $\lambda_{\max}$ is the largest eigenvalue.

4.2.3 Information-Based Optimal Motion Planning

The information-based motion planning optimization problems are formulated in this subsection. Given the estimate $\hat{\boldsymbol{x}}(k|k)$ and associated estimation error covariance $\mathbf{P}(k|k)$, the predicted state vector $\hat{\boldsymbol{x}}(k+1|k)$ and associated prediction error covariance $\mathbf{P}(k+1|k)$ are given by

$$\hat{\boldsymbol{x}}(k+1|k) = \mathbf{F}\hat{\boldsymbol{x}}(k|k) + \mathbf{G}\boldsymbol{u}(k)$$
$$\mathbf{P}(k+1|k) = \mathbf{F}\mathbf{P}(k|k)\mathbf{F}^{\mathsf{T}} + \mathbf{Q}.$$

Note that $\mathbf{P}(k+1|k)$ is not a function of $\boldsymbol{u}(k)$. The observation jacobian matrix, evaluated at $\hat{\boldsymbol{x}}(k+1|k)$, is given by

$$\mathbf{H} = \begin{bmatrix} \mathbf{h}_1^{\mathsf{T}}(\hat{\boldsymbol{r}}_r, \boldsymbol{u}, \boldsymbol{r}_{s_a}) & \mathbf{0}_{1\times 4} & \cdots & \mathbf{0}_{1\times 4} \\ \mathbf{h}_1^{\mathsf{T}}(\hat{\boldsymbol{r}}_r, \boldsymbol{u}, \hat{\boldsymbol{r}}_{s_1}) & \mathbf{h}_2^{\mathsf{T}}(\hat{\boldsymbol{r}}_r, \boldsymbol{u}, \hat{\boldsymbol{r}}_{s_1}) & \cdots & \mathbf{0}_{1\times 4} \\ \vdots & \vdots & \ddots & \vdots \\ \mathbf{h}_1^{\mathsf{T}}(\hat{\boldsymbol{r}}_r, \boldsymbol{u}, \hat{\boldsymbol{r}}_{s_m}) & \mathbf{0}_{1\times 4} & \cdots & \mathbf{h}_2^{\mathsf{T}}(\hat{\boldsymbol{r}}_r, \boldsymbol{u}, \hat{\boldsymbol{r}}_{s_m}) \end{bmatrix}$$

$$\begin{aligned} \mathbf{h}_1^{\mathsf{T}}(\boldsymbol{r}_r, \boldsymbol{u}, \boldsymbol{r}_{s_j}) &\triangleq \begin{bmatrix} g_1(\boldsymbol{r}_r, \boldsymbol{u}, \boldsymbol{r}_{s_j}) & g_2(\boldsymbol{r}_r, \boldsymbol{u}, \boldsymbol{r}_{s_j}) & 0 & 0 & c & 0 \end{bmatrix} \\ \mathbf{h}_2^{\mathsf{T}}(\boldsymbol{r}_r, \boldsymbol{u}, \boldsymbol{r}_{s_j}) &\triangleq \begin{bmatrix} -g_1(\boldsymbol{r}_r, \boldsymbol{u}, \boldsymbol{r}_{s_j}) - g_2(\boldsymbol{r}_r, \boldsymbol{u}, \boldsymbol{r}_{s_j}) & -c & 0 \end{bmatrix} \end{aligned}$$

$$\begin{aligned} g_1(\boldsymbol{r}_r, \boldsymbol{u}, \boldsymbol{r}_{s_j}) &\triangleq \frac{x_r + T\dot{x}_r + \frac{T^2}{2}u_1 - x_{s_j}}{\|\boldsymbol{r}_r + T\dot{\boldsymbol{r}} + \frac{T^2}{2}\boldsymbol{u} - \boldsymbol{r}_{s_j}\|_2} \\ g_2(\boldsymbol{r}_r, \boldsymbol{u}, \boldsymbol{r}_{s_j}) &\triangleq \frac{y_r + T\dot{y}_r + \frac{T^2}{2}u_2 - y_{s_j}}{\|\boldsymbol{r}_r + T\dot{\boldsymbol{r}} + \frac{T^2}{2}\boldsymbol{u} - \boldsymbol{r}_{s_j}\|_2}, \end{aligned}$$

where $j = a, 1, \ldots, m$, and the time dependency has been dropped above for compactness of notation, namely $\mathbf{H} = \mathbf{H}(k+1)$, $\hat{\boldsymbol{r}}_r = \hat{\boldsymbol{r}}_r(k+1|k)$, $\boldsymbol{u} = \boldsymbol{u}(k)$, $\boldsymbol{r}_{s_a} = \boldsymbol{r}_{s_a}(k)$, $\hat{\boldsymbol{r}}_{s_j} = \hat{\boldsymbol{r}}_{s_j}(k+1|k)$. The updated covariance matrix is given by

$$\mathbf{P}^{-1}(k+1|k+1) = \mathbf{P}^{-1}(k+1|k) + \mathbf{H}^{\mathsf{T}}(k+1)\mathbf{R}^{-1}\mathbf{H}(k+1).$$

It is worth noting that $\mathbf{P}(k+1|k+1)$ is a function of $\boldsymbol{u}(k)$ and can be computed without knowledge of the observation at the next time-step, namely $\boldsymbol{z}(k+1)$. The cost functional $\mathcal{J}[\boldsymbol{u}(k)]$ can be chosen to be the D-, A-, or E-optimality criterion defined in Definition 4.2.1, where $\mathbf{Y} = \mathbf{P}^{-1}(k+1|k+1)$.

Ideally, one would like to solve the optimization problem analytically using Lagrange multipliers. However, the problem quickly becomes intractable

as more SOPs are present in the environment. If no analytical solution can be obtained, one typically resorts to numerical optimization solvers. Nevertheless, convexity properties of the problem are sought, if possible, which enables utilization of efficient convex solvers, such as CVX [112]. Plotting $\mathcal{J}[\boldsymbol{u}(k)]$ reveals that the D-, A-, and E-optimality criteria are neither convex nor concave as illustrated in Figure 4.2 for a random OpNav environment comprising a receiver and four SOPs.

4.2.4 Innovation-Based Optimal Motion Planning

This subsection formulates the innovation-based optimization problems and shows that with proper reformulation and reasonable approximations such optimization problems have strong convexity properties. Moreover, it is shown that the MILD, MIT, and MIME optimization problems reduce to searching over the extreme points of the feasibility region.

Theorem 4.2.1. *For a sufficiently small sampling period T and with proper reformulation, the innovation matrix $\mathbf{S}(k+1)$ is affine in the control inputs, specifically*

$$\mathbf{S}(k+1) = \mathbf{S}_0(k+1) + \sum_{i=1}^{2} \mathbf{S}_i(k+1)u_i(k). \tag{4.1}$$

Proof. First, consider transforming the receiver and SOP dynamics in (2.1)-(2.3) and observation model in (2.7) into a polar coordinate frame centered at the receiver (x_r, y_r), such that $(x_j, y_j) \mapsto (r_{s_j}, \theta_{s_j})$, where $x_j \triangleq x_r - x_{s_j}$,

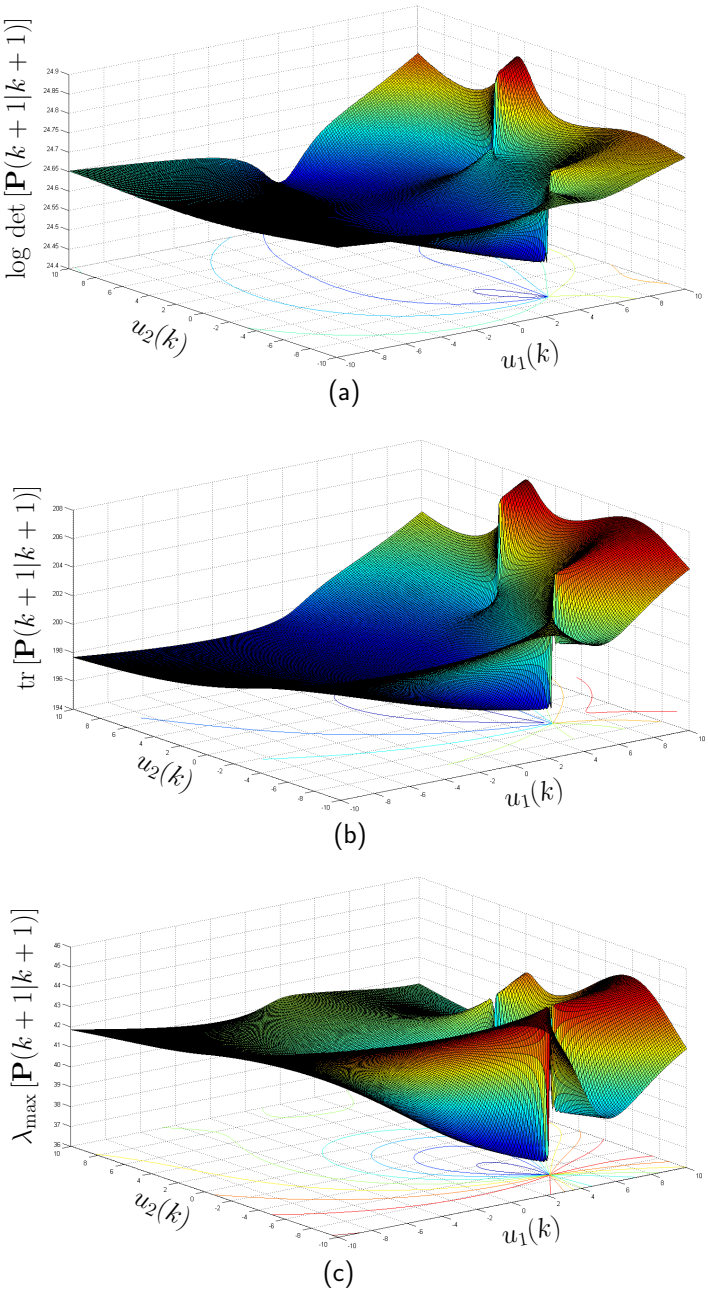

Figure 4.2: D-, A-, and E-optimality optimization functionals for an OpNav environment with a receiver and four SOPs

$y_j \triangleq y_r - y_{s_j}$, and

$$\begin{cases} r_{s_j} = \sqrt{x_j^2 + y_j^2} \\ \theta_{s_j} = \tan^{-1}\left(\frac{y_j}{x_j}\right) \end{cases} \quad \Leftrightarrow \quad \begin{cases} x_j = r_{s_j} \cos\theta_{s_j} \\ y_j = r_{s_j} \sin\theta_{s_j} \end{cases}$$

where the $\tan^{-1}(\bullet)$ function is interpreted as the unambiguous four-quadrant arctan function, commonly referred to as $\text{atan2}(y, x)$. Hence, the transformed state has the form $\boldsymbol{x}' \triangleq \boldsymbol{g}(\boldsymbol{x}) = \Big[\boldsymbol{\xi}_{s_a}^{\mathsf{T}}, \dot{\boldsymbol{\xi}}_{s_a}^{\mathsf{T}}, \boldsymbol{\xi}_{s_1}^{\mathsf{T}}, \dot{\boldsymbol{\xi}}_{s_1}^{\mathsf{T}}, \ldots, \boldsymbol{\xi}_{s_m}^{\mathsf{T}}, \dot{\boldsymbol{\xi}}_{s_m}^{\mathsf{T}}, \boldsymbol{x}_{\text{clk},r}^{\mathsf{T}}, \boldsymbol{x}_{\text{clk},s_1}^{\mathsf{T}}, \ldots, \boldsymbol{x}_{\text{clk},s_m}^{\mathsf{T}}, \boldsymbol{x}_{\text{clk},s_a}^{\mathsf{T}}\Big]^{\mathsf{T}}$, where $\boldsymbol{\xi}_{s_j} \triangleq \big[r_{s_j}, \theta_{s_i}\big]^{\mathsf{T}}$, $j = a, 1, \ldots, m$. It can be readily shown that in the transformed coordinate frame the dynamics are nonlinear in the states, yet affine in the control inputs, while the observations are linear time-invariant, specifically

$$\begin{aligned} \dot{\boldsymbol{x}}'(t) &= \boldsymbol{f}_0'\left[\boldsymbol{x}'(t)\right] + \sum_{i=1}^{2} \boldsymbol{f}_i'\left[\boldsymbol{x}'(t)\right] u_i(t) + \tilde{\boldsymbol{w}}'(t) \\ \boldsymbol{z}(t) &= \mathbf{H}'\boldsymbol{x}'(t) + \tilde{\boldsymbol{v}}(t), \end{aligned} \tag{4.2}$$

$$\boldsymbol{f}_i' = \big[\boldsymbol{f}_{i,s_a}', \boldsymbol{f}_{i,s_1}', \ldots, \boldsymbol{f}_{i,s_m}', \boldsymbol{f}_{i,\text{clk},r}', \boldsymbol{f}_{i,\text{clk},s_1} \ldots, \boldsymbol{f}_{i,\text{clk},s_m}', \boldsymbol{f}_{i,\text{clk},s_a}'\big]^{\mathsf{T}}$$

$$\boldsymbol{f}_{0,s_j}' = \left[\dot{r}_{s_j}, \dot{\theta}_{s_j}, r_{s_j}\dot{\theta}_{s_j}^2, \frac{-2\,\dot{r}_{s_j}\dot{\theta}_{s_j}}{r_{s_j}}\right]^{\mathsf{T}}, \quad \boldsymbol{f}_{0,\text{clk},r}' = \Big[\dot{\delta t}_r,\, 0\Big]^{\mathsf{T}}$$

$$\boldsymbol{f}_{1,s_j}' = \left[0,\, 0, \cos\theta_{s_j},\, \frac{-\sin\theta_{s_j}}{r_{s_j}}\right]^{\mathsf{T}}, \quad \boldsymbol{f}_{0,\text{clk},s_j}' = \Big[\dot{\delta t}_{s_j},\, 0\Big]^{\mathsf{T}}$$

$$\boldsymbol{f}_{2,s_j}' = \left[0,\, 0,\, \sin\theta_{s_j},\, \frac{\cos\theta_{s_j}}{r_{s_j}}\right]^{\mathsf{T}}$$

$$\boldsymbol{f}_{1,\text{clk},r}' = \boldsymbol{f}_{1,\text{clk},s_j}' = \boldsymbol{f}_{2,\text{clk},r}' = \boldsymbol{f}_{2,\text{clk},s_j}' = \mathbf{0}_{2\times 1}$$

$$\tilde{\boldsymbol{w}}' = \big[\tilde{\boldsymbol{w}}_{s_a}',\, \tilde{\boldsymbol{w}}_{s_1}',\, \ldots, \tilde{\boldsymbol{w}}_{s_m}',\, \tilde{\boldsymbol{w}}_{\text{clk},r},\, \tilde{\boldsymbol{w}}_{\text{clk},s_1},\, \ldots,\, \tilde{\boldsymbol{w}}_{\text{clk},s_m},\, \tilde{\boldsymbol{w}}_{\text{clk},s_a}\big]^{\mathsf{T}}$$

$$\tilde{\boldsymbol{w}}_{s_j}' = \Big[0,\, 0, \tilde{w}_{1,s_j}',\, \tilde{w}_{2,s_j}'\Big]^{\mathsf{T}},$$

where $i = 0, 1, 2$ and $j = a, 1, \ldots, m$. The transformed process noise vector $\tilde{\boldsymbol{w}}'$ is zero-mean, white with a power spectral density $\tilde{\mathbf{Q}}'(t)$, such that

$$\tilde{\mathbf{Q}}' = \text{diag}\left[\, \tilde{\mathbf{Q}}'_{s_a}, \tilde{\mathbf{Q}}'_{s_1}, \ldots, \tilde{\mathbf{Q}}'_{s_m}, \tilde{\mathbf{Q}}_{\text{clk},r}, \tilde{\mathbf{Q}}_{\text{clk},s_1}, \ldots, \tilde{\mathbf{Q}}_{\text{clk},s_m}, \tilde{\mathbf{Q}}_{\text{clk},s_a} \,\right]$$

$$\tilde{\mathbf{Q}}'_{s_j} = \boldsymbol{\Psi}\left(\boldsymbol{\xi}_{s_j}\right) \text{diag}\left[\, 0,\, 0, \tilde{q}_x,\, \tilde{q}_y \,\right] \boldsymbol{\Psi}^{\mathsf{T}}\left(\boldsymbol{\xi}_{s_j}\right)$$

$$\boldsymbol{\Psi}\left(\boldsymbol{\xi}_{s_j}\right) \triangleq \begin{bmatrix} 0 & 0 & 0 & 0 \\ 0 & 0 & 0 & 0 \\ 0 & 0 & \cos\theta_{s_j} & \sin\theta_{s_j} \\ 0 & 0 & \frac{-\sin\theta_{s_j}}{r_{s_j}} & \frac{\cos\theta_{s_j}}{r_{s_j}} \end{bmatrix}, \quad j = a, 1, \ldots, m$$

$$\mathbf{H}' = \begin{bmatrix} \mathbf{h}'^{\mathsf{T}}_{s_a} & \mathbf{0} & \cdots & \mathbf{0} & \mathbf{h}'^{\mathsf{T}}_{\text{clk},r} & \mathbf{0} & \cdots & \mathbf{0} & \mathbf{h}'^{\mathsf{T}}_{\text{clk},s_a} \\ \mathbf{0} & \mathbf{h}'^{\mathsf{T}}_{s_1} & \cdots \mathbf{0} & \mathbf{h}'^{\mathsf{T}}_{\text{clk},r} & \mathbf{h}'^{\mathsf{T}}_{\text{clk},s_1} & \cdots & \mathbf{0} & \mathbf{0} & \mathbf{0} \\ \vdots & \vdots & \ddots & \vdots & \vdots & \vdots & \ddots & \vdots & \vdots \\ \mathbf{0} & \mathbf{0} & \cdots & \mathbf{h}'^{\mathsf{T}}_{s_m} & \mathbf{h}'^{\mathsf{T}}_{\text{clk},r} & \mathbf{0} & \cdots & \mathbf{h}'^{\mathsf{T}}_{\text{clk},s_m} & \mathbf{0} \end{bmatrix}$$

$$\mathbf{h}'^{\mathsf{T}}_{s_j} \triangleq [\, 1,\, 0,\, 0,\, 0 \,], \quad \mathbf{h}'^{\mathsf{T}}_{\text{clk},r} \triangleq [\, c,\, 0 \,], \quad \mathbf{h}^{\mathsf{T}}_{\text{clk},s_j} = -\mathbf{h}'^{\mathsf{T}}_{\text{clk},r}.$$

Next, the nonlinear dynamics in (4.2) is linearized around nominal $\boldsymbol{x}^o_j$ and $\boldsymbol{u}^o$ to yield the linear time-varying system

$$\frac{d}{dt}\delta\boldsymbol{x}'(t) = \mathbf{F}'(t)\delta\boldsymbol{x}'(t) + \mathbf{G}'(t)\delta\boldsymbol{u}(t) + \tilde{\boldsymbol{w}}'(t), \tag{4.3}$$

where $\delta\boldsymbol{x}' \triangleq \boldsymbol{x}' - \boldsymbol{x}^o$ and $\delta\boldsymbol{u} \triangleq \boldsymbol{u} - \boldsymbol{u}^o$. It can be readily shown that $\mathbf{F}'(t)$ is affine in the control inputs, namely

$$\mathbf{F}'(t) = \mathbf{F}'_0(t) + \sum_{i=1}^{2} \mathbf{F}'_i(t)\, u_i(t)$$

$$\begin{aligned} \mathbf{F}'_0(t) &= \text{diag}\left[\, \mathbf{F}'_{0,s_a}(t), \mathbf{F}'_{0,s_1}(t), \ldots, \mathbf{F}'_{0,s_m}(t), \mathbf{A}_{\text{clks}} \,\right], \\ \mathbf{F}'_i(t) &= \text{diag}\left[\, \mathbf{F}'_{i,s_a}(t), \mathbf{F}'_{i,s_1}(t), \ldots, \mathbf{F}'_{i,s_m}(t), \mathbf{0}_{(2m+4)\times(2m+4)} \,\right] \end{aligned}$$

$$
\begin{aligned}
\mathbf{F}'_{0,s_j}(t) &= \begin{bmatrix} 0 & 0 & 1 & 0 \\ 0 & 0 & 0 & 1 \\ \dot{\theta}^2_{s_j} & 0 & 0 & 2\,r_{s_j}\dot{\theta}_{s_j} \\ \frac{2\,\dot{r}_{s_j}\dot{\theta}_{s_j}}{r^2_{s_j}} & 0 & \frac{-2\,\dot{\theta}_{s_j}}{r_{s_j}} & \frac{-2\dot{r}_{s_j}}{r_{s_j}} \end{bmatrix} \\
\mathbf{F}'_{1,s_j}(t) &= \begin{bmatrix} 0 & 0 & 0 & 0 \\ 0 & 0 & 0 & 0 \\ 0 & -\sin\theta_{s_j} & 0 & 0 \\ \frac{\sin\theta_{s_j}}{r^2_{s_j}} & \frac{-\cos\theta_{s_j}}{r_{s_j}} & 0 & 0 \end{bmatrix} \\
\mathbf{F}'_{2,s_j}(t) &= \begin{bmatrix} 0 & 0 & 0 & 0 \\ 0 & 0 & 0 & 0 \\ 0 & \cos\theta_{s_j} & 0 & 0 \\ \frac{-\cos\theta_{s_j}}{r^2_{s_j}} & \frac{-\sin\theta_{s_j}}{r_{s_j}} & 0 & 0 \end{bmatrix},
\end{aligned}
$$

where $j = a, 1, \ldots, m$ and $\mathbf{A}_{\text{clks}}$ is block-diagonal consisting of $m+2$ blocks of $\mathbf{A}_{\text{clk}}$.

Then, the linearized system in (4.3) is discretized by assuming $\mathbf{F}'(t)$, $\mathbf{G}'(t)$, and $\tilde{\mathbf{Q}}'(t)$ to be approximately constant over a sampling interval T, i.e., $\mathbf{F}'(t) \approx \mathbf{F}'(k)$, $\mathbf{G}'(t) \approx \mathbf{G}'(k)$, and $\tilde{\mathbf{Q}}'(t) \approx \tilde{\mathbf{Q}}'(k)$, and assuming zero-order hold (ZOH) of the control inputs, i.e., $\{u(t) = u(k),\, k \le t < k+1\}$ to yield [113]

$$
\begin{aligned}
\boldsymbol{x}'(k+1) &= \boldsymbol{\Phi}'(k+1,k)\,\boldsymbol{x}'(k) + \boldsymbol{\Gamma}'\,\boldsymbol{u}(k) + \boldsymbol{w}'(k) \\
\boldsymbol{\Gamma}'(k+1,k) &\triangleq \int_k^{k+1} e^{\mathbf{F}'(k)[k+1-\tau]}\,\mathbf{G}(k)\,d\tau,
\end{aligned}
$$

$\boldsymbol{\Phi}'(k+1,k) \triangleq e^{\mathbf{F}'(k)T}$, and $\boldsymbol{w}'(k)$ is a zero-mean white stochastic sequence with covariance $\mathbf{Q}'(k+1,k)$ given by

$$
\mathbf{Q}'(k+1,k) = \int_k^{k+1} e^{\mathbf{F}'(k)[k+1-\tau]}\,\tilde{\mathbf{Q}}'(k)\,e^{\mathbf{F}'^{\mathsf{T}}(k)[k+1-\tau]}d\tau.
$$

Note that the state transition matrix $\mathbf{\Phi}'(k+1,k)$ is now a matrix exponential, since $\mathbf{F}(t)$ is assumed to be constant over T. The matrix exponential can be factored as

$$\mathbf{\Phi}'(k+1,k) = \mathbf{\Xi}(k)\, e^{T\sum_{i=1}^{2}\mathbf{F}'_i(k)u_i(k)},$$

where $\mathbf{\Xi}(k) \triangleq e^{T\mathbf{F}'_0(k)}$. Note that the above factorization holds, since the matrices $\mathbf{F}'_0(k)$ and $\sum_{i=1}^{2}\mathbf{F}'_i(k)u_i(k)$ can be readily shown to be commutative (see Section 1.1 in Appendix 1). Next, the matrix exponential $e^{T\sum_{i=1}^{2}\mathbf{F}'_i(k)u_i(k)}$ is expressed as a Taylor series and assuming sufficiently small values of T, the series is truncated to the first-order power in T. Therefore, the state transition matrix is expressible as

$$\mathbf{\Phi}'(k+1,k) \;=\; \mathbf{\Xi}(k) + T\sum_{i=1}^{2}\mathbf{\Xi}(k)\mathbf{F}'_i(k)u_i(k).$$

Proceeding in a similar manner for $\mathbf{Q}'(k+1,k)$, it is straightforward to show that $\mathbf{Q}'(k+1,k) \approx T\,\mathbf{Q}'(k)$.

Next, the predicted error covariance is given by

$$\mathbf{P}'(k+1|k) = \mathbf{\Phi}'(k+1,k)\mathbf{P}'(k|k)\mathbf{\Phi}'^{\mathsf{T}}(k+1,k) + \mathbf{Q}'(k+1,k).$$

Note that to evaluate $\mathbf{P}'(k+1|k)$, which corresponds to the transformed state $\boldsymbol{x}'(k)$, one needs $\mathbf{P}'(k|k)$ in the transformed state-space. Given the state estimate $\hat{\boldsymbol{x}}(k|k)$ in the original state-space and associated $\mathbf{P}(k|k)$, one can find the transformed $\mathbf{P}'(k|k)$ via linearization around $\hat{\boldsymbol{x}}(k|k)$ as

$$\boldsymbol{x}' = \boldsymbol{g}(\boldsymbol{x}) \approx \boldsymbol{g}\left[\hat{\boldsymbol{x}}(k|k)\right] + \nabla_{\boldsymbol{x}}\,\boldsymbol{g}(\boldsymbol{x})\Big|_{\boldsymbol{x}=\hat{\boldsymbol{x}}(k|k)} \cdot \left[\boldsymbol{x} - \hat{\boldsymbol{x}}(k|k)\right].$$

Defining $\mathbf{\Lambda}(k) \triangleq \nabla_{\boldsymbol{x}} \boldsymbol{g}(\boldsymbol{x})|_{\boldsymbol{x}=\hat{\boldsymbol{x}}(k|k)}$ and recognizing that $\mathrm{cov}\,[\boldsymbol{x} - \hat{\boldsymbol{x}}(k|k)] = \mathbf{P}(k|k)$ yields

$$\mathbf{P}'(k+1|k) = \mathbf{\Lambda}(k)\mathbf{P}(k+1|k)\mathbf{\Lambda}^{\mathsf{T}}(k). \tag{4.4}$$

Explicit expression for $\mathbf{\Lambda}(k)$ is given in Appendix 1.2 in Appendix 1.

Substituting for $\mathbf{\Phi}'(k+1,k)$ and truncating to the first-order power in T, it can be shown that the predicted error covariance is affine in the control inputs, specifically

$$\mathbf{P}'(k+1|k) = \mathbf{P}'_0(k+1|k) + \sum_{i=1}^{2} \mathbf{P}'_i(k+1|k)u_i(k)$$

$$\mathbf{P}'_0(k+1|k) \triangleq \mathbf{\Xi}(k)\mathbf{P}'(k|k)\mathbf{\Xi}^{\mathsf{T}}(k) + \mathbf{Q}'(k+1,k)$$

$$\mathbf{P}'_i(k+1|k) \triangleq T\Big[\mathbf{\Xi}(k)\mathbf{P}'(k|k)\mathbf{F}_i'^{\mathsf{T}}(k)\mathbf{\Xi}^{\mathsf{T}}(k) + \mathbf{\Xi}(k)\mathbf{F}'_i(k)\mathbf{P}'(k|k)\mathbf{\Xi}^{\mathsf{T}}(k)\Big],\ i = 1, 2.$$

Finally, the observation innovation $\tilde{\boldsymbol{z}}'(k+1) \triangleq \boldsymbol{z}(k+1) - \hat{\boldsymbol{z}}'(k+1|k)$, where $\hat{\boldsymbol{z}}'(k+1|k) = \mathbf{H}'\hat{\boldsymbol{x}}'(k+1|k)$, has a corresponding covariance $\mathbf{S}'(k+1)$ given by

$$\mathbf{S}'(k+1) = \mathbf{H}'\mathbf{P}'(k+1|k)\mathbf{H}'^{\mathsf{T}} + \mathbf{R},$$

and (4.1) follows with $\mathbf{S}'_0(k+1) = \mathbf{H}\mathbf{P}'_0(k+1|k)\mathbf{H}^{\mathsf{T}} + \mathbf{R}$ and $\mathbf{S}'_i(k+1) = \mathbf{H}\mathbf{P}'_i(k+1|k)\mathbf{H}^{\mathsf{T}}$, for $i = 1, 2$. □

The special affine form of the innovation matrix in (4.1) yields the following result regarding the optimal solution of the innovation-based optimization problems.

Theorem 4.2.2. *The optimal solutions for the innovation-based greedy motion planning problems: MILD, MIT, and MIME lie on the extreme points of the feasibility region.*

Proof. First, it easy to see that the velocity and acceleration constraints are convex in the optimization variable $\boldsymbol{u}(k)$, since the norm of a vector is convex and the composition of a convex function with an affine mapping preserves convexity [114]. Next, we show that MILD is a concave function, whereas MIT and MIME are convex functions. To this end, concavity of MILD follows from Lemma 1.3.1 in Section 1.3 of Appendix 1. Moreover, since MIT is affine in the optimization variable, it is both convex and concave. Convexity of MIME follows from Lemma 1.3.2 in Section 1.3 of Appendix 1. Hence, in the MILD case, one is maximizing a concave functional subject to convex constraints. But, since the logarithm functional is strictly monotonically increasing, the maximum is attained at the extreme points of the feasibility region. In the MIT and MIME case, one is maximizing convex functionals subject to convex constraints; therefore, the maximum is attained at the extreme points of the feasibility region [115]. □

The significance of Theorem 4.2.2 is that the innovation-based optimization problems reduce to search problems via function evaluations. Figure 4.3(a) illustrates the control feasibility region over which the information- and innovation-based optimization functionals need to be considered. Figure 4.3(b)

illustrates the extreme points of the feasibility region over which the optimal solution of the innovation-based functionals lies.

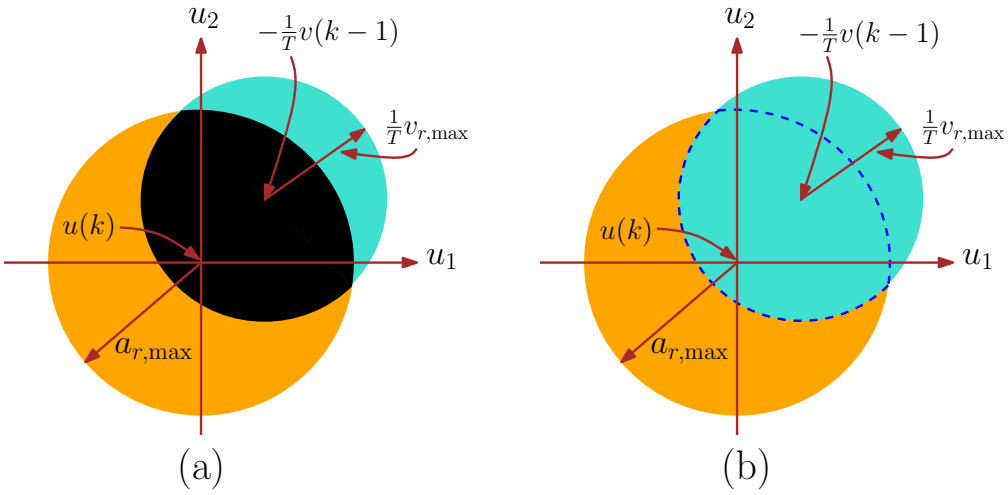

Figure 4.3: (a) Black shaded region: control feasibility region for information- and innovation-based optimization. (b) Dashed curve: extreme points of feasibility region over which the optimal solution of innovation-based optimization lies

4.2.5 Relationship between D-Optimality and MILD

Under linear Gaussian assumptions, one can show that D-optimality and MILD are equivalent. To see this, consider two jointly Gaussian random vectors $\boldsymbol{x}$ and $\boldsymbol{z}$ with auto- and cross-covariances given by $\mathbf{P}_{\boldsymbol{xx}}$, $\mathbf{P}_{\boldsymbol{zz}}$, and $\mathbf{P}_{\boldsymbol{xz}}$. Assume that $\boldsymbol{z} = \mathbf{H}\boldsymbol{x} + \boldsymbol{v}$, where $\boldsymbol{v} \sim \mathcal{N}(\mathbf{0}, \mathbf{R})$ is independent of $\boldsymbol{x}$. Then, the mutual information between $\boldsymbol{x}$ and $\boldsymbol{z}$, which measures the expected reduction in entropy in one random vector due to the observation of another, can be

shown through the Kullback-Leibler divergence to be given by [116]

$$I(\boldsymbol{x},\boldsymbol{z}) = \frac{1}{2}\log\frac{\det\left[\mathbf{P}_{\boldsymbol{xx}}^{-1}+\mathbf{H}^{\mathsf{T}}\mathbf{R}^{-1}\mathbf{H}\right]}{\det\left[\mathbf{P}_{\boldsymbol{xx}}^{-1}\right]} \tag{4.5}$$

$$= \frac{1}{2}\log\frac{\det\left[\mathbf{H}\,\mathbf{P}_{\boldsymbol{xx}}\,\mathbf{H}^{\mathsf{T}}+\mathbf{R}\right]}{\det\left[\mathbf{R}\right]}. \tag{4.6}$$

Therefore, to maximize $I(\boldsymbol{x},\boldsymbol{z})$ one can either maximize the right-hand side of (4.5) or (4.6). Interpreting $\mathbf{P}_{\boldsymbol{xx}}$ as the prediction error covariance, which is not a function of $\boldsymbol{u}$ as shown in Subsection 4.2.3, it can be established that the former maximization is nothing but D-optimality, while the latter maximization is MILD.

4.2.6 Simulation Results

This section presents simulation results comparing greedy information- and innovation-based receiver motion strategies as well as random and predefined trajectories [111, 117]. A receiver with an unknown initial state vector was assumed to be dropped in an OpNav environment comprising an anchor SOP with a known initial state vector, labeled SOP_a, and three SOPs with unknown initial state vectors, labeled $\{\text{SOP}_i\}_{i=1}^{3}$. The receiver's clock was assumed to be a TCXO, while the SOPs were assumed to be equipped with OCXO clocks. For purposes of numerical stability, the clock error states were defined to be $c\delta t$ and $c\dot{\delta t}$. The simulation settings are given in Table 4.1.

Eight receiver trajectories were simulated. The first two were open-loop: one in which the receiver's maneuvers were chosen randomly, while in the other, the maneuvers were specified so to traverse a trajectory around

Table 4.1: Greedy motion planning simulation settings

Parameter	**Value**
$\boldsymbol{x}_r(0)$	$[\,0,\ 0,\ 0,\ 0,\ 100,\ 10\,]^\mathsf{T}$
$\boldsymbol{x}_{s_a}(0)$	$[\,0,\ 150,\ 10,\ 0.1\,]^\mathsf{T}$
$\boldsymbol{x}_{s_1}(0)$	$[\,100,\ -150,\ 20,\ 0.2\,]^\mathsf{T}$
$\boldsymbol{x}_{s_2}(0)$	$[\,200,\ 200,\ 30,\ 0.3\,]^\mathsf{T}$
$\boldsymbol{x}_{s_3}(0)$	$[\,-150,\ 50,\ 40,\ 0.4\,]^\mathsf{T}$
$\hat{\boldsymbol{x}}_r(0\vert-1)$	$\sim \mathcal{N}\,[\,\boldsymbol{x}_r(0), \mathbf{P}_r(0\vert-1)\,]$
$\hat{\boldsymbol{x}}_{s_i}(0\vert-1)$	$\sim \mathcal{N}\,[\,\boldsymbol{x}_{s_i}(0), \mathbf{P}_{s_i}(0\vert-1)\,],\ \ i=1,2,3$
$\hat{\boldsymbol{x}}_{\mathrm{clk},s_a}(0\vert-1)$	$\sim \mathcal{N}\,[\,\boldsymbol{x}_{\mathrm{clk},s_a}(0), \mathbf{P}_{\mathrm{clk},s_a}(0\vert-1)\,]$
$\mathbf{P}_r(0\vert-1)$	$(10^4)\cdot\mathrm{diag}\,[\,1,1,10^{-2},10^{-2},1,10^{-2}\,]$
$\mathbf{P}_{s_i}(0\vert-1)$	$(10^3)\cdot\mathrm{diag}\,[\,1,1,1,10^{-1}\,],\ \ i=1,2,3$
$\mathbf{P}_{\mathrm{clk},s_a}(0\vert-1)$	$(10^3)\cdot\mathrm{diag}\,[\,1,10^{-1}\,]$
$h_{0,r}$	2×10^{-19}
$h_{-2,r}$	2×10^{-20}
h_{0,s_j}	$8\times10^{-20},\ \ j=1,\ldots,4$
h_{-2,s_j}	$4\times10^{-23},\ \ j=1,\ldots,4$
$\tilde{q}_x, \tilde{q}_y$	$0.1\,(\mathrm{m/s}^2)^2$
$\mathbf{R}$	$\mathrm{diag}\,[\,400,500,600,700\,]\,\mathrm{m}^2$
$v_{\max}$	$20\,\mathrm{m/s}$
$a_{\max}$	$5\,\mathrm{m/s}^2$
T	$0.1\,\mathrm{s}$

SOP_a. The remaining six trajectories were closed-loop according to Figure 4.1 with $\mathcal{J}\,[\boldsymbol{u}(k)]$ being D-optimality, A-optimality, E-optimality, MILD, MIT, and MIME. The optimal solutions of the information-based functionals were found by gridding the control feasibility region and performing an exhaustive-search, while the optimal solutions of the innovation-based functionals were found by searching over the extreme points of the feasibility region.

Figure 4.4 illustrates the eight receiver trajectories for a single simu-

lation run with the same initial estimates and process and observation noise time histories.

To compare the performance of the eight trajectories, the root mean squared estimation error (RMSEE) criterion was chosen [58]. The position, velocity, clock bias, and clock drift RMSEE over N MC runs are respectively defined as

$$\begin{aligned}
\text{RMSEE}[\boldsymbol{r}(k)] &\triangleq \sqrt{\frac{1}{N}\sum_{i=1}^{N} \tilde{x}_i^2(k|k) + \tilde{y}_i^2(k|k)} \\
\text{RMSEE}[\dot{\boldsymbol{r}}(k)] &\triangleq \sqrt{\frac{1}{N}\sum_{i=1}^{N} \tilde{\dot{x}}_i^2(k|k) + \tilde{\dot{y}}_i^2(k|k)} \\
\text{RMSEE}[\delta t(k)] &\triangleq \sqrt{\frac{1}{N}\sum_{i=1}^{N} \tilde{\delta t}_i^{\,2}(k|k)} \\
\text{RMSEE}[\dot{\delta t}(k)] &\triangleq \sqrt{\frac{1}{N}\sum_{i=1}^{N} \tilde{\dot{\delta t}}_i^2(k|k)}.
\end{aligned}$$

Figures 4.5-4.11 show the RMSEE for 100 MC runs for the receiver and SOP_1, while Figures 4.12-4.18 show the total RMSEE over the simulation horizon (50 seconds). Similar RMSEE and total RMSEE results were reported for SOP_2 and SOP_3.

The following conclusions can be drawn from these results. First, optimization-based motion planning yielded superior results to open-loop trajectories, which highlights the need to optimize the receiver trajectory for optimal information gathering. Second, there was a consistent performance ordering of the optimization-based methods: D-optimality and MILD yielded

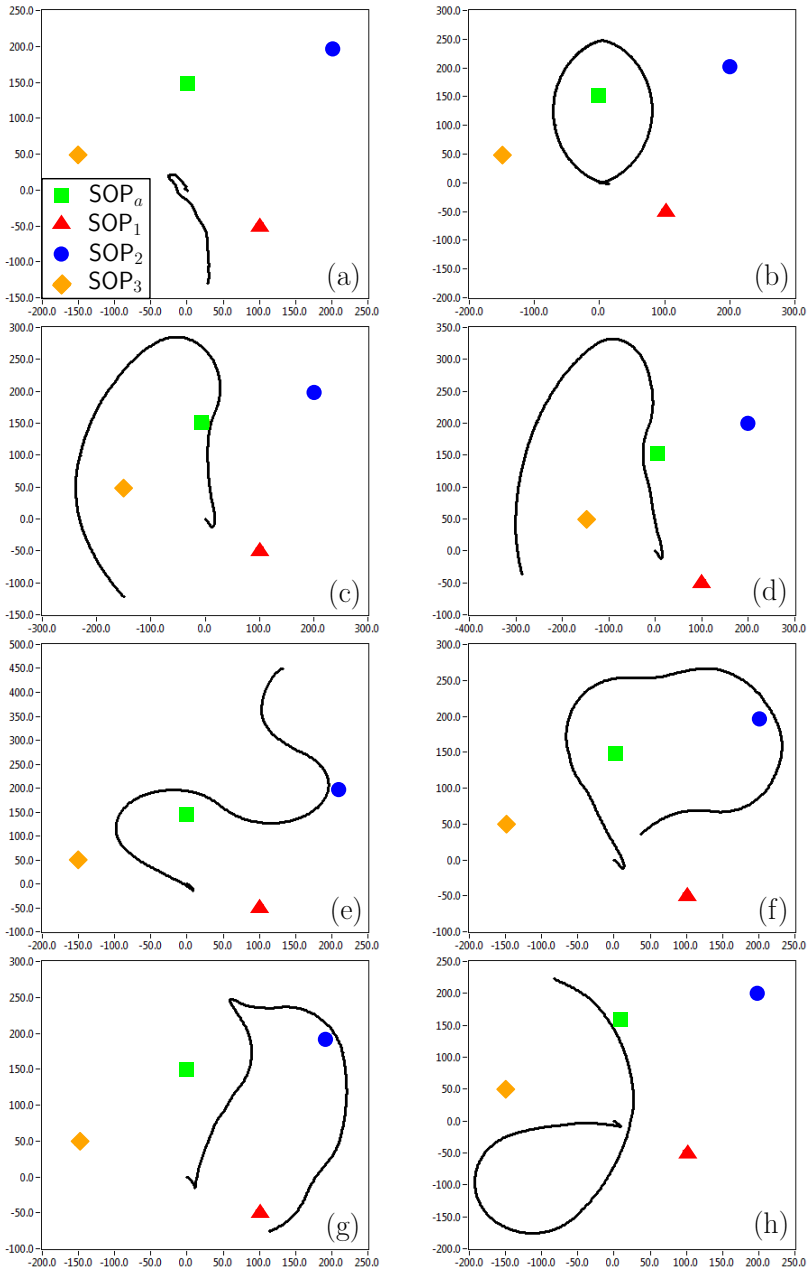

Figure 4.4: Receiver trajectories due to (a) random, (b) prescribed, (c) D-optimality, (d) MILD, (e) A-optimality, (f) MIT, (g) E-optimality, and (h) MIME motion planning strategies

the best results followed by A-optimality and MIT, while E-optimality and MIME yielded the worst results. Note that the only exception to this ordering was in the receiver and SOP clock drift RMSEE for A-optimality, E-optimality, MIT, and MIME. Nevertheless, the differences among these four methods for the clock drift states RMSEE were practically negligible. Third, while D-optimality and MILD were comparable, D-optimality was slightly superior, despite the fact that they were shown to be equivalent in Subsection 4.2.5. This can be explained by recalling that in deriving MILD a couple of approximations were invoked, namely dropping terms involving higher-order powers of T and approximating the matrix exponential via a Taylor Series expansion. Additionally, D-optimality and MILD equivalency was shown to hold for the Gaussian case, which does not necessarily hold here.

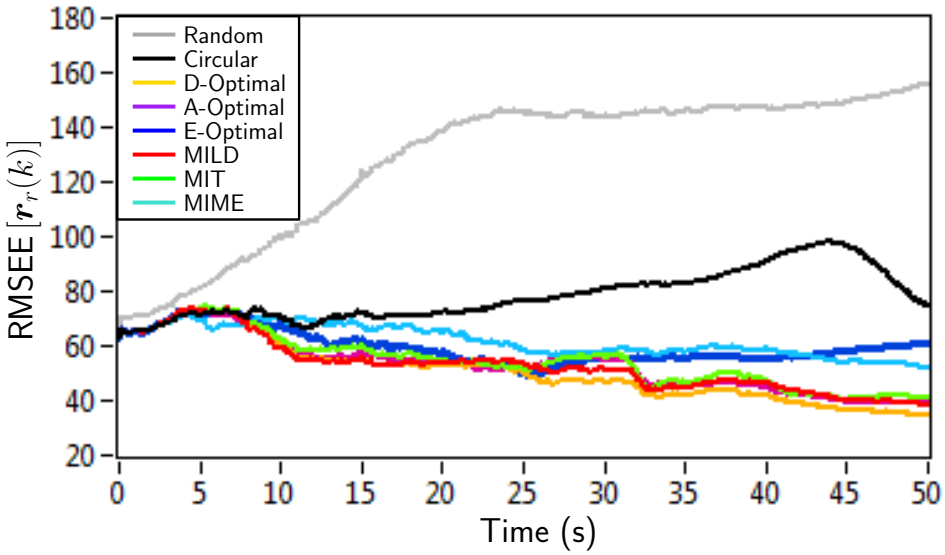

Figure 4.5: Receiver position RMSEE

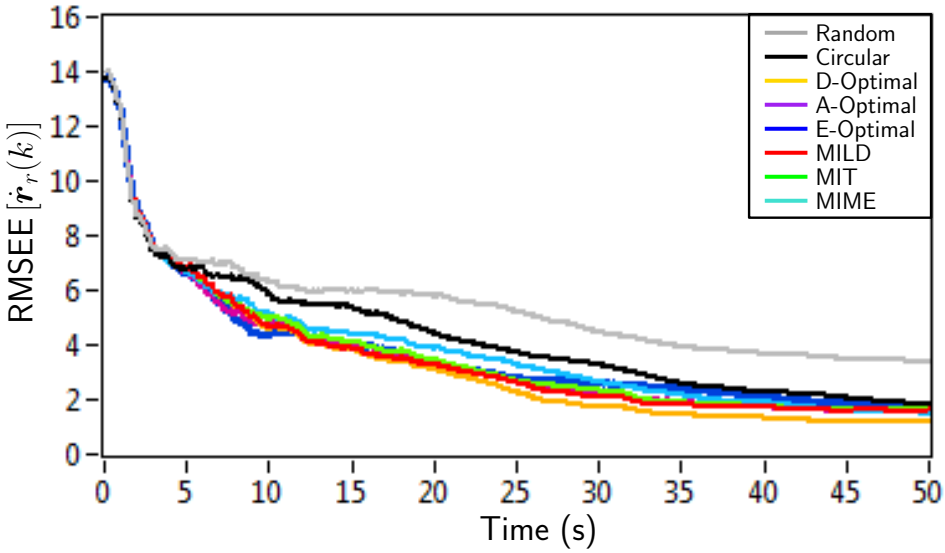

Figure 4.6: Receiver velocity RMSEE

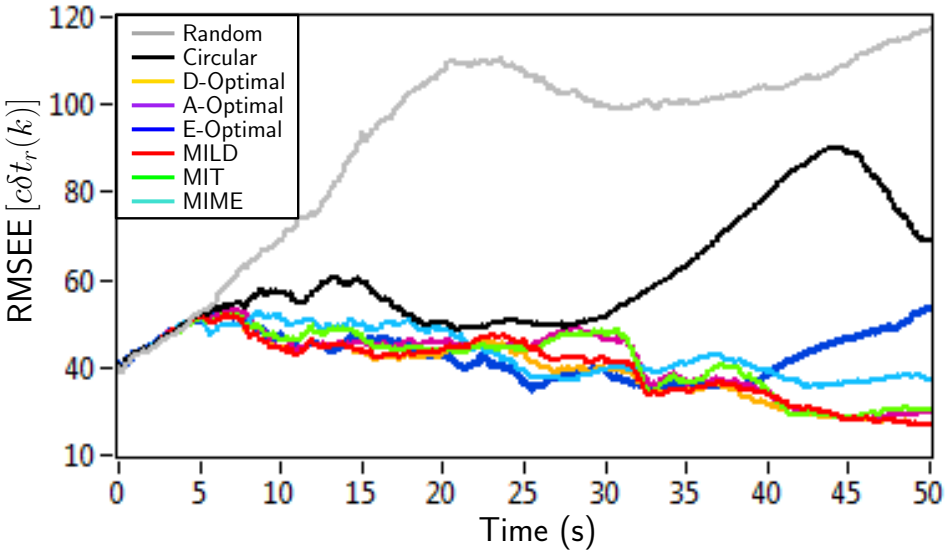

Figure 4.7: Receiver clock bias RMSEE

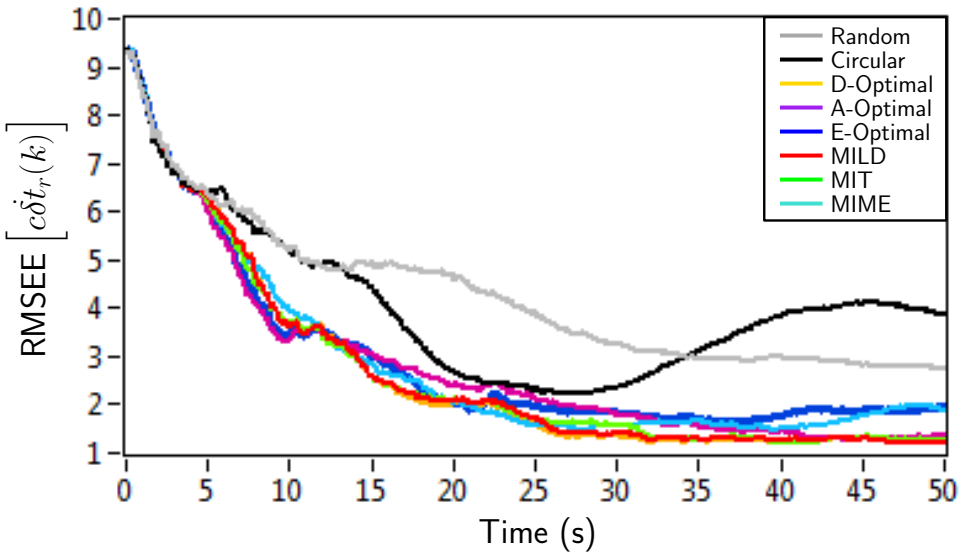

Figure 4.8: Receiver clock drift RMSEE

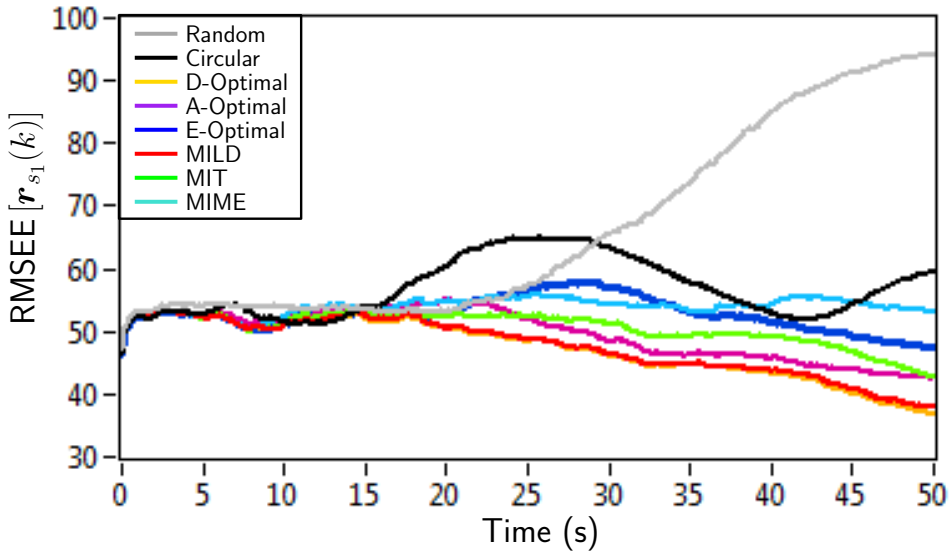

Figure 4.9: SOP_1 position RMSEE

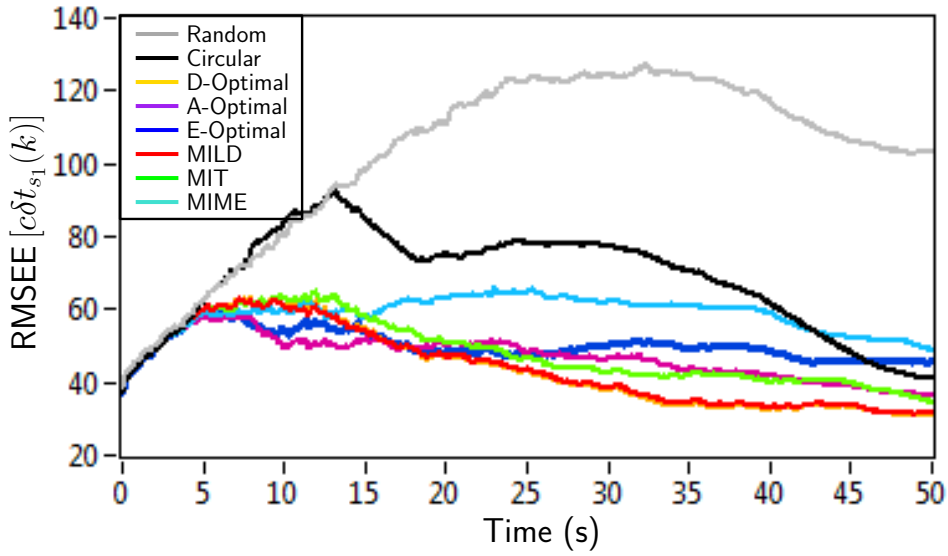

Figure 4.10: SOP_1 clock bias RMSEE

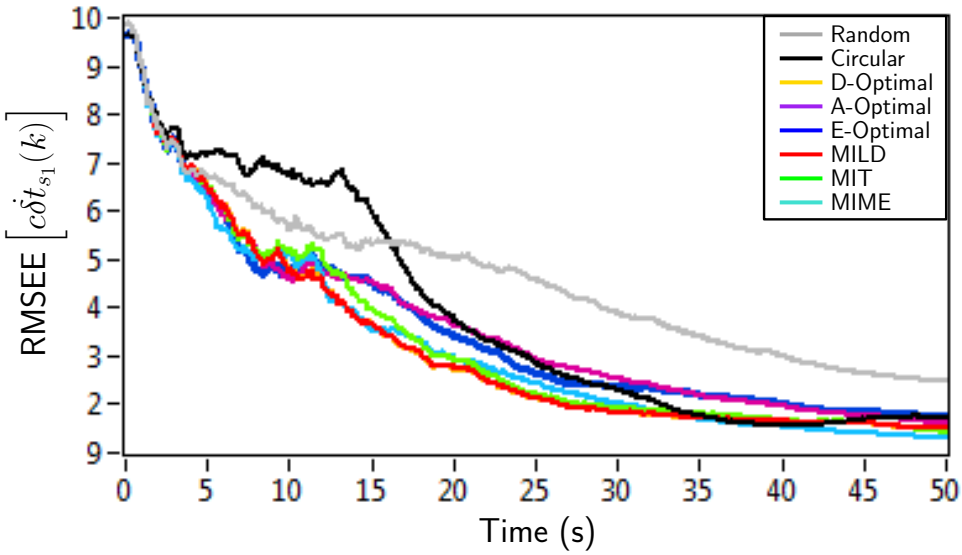

Figure 4.11: SOP_1 clock drift RMSEE

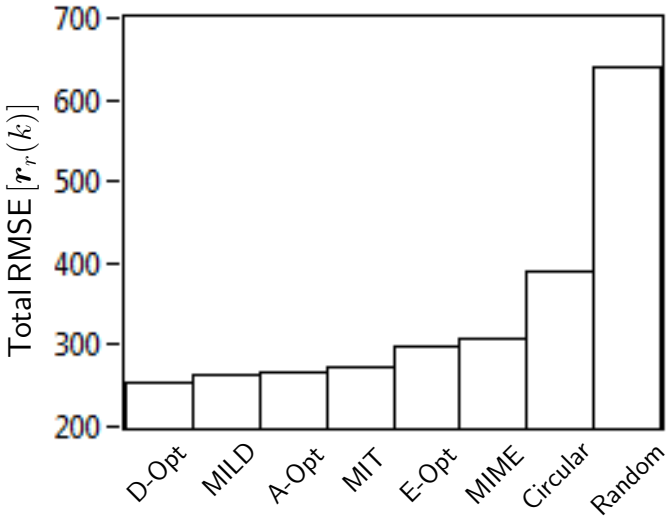

Figure 4.12: Receiver position total RMSEE

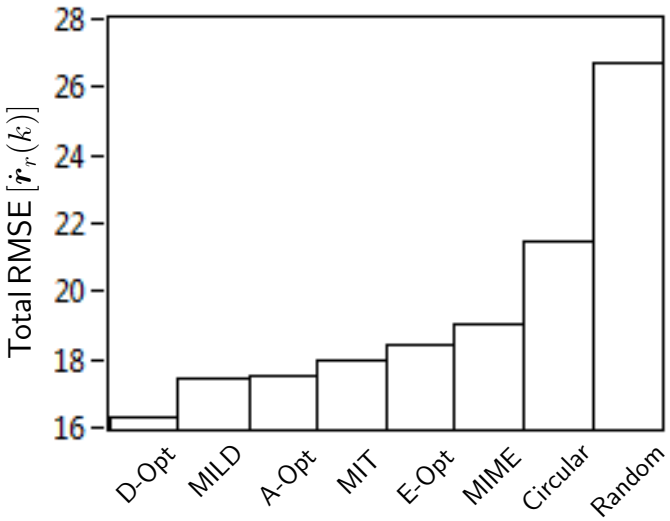

Figure 4.13: Receiver velocity total RMSEE

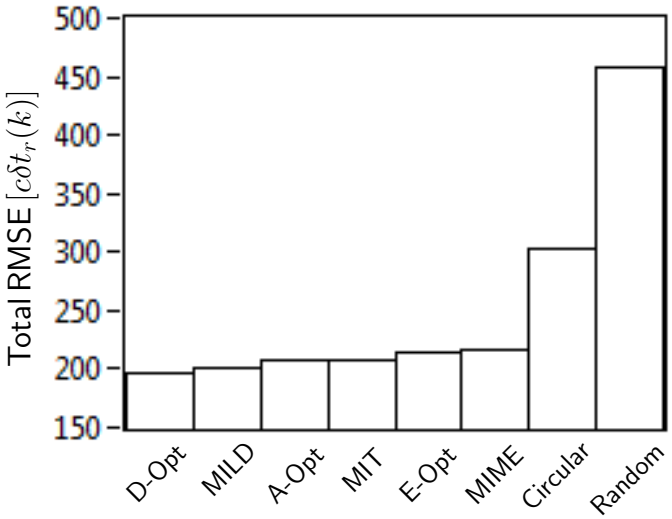

Figure 4.14: Receiver clock bias total RMSEE

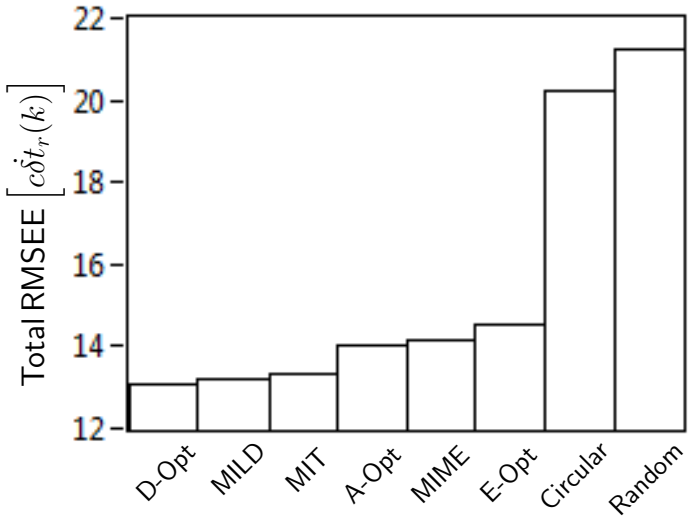

Figure 4.15: Receiver clock drift total RMSEE

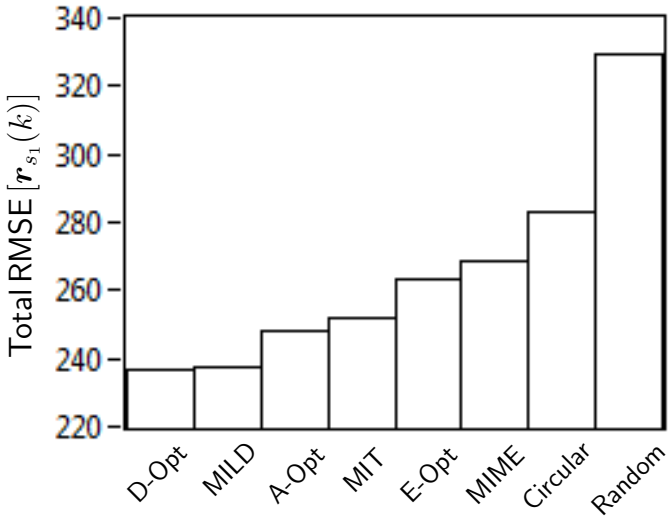

Figure 4.16: SOP_1 position total RMSEE

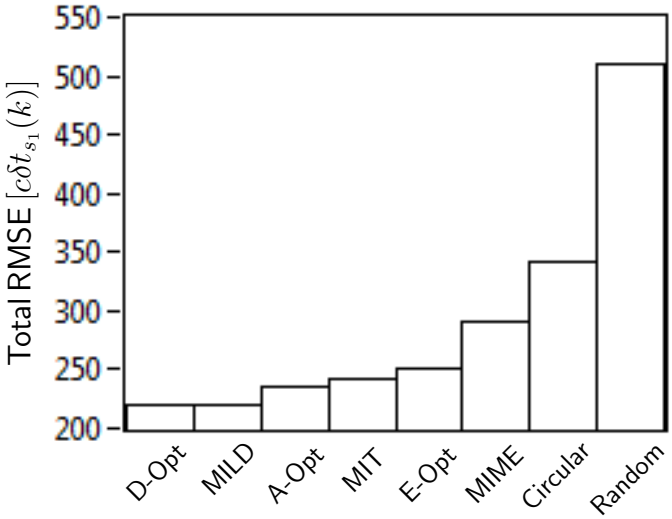

Figure 4.17: SOP_1 clock bias total RMSEE

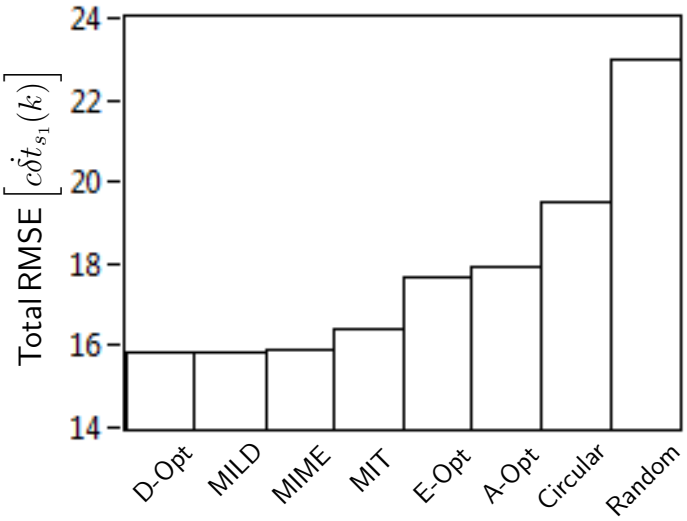

Figure 4.18: SOP_1 clock drift total RMSEE

4.3 Receding Horizon Trajectory Optimization

Multi-step look-ahead, also known as receding horizon, strategies are known to outperform greedy strategies for trajectory optimization [100–103]. In receding horizon trajectory optimization, at a particular time-step, a multi-step look-ahead optimal control sequence is computed. However, only the first step of this sequence is applied, whereas the rest of the sequence is discarded. This is motivated by the fact that at the next time-step, a new measurement becomes available, which contains information that is used to refine the optimal trajectory.

This section assesses the achieved improvements and associated limitations of a receding horizon strategy over a greedy strategy for the two observable modes of operation established in Section 3.6: (i) simultaneous receiver

localization and signal landscape mapping and (ii) signal landscape mapping. For the former case, the OpNav environment is assumed to comprise an unknown receiver with a state vector $\boldsymbol{x}_r$, a fully-known anchor SOP with a state vector $\boldsymbol{x}_{s_a}$, and m unknown SOPs with state vectors $\boldsymbol{x}_{s_1}, \ldots, \boldsymbol{x}_{s_m}$, whereas for the latter case the environment is assumed to comprise a fully-known receiver with a state vector $\boldsymbol{x}_r$ and m unknown SOPs with state vectors $\boldsymbol{x}_{s_1}, \ldots, \boldsymbol{x}_{s_m}$.

4.3.1 Receding Horizon Receiver Motion Planning Strategy

The proposed receding horizon trajectory optimization loop is illustrated in Figure 4.19. At a particular time-step k, the pseudorange observations $\boldsymbol{z}(k)$ made by the receiver on the SOPs in the environment are fused through an estimator– an EKF in this case. The observations take the form $\boldsymbol{z}(k) \triangleq [\, z_a(k), z_1(k), \ldots, z_m(k) \,]^{\mathsf{T}}$ and $\boldsymbol{z}(k) \triangleq [\, z_1(k), \ldots, z_m(k) \,]^{\mathsf{T}}$, respectively, for the two modes of operation defined above, and it is assumed that the observation noise elements are independent. Hence, the estimator's dynamics model is given by

$$\boldsymbol{x}\,(k+1) = \mathbf{F}\,\boldsymbol{x}\,(k) + \mathbf{G}\,\boldsymbol{u}\,(k) + \boldsymbol{w}(k),$$

where for the first observable case: $\boldsymbol{x} \triangleq \left[\, \boldsymbol{x}_r^{\mathsf{T}}, \boldsymbol{x}_{s_1}^{\mathsf{T}}, \ldots, \boldsymbol{x}_{s_m}^{\mathsf{T}} \,\right]^{\mathsf{T}}$ is the estimator's state vector, $\boldsymbol{u} \triangleq \boldsymbol{u}_r$ is the control vector, $\mathbf{F} = \mathrm{diag}\,[\, \mathbf{F}_r, \mathbf{F}_s, \ldots, \mathbf{F}_s \,]$, $\mathbf{G} = \left[\, \mathbf{G}_r^{\mathsf{T}}, \mathbf{0}_{2\times 4m} \,\right]^{\mathsf{T}}$, and $\boldsymbol{w} \triangleq [\, \boldsymbol{w}_r^{\mathsf{T}}, \boldsymbol{w}_{s_1}^{\mathsf{T}}, \ldots, \boldsymbol{w}_{s_m}^{\mathsf{T}} \,]^{\mathsf{T}}$ is a zero-mean process noise vector with covariance $\mathbf{Q} = \mathrm{diag}\,[\, \mathbf{Q}_r, \mathbf{Q}_{s_1}, \ldots, \mathbf{Q}_{s_m} \,]$, and the estimator's observation noise covariance is given by $\mathbf{R} = \mathrm{diag}\,[\, r_{s_a}, r_{s_1}, \ldots, r_{s_m} \,]$. For

the second observable case: $\boldsymbol{x} \triangleq \left[\, \boldsymbol{x}_{s_1}^{\mathsf{T}}, \ldots, \boldsymbol{x}_{s_m}^{\mathsf{T}} \,\right]^{\mathsf{T}}$ is the estimator's state vector, $\boldsymbol{u} \triangleq \mathbf{0}$ is the control vector, $\mathbf{F} = \operatorname{diag}\left[\, \mathbf{F}_s, \ldots, \mathbf{F}_s \,\right]$, $\mathbf{G} = \left[\, \mathbf{0}_{2\times 4m} \,\right]^{\mathsf{T}}$, and $\boldsymbol{w} \triangleq \left[\, \boldsymbol{w}_{s_1}^{\mathsf{T}}, \ldots, \boldsymbol{w}_{s_m}^{\mathsf{T}} \,\right]^{\mathsf{T}}$ is a zero-mean process noise vector with covariance $\mathbf{Q} = \operatorname{diag}\left[\, \mathbf{Q}_{s_1}, \ldots, \mathbf{Q}_{s_m} \,\right]$, and the estimator's observation noise covariance is given by $\mathbf{R} = \operatorname{diag}\left[\, r_{s_1}, \ldots, r_{s_m} \,\right]$.

The EKF produces a state estimate $\hat{\boldsymbol{x}}(k|k)$ and an associated estimation error covariance $\mathbf{P}(k|k)$. The estimate and associated covariance are fed into a receding horizon optimal control solver, which solves for the optimal admissible N-step look-ahead control actions $\boldsymbol{U}_k^N$, which are defined as $\left(\boldsymbol{U}_k^N\right)^\star \triangleq \{\boldsymbol{u}^\star(k+j),\, j=0,\ldots,N-1\}$ to minimize the D-optimality cost functional $\mathcal{J}$, subject to the OpNav dynamics and observation model Σ_{OpNav} along with velocity and acceleration constraints. Recall from Subsection 4.2.2 that the D-optimality criterion is proportional to the volume of the estimation error uncertainty ellipsoid and was demonstrated in Subsection 4.2.6 to be superior to the A- and E-optimality criteria in an RMSEE sense. In Figure 4.19, $v_{r,\max}$ and $a_{r,\max}$ represent the maximum speed and acceleration, respectively, with which the receiver can move.

Note that if $N = 1$, the receding horizon trajectory optimization problem reduces to greedy optimization. To evaluate the N-step estimation error covariance, $\mathbf{P}(k+N|k+N)$, the zero future innovations assumption, namely $\tilde{\boldsymbol{z}}(j+1) \triangleq \boldsymbol{z}(j+1) - \boldsymbol{h}\left[\hat{\boldsymbol{x}}(j+1|j)\right] \equiv 0$, for $j = k, \ldots, k+N-1$, will be invoked [101]. Once the optimal N-step look-ahead control actions $\left(\boldsymbol{U}_k^N\right)^\star$ are found, only the first control action $\boldsymbol{u}^\star(k)$ is applied, whereas the rest of the

control actions $\{\boldsymbol{u}^\star(j)\}_{j=k+1}^{k+N-1}$ are discarded. A single iteration of the algorithm for finding the receding horizon optimal receiver trajectory is outlined in Algorithm 1.

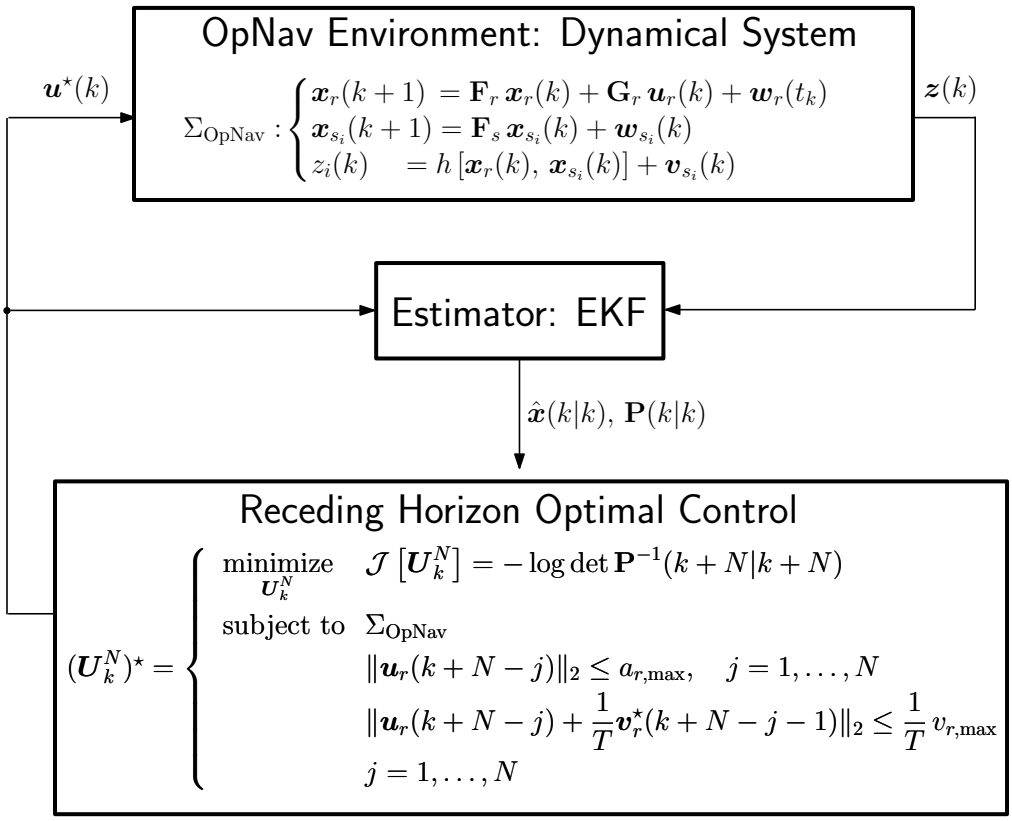

Figure 4.19: Receding horizon receiver motion planning loop. For the first observable mode of operation: $i = a, 1, \ldots, m$, and for the second observable mode of operation: $i = 1, \ldots, m$.

One drawback of receding horizon trajectory optimization is repeated invoking of the zero-innovation assumption. Another drawback is increased computational burden. Figure 4.20 illustrates the cascade of feasibility regions that should be considered as the horizon is increased. In particular,

each point in the black shaded region corresponding to the feasibility region of the first-step look-ahead has an associated feasibility region of its own signifying the feasible maneuvers the receiver could take for the second-step. The number of optimization variables for an N-step look-ahead problem are $2N$. Denoting the number of feasible maneuvers in a particular time-step j by n_j, it is easy to see that an exhaustive search-type algorithm has a computational burden $\mathcal{O}\left(\prod_{j=1}^{N} n_j\right)$.

Algorithm 1 Receding horizon trajectory optimization

Given: $\hat{\boldsymbol{x}}(k|k)$, $\mathbf{P}(k|k)$, N
for $j = k, \ldots, k+N-1$ **find**
$\hat{\boldsymbol{x}}(j+1|j) = \mathbf{F}\hat{\boldsymbol{x}}(j|j) + \mathbf{G}\boldsymbol{u}(j)$
$\mathbf{H}(j+1) = \left.\frac{\partial \boldsymbol{h}[\boldsymbol{x}_r(j+1), \boldsymbol{x}_s(j+1)]}{\partial \boldsymbol{x}}\right|_{\boldsymbol{x}=\hat{\boldsymbol{x}}(j+1|j)}$
$\mathbf{P}(j+1|j) = \mathbf{F}\mathbf{P}(j|j)\mathbf{F}^{\mathsf{T}} + \mathbf{Q}$
$\mathbf{S}(j+1) = \mathbf{H}(j+1)\mathbf{P}(j+1|j)\mathbf{H}^{\mathsf{T}}(j+1) + \mathbf{R}$
$\mathbf{W}(j+1) = \mathbf{P}(j+1|j)\mathbf{H}^{\mathsf{T}}(j+1)\mathbf{S}^{-1}(j+1)$
$\mathbf{P}(j+1|j+1) = \mathbf{P}(j+1|j) - \mathbf{W}(j+1)\mathbf{S}(j+1)\mathbf{W}^{\mathsf{T}}(j+1)$
$\hat{\boldsymbol{x}}(j+1|j+1) \equiv \hat{\boldsymbol{x}}(j+1|j)$
end for
Solve:

$$\underset{\boldsymbol{U}_{t_k}^{N}}{\text{minimize}} \quad \mathcal{J}\left[\boldsymbol{U}_k^N\right] = -\log\det\mathbf{P}^{-1}(k+N|k+N)$$

$$\text{subject to} \quad \Sigma_{\text{OpNav}}$$
$$\|\boldsymbol{u}_r(k+N-j)\|_2 \leq a_{r,\max}, \quad j = 1, \ldots, N$$
$$\left\|\boldsymbol{u}_r(k+N-j) + \frac{\boldsymbol{v}_r^{\star}(k+N-j-1)}{T}\right\|_2 \leq \frac{v_{r,\max}}{T},$$
$$j = 1, \ldots, N$$

Apply: $\boldsymbol{u}^{\star}(k)$
Discard: $\{\boldsymbol{u}^{\star}(k+1), \ldots, \boldsymbol{u}^{\star}(k+N-1)\}$

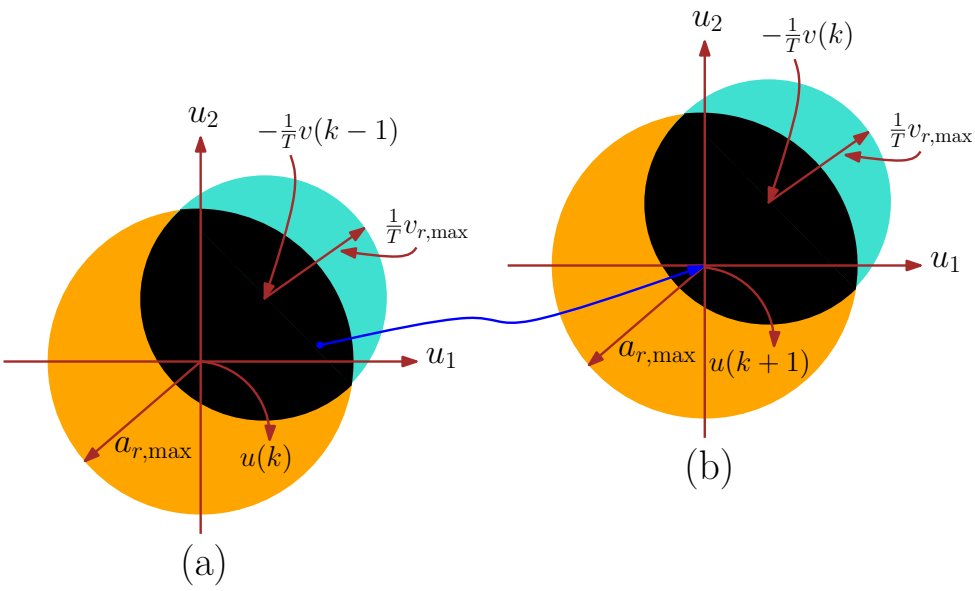

Figure 4.20: Cascade of feasibility regions for two-step look-ahead horizon. The two disks in (a) represent the acceleration and velocity constraints for the firs-step look-ahead. The disks intersection (black shaded area) are the receiver feasible maneuvers. Each point in this feasibility region is associated with another feasibility region in (b) representing the feasible maneuvers for the second-step look-ahead.

4.3.2 Simulation Results

This subsection presents simulation results to demonstrate the limitations and effectiveness of receding horizon trajectory optimization versus greedy [85, 86]. An OpNav environment comprising a receiver and four SOPs, labeled $\{\text{SOP}_i\}_{i=1}^{4}$, was simulated according to the settings presented in Table 4.2. The receiver's and SOPs' clocks were assumed to be TCXO and OCXOs, respectively. For purposes of numerical stability, the clock error states were defined to be $c\delta t$ and $c\dot{\delta t}$. Two receiver modes of operation were considered, corresponding to the two observability conditions established in Section 3.6:

(i) simultaneous receiver localization and signal landscape mapping in an environment with one fully-known "anchor" SOP and three unknown SOPs, and (ii) signal landscape mapping in an environment with four unknown SOPs and a fully-known receiver.

Table 4.2: Receding horizon trajectory optimization simulation settings

Parameter	**Value**
$\boldsymbol{x}_{s_1}(0)$	$[\,0,\ 150,\ 10,\ 0.1\,]^\mathsf{T}$
$\boldsymbol{x}_{s_2}(0)$	$[\,100,\ -150,\ 20,\ 0.2\,]^\mathsf{T}$
$\boldsymbol{x}_{s_3}(0)$	$[\,200,\ 200,\ 30,\ 0.3\,]^\mathsf{T}$
$\boldsymbol{x}_{s_4}(0)$	$[\,-150,\ 50,\ 40,\ 0.4\,]^\mathsf{T}$
$h_{0,r}$	2×10^{-19}
$h_{-2,r}$	2×10^{-20}
h_{0,s_j}	$8 \times 10^{-20},\ \ j = 1, \ldots, 4$
h_{-2,s_j}	$4 \times 10^{-23},\ \ j = 1, \ldots, 4$
$\tilde{q}_x, \tilde{q}_y$	$0.1\,(\mathrm{m/s^2})^2$
r	$\{\,250,\ 300,\ 350\,\}\ \mathrm{m}^2$
$v_{\max}$	$10\,\mathrm{m/s}$
$a_{\max}$	$3\,\mathrm{m/s}^2$
T	$0.2\,\mathrm{s}$

Three sets of simulations were performed for three different observation noise intensities r. Four receiver trajectories per noise intensity were generated: a random trajectory, a greedy trajectory, and two receding horizon trajectories with $N = 2$ and $N = 3$. For meaningful comparison, the same initial state estimates and process and observation noise realization time histories were used to generate the four receiver trajectories. Several MC-based runs were conducted for each noise intensity with randomized initial state estimates and noise realization time histories.

4.3.2.1 Case 1: Simultaneous Receiver Localization and Signal Landscape Mapping with One Known Anchor SOP

The receiver was assumed to have the initial state $\boldsymbol{x}_r(0) = [\,0,\,0,\,10,\,0,\,100,\,10\,]^{\mathsf{T}}$ and the known anchor SOP was assumed to be SOP_1. The initial estimates for the receiver and the three SOPs were generated according to $\hat{\boldsymbol{x}}_r(0|-1) \sim \mathcal{N}\left[\boldsymbol{x}_r(0), \mathbf{P}_r(0|-1)\right]$ and $\hat{\boldsymbol{x}}_{s_i}(0|-1) \sim \mathcal{N}\left[\boldsymbol{x}_{s_i}(0), \mathbf{P}_{s_i}(0|-1)\right]$, $i = 2, 3, 4$, with initial estimation error covariance matrices $\mathbf{P}_r(0|-1) = (10^4) \cdot \mathrm{diag}\,[\,1,\,1,\,1,\,1,\,1, 10^{-2}\,]$ and $\mathbf{P}_{s_i}(0|-1) = (10^4) \cdot \mathrm{diag}\,[\,1,\,1,\,1, 10^{-2}\,]$. To assess the localization accuracy and signal landscape map quality, the natural logarithm of the posterior estimation error covariance determinant, namely $\log\det\left[\mathbf{P}(k+1|k+1)\right]$, was adopted.

The resulting receiver trajectories for $r = 250\,\mathrm{m}^2$ and a particular run are illustrated in Figure 4.21. The resulting localization and signal landscape map uncertainties for $r \in \{\,250,\,300,\,350\,\}\ \mathrm{m}^2$ and the same run are plotted in Figure 4.22-4.24. The $\log\det\left[\mathbf{P}^{\star}(k+1|k+1)\right]$ plots exhibited a similar behavior for various MC runs. The reduction in receiver localization and signal landscape map estimation uncertainty for the receding horizon approaches over the greedy approach at the end of the simulation time is averaged over ten MC runs and is tabulated in Table 4.3.

Table 4.3: Average % reduction in receiver localization and signal landscape map estimation uncertainty for receding horizon over greedy

N	$r = 250$	$r = 300$	$r = 350$
2	14.19	7.51	-8.03
3	29.63	20.95	6.28

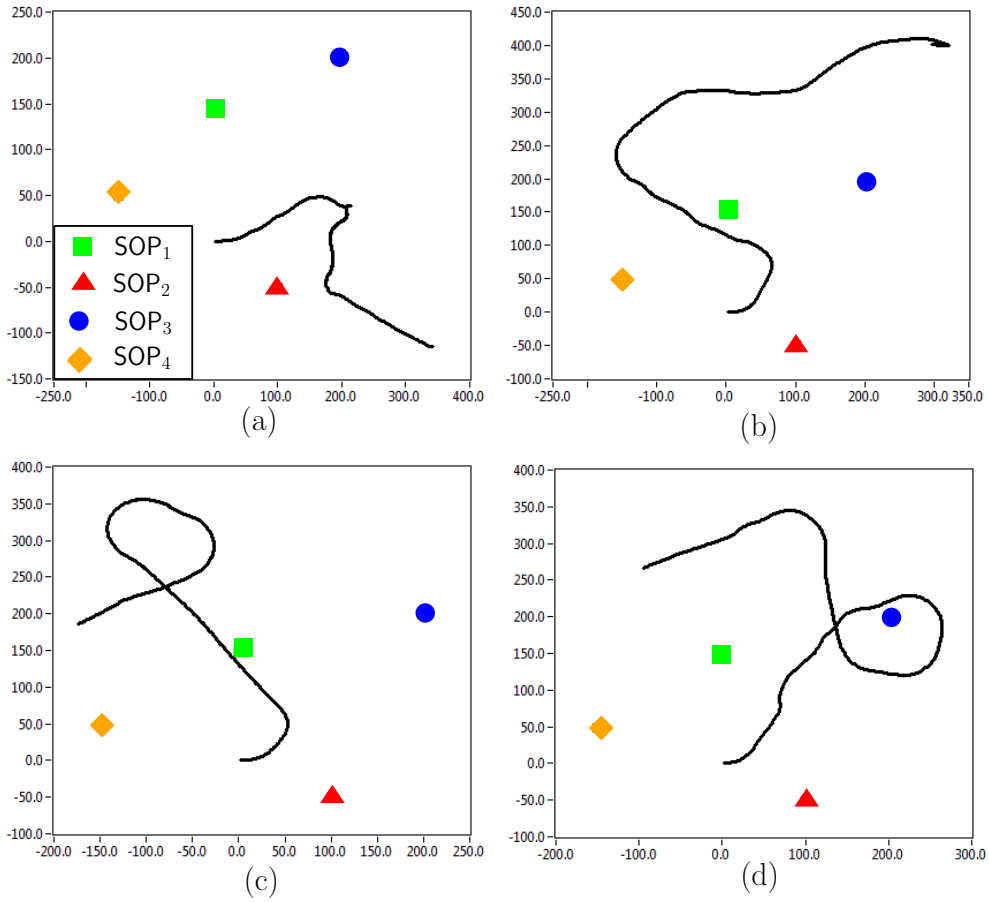

Figure 4.21: Case 1: receiver trajectories due to (a) random, (b) optimal greedy, (c) optimal two-step look-ahead, and (d) optimal three-step look-ahead

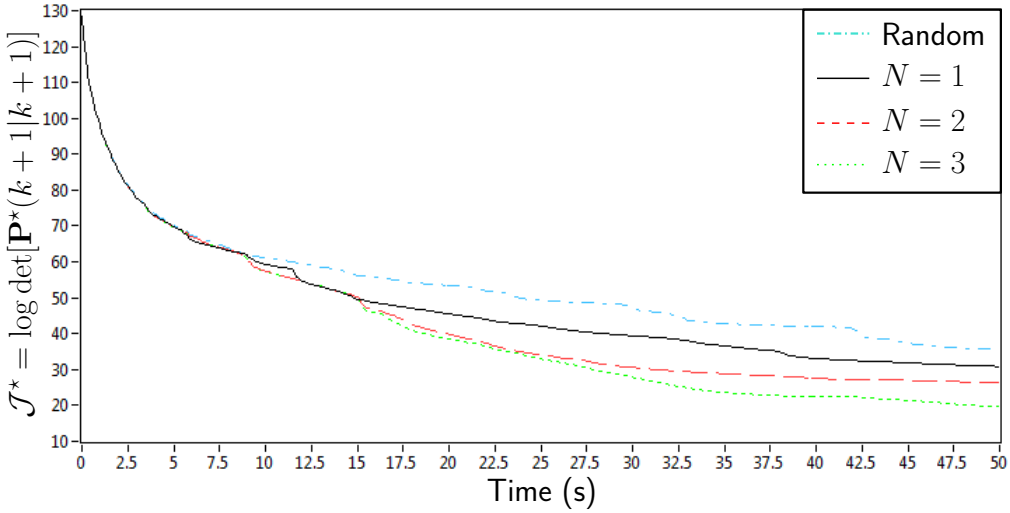

Figure 4.22: Localization & signal landscape map uncertainty for $r = 250\,\mathrm{m}^2$

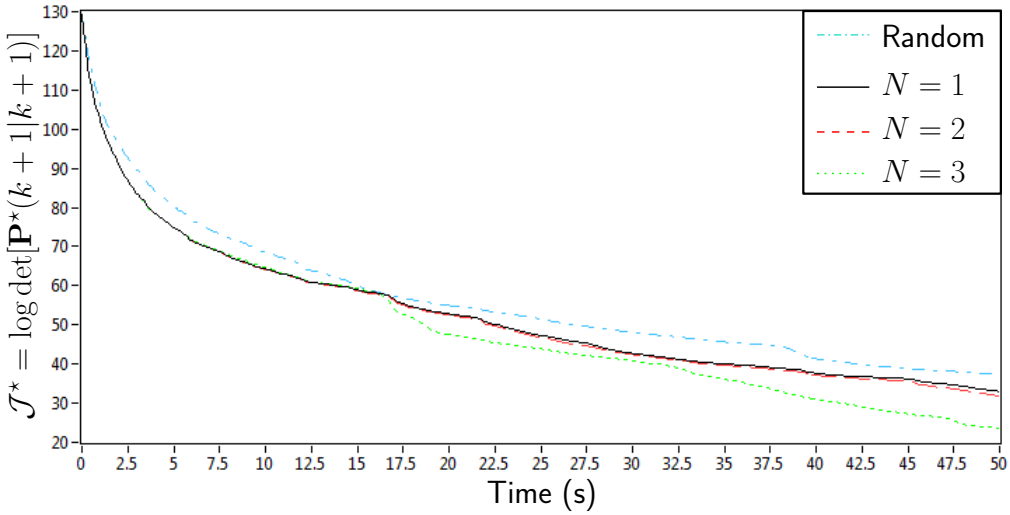

Figure 4.23: Localization & signal landscape map uncertainty for $r = 300\,\mathrm{m}^2$

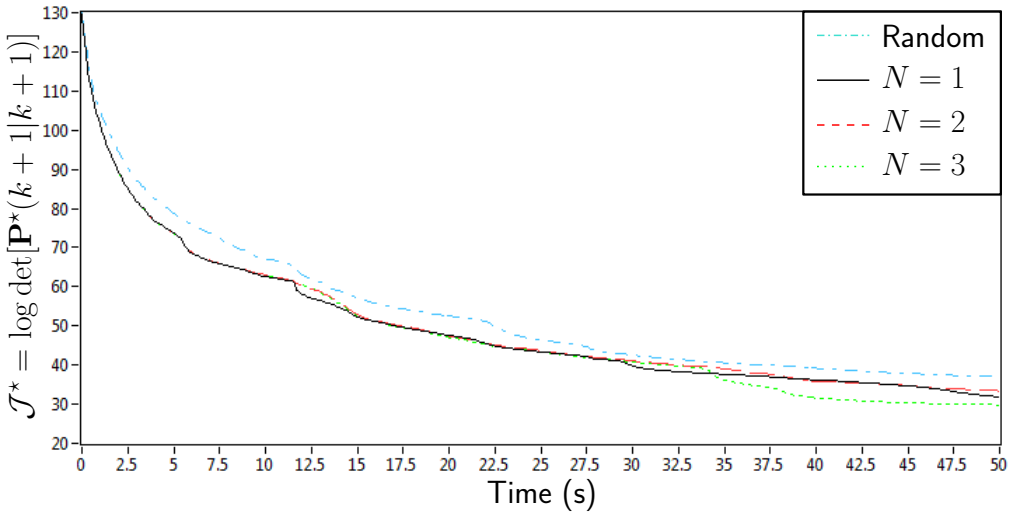

Figure 4.24: Localization & signal landscape map uncertainty for $r = 350\,\mathrm{m}^2$

4.3.2.2 Case 2: Signal Landscape Mapping with a Known Receiver

The receiver was assumed to have an initial known state of $\boldsymbol{x}_r(0) = [\,0,\,0,\,0,\,0,\,100,\,10\,]^\mathsf{T}$. The initial estimates for the the four SOPs were generated according to $\hat{\boldsymbol{x}}_{s_i}(0|-1) \sim \mathcal{N}\left[\boldsymbol{x}_{s_i}(0), \mathbf{P}_{s_i}(0|-1)\right]$, $i = 1, \ldots, 4$, with initial estimation error covariance matrices $\mathbf{P}_{s_i}(0|-1) = (10^4)\cdot\mathrm{diag}\,[\,1, 1, 1, 10^{-2}\,]$. To assess the signal landscape map, quality $\log\det\left[\mathbf{P}(k+1|k+1)\right]$ was adopted.

The resulting receiver trajectories for $r = 250\,\mathrm{m}^2$ and a particular run are illustrated in Figure 4.25. The resulting signal landscape map uncertainty for $r \in \{\,250,\,300,\,350\,\}\ \mathrm{m}^2$ and the same run are plotted in Figure 4.26-4.28. The $\log\det\left[\mathbf{P}^\star(k+1|k+1)\right]$ plots exhibited a similar behavior for various MC runs. The reduction in signal landscape map estimation uncertainty for the receding horizon approaches over the greedy approach at the end of the simulation time is averaged over ten MC runs and is tabulated in Table 4.4.

Table 4.4: Average % reduction in signal landscape map estimation uncertainty for receding horizon over greedy

N	$r = 250$	$r = 300$	$r = 350$
2	94.69	55.56	43.61
3	135.51	78.46	52.63

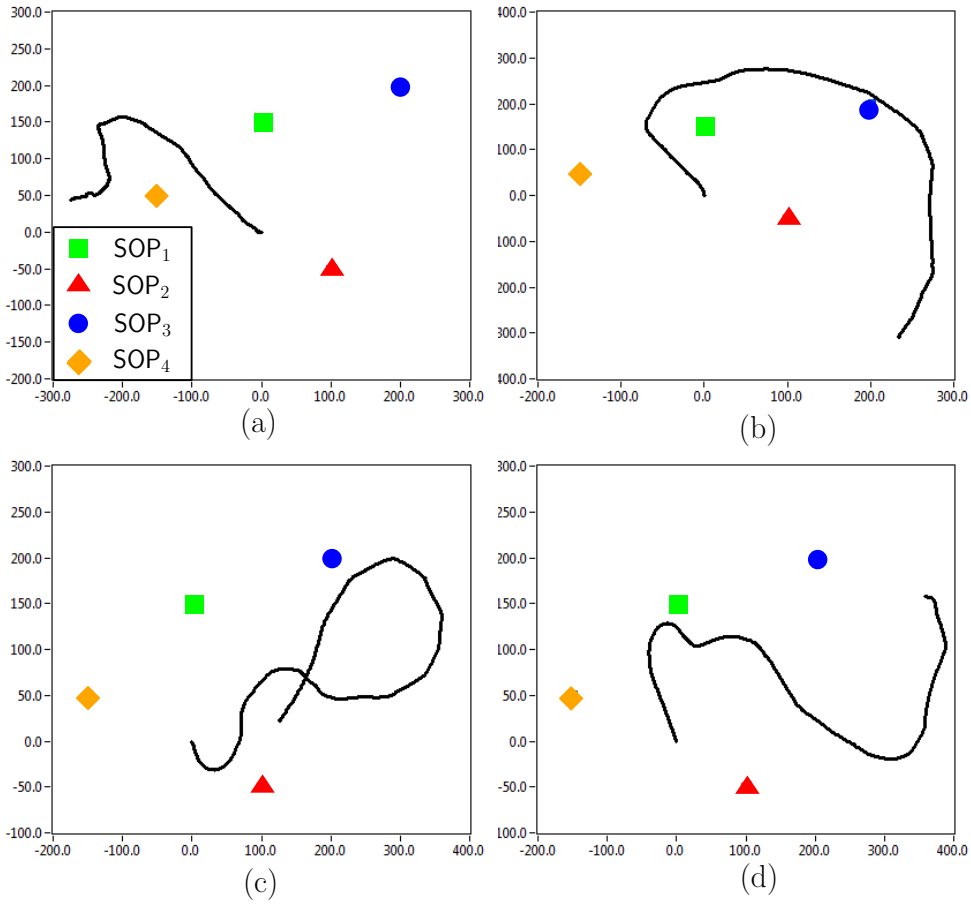

Figure 4.25: Case 2: receiver trajectories due to (a) random, (b) optimal greedy, (c) optimal two-step look-ahead, and (d) optimal three-step look-ahead

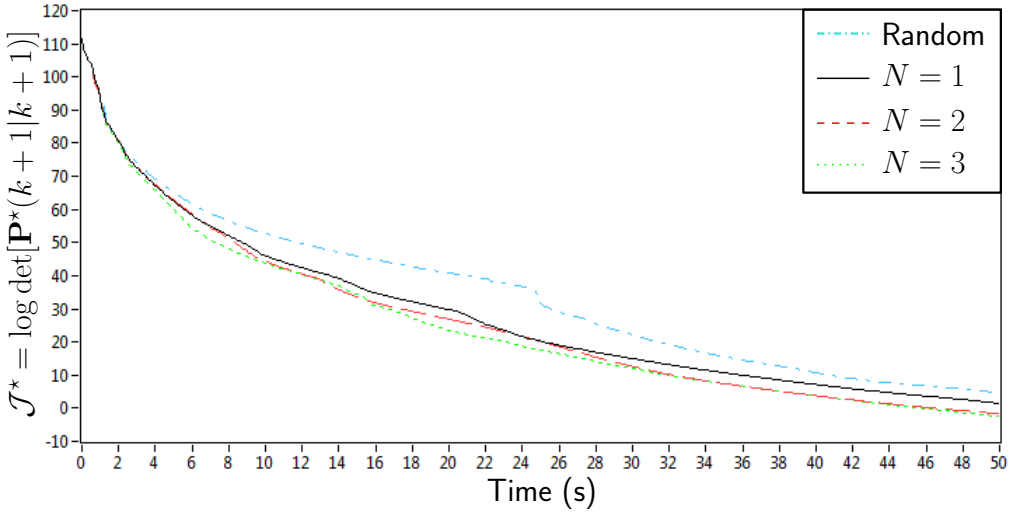

Figure 4.26: Signal landscape map uncertainty for $r = 250\,\mathrm{m}^2$

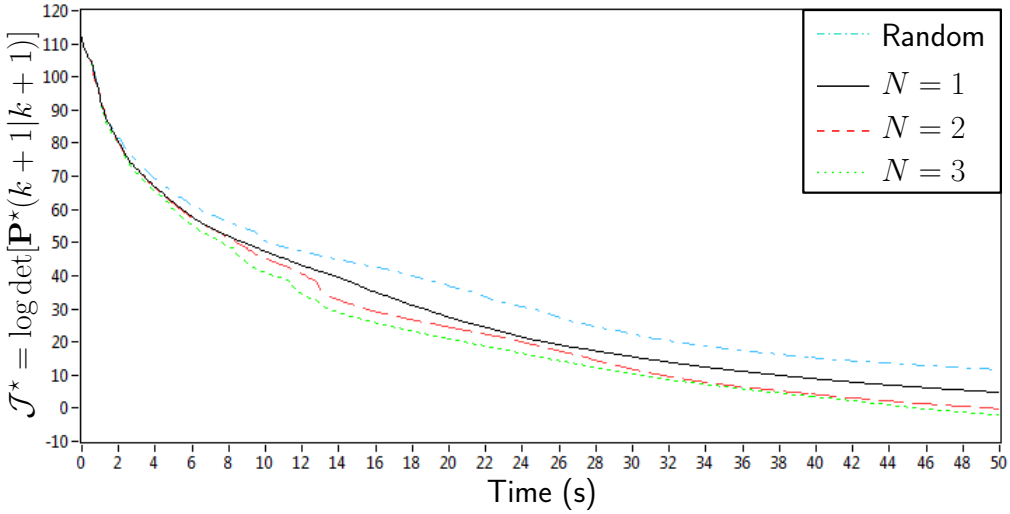

Figure 4.27: Signal landscape map uncertainty for $r = 300\,\mathrm{m}^2$

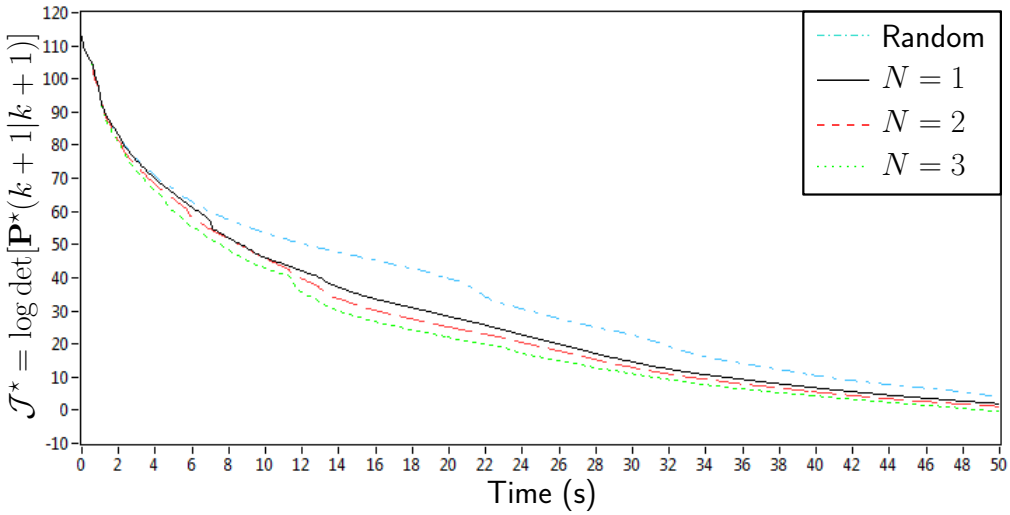

Figure 4.28: Signal landscape map uncertainty for $r = 350\,\mathrm{m}^2$

4.3.2.3 Simulation Results Discussion

The following conclusions can be drawn from the presented simulations. First, greedy motion planning and receding horizon trajectory optimization yielded superior results to random trajectories. Second, receding horizon trajectory optimization outperformed greedy motion planning. Third, the superiority of receding horizon over greedy motion planning depends on the observation noise intensity– the larger the observation noise, the less advantage the receding horizon strategy has. In fact, for large enough observation noise, receding horizon yields nearly identical (or slightly worse) performance than greedy. Fourth, for the same simulation settings, the improvements gained from receding horizon over greedy were more significant whenever the receiver had *a priori* knowledge about its own state and was tasked with signal landscape mapping, over the case where the receiver had no *a priori* knowledge

about its state and was tasked with simultaneous receiver localization and signal landscape mapping.

4.4 Collaborative Signal Landscape Mapping

This section studies the problem of collaborative signal landscape mapping of multiple unknown SOPs through multiple receivers. In accordance with the observability condition established in Section 3.6, it is assumed that one receiver has full knowledge of its initial state vector.

4.4.1 Price of Anarchy

The collaborative signal landscape mapping problem is a coupled decision making under uncertainty and information fusion problem, to which various architectures can be synthesized. To assess the performance of the various architectures that will be synthesized, the game-theoretic notion of price of anarchy (PoA) will be adopted, which is defined next [118].

Definition 4.4.1. The PoA quantifies the degradation of solution quality as a centralized system moves to a more decentralized framework. Mathematically,

$$\text{PoA} \triangleq \frac{\max\limits_{s_i} \mathcal{J}_{s_i}^{\star\star}}{\mathcal{J}^{\star}},$$

where $\mathcal{J}^{\star}$ is the optimal centralized cost and $\mathcal{J}_{s_i}^{\star\star}$ is the cost of the ith agent due to some decentralized strategy s.

Note that in calculating the PoA, one takes the worst case (maximum) cost over different agents in the environment, since the PoA assesses the overall

performance of the system due to a proposed decentralized strategy s versus a centralized one. Also, note that PoA ≥ 1, and the closer the PoA is to one, the more comparable the proposed decentralized strategy s is to an optimal centralized strategy.

4.4.2 Main Building Blocks

The collaborative signal landscape mapping architectures are composed of four main building blocks: (*i*) radio frequency (RF) front-end (FE) processing and tracking loops (TL), (*ii*) extended information filter (EIF), (*iii*) optimal greedy control (OGC) solver, and (*iv*) actuators. These building blocks are described next.

4.4.2.1 RF FE Processing and TL

This block digitizes and downsamples the RF analog stream received by the antenna [119–121]. Subsequently, the SOP signal is acquired and tracked to produce the pseudorange observable described in Section 2.2 [122].

4.4.2.2 Extended Information Filter

This block takes the pseudorange observables $\{z_i(k)\}_{i=1}^{m}$, where m is the number of SOPs, and filters them to produce an estimate $\hat{\boldsymbol{x}}(k|k)$ and an associated estimation error covariance $\mathbf{P}(k|k)$. This block is also utilized to fuse filtered estimates from different receivers.

For optimal fusion, the estimation scheme adopted to fuse estimates

and associated estimation error covariances from multiple receivers making observations on the same SOPs cannot be formulated in the standard KF formulation. This is due to the fact that while the innovations are temporally uncorrelated, the innovations generated from different receivers are correlated by virtue of the fact that they use a common prediction [106]. Suboptimal algorithms for fusing estimates and their corresponding auto-covariances, where the cross-correlation between the vectors is unknown exist, such as the covariance intersection algorithm [123]. However, by expressing the estimation problem in the information space instead of the state space, optimal fusion can be derived leading to the EIF [106, 124], a special case of which is summarized next.

Consider the linear dynamics and nonlinear observations

$$\boldsymbol{x}(k+1) = \mathbf{F}\,\boldsymbol{x}(k) + \mathbf{G}\,\boldsymbol{u}(k) + \boldsymbol{w}(k)$$
$$\boldsymbol{z}(k) = \boldsymbol{h}\,[\boldsymbol{x}(k)] + \boldsymbol{v}(k)$$

where $\boldsymbol{x} \in \mathbb{R}^n$, $\boldsymbol{u} \in \mathbb{R}^r$, $\boldsymbol{w} \in \mathbb{R}^n$, $\boldsymbol{z} \in \mathbb{R}^m$, $\boldsymbol{v} \in \mathbb{R}^m$ are the system state, input, process noise, observation, and observation noise vectors, respectively. Assume $\boldsymbol{w}$ and $\boldsymbol{v}$ to be zero-mean, mutually-uncorrelated, white noise sequences with covariance matrices $\mathbf{Q}$ and $\mathbf{R}$, respectively.

Assume the initial knowledge about the system state to be captured in the state estimate $\hat{\boldsymbol{x}}(0|0)$ and associated estimation error covariance $\mathbf{P}(0|0)$. The EIF maintains the information state vector and information matrix, defined as $\hat{\boldsymbol{y}}(i|j) \triangleq \mathbf{Y}(i|j)\hat{\boldsymbol{x}}(i|j)$ and $\mathbf{Y}(i|j) \triangleq \mathbf{P}^{-1}(i|j)$, respectively, where

$\hat{\boldsymbol{x}}(i|j)$ and $\mathbf{P}(i|j)$ are the state vector estimate and associated estimation error covariance at time i given all the observations up to and including time j. The EIF recursive prediction and correction equations are given by

Prediction

$$\begin{aligned}\hat{\boldsymbol{y}}(k+1|k) &= \mathbf{Y}(k+1|k)\left[\mathbf{F}\,\hat{\boldsymbol{x}}(k|k)+\mathbf{G}\,\boldsymbol{u}(k)\right]\\ \mathbf{Y}(k+1|k) &= \left[\mathbf{F}\,\mathbf{Y}^{-1}(k|k)\,\mathbf{F}^{\mathsf{T}}+\mathbf{Q}\right]^{-1}\end{aligned}$$

Correction

$$\begin{aligned}\hat{\boldsymbol{y}}(k+1|k+1) &= \hat{\boldsymbol{y}}(k+1|k)+\boldsymbol{i}(k+1)\\ \mathbf{Y}(k+1|k+1) &= \mathbf{Y}(k+1|k)+\mathbf{I}(k+1),\end{aligned}$$

where $\boldsymbol{i}(k+1)$ and $\mathbf{I}(k+1)$ denote the information state contribution and its corresponding information matrix, respectively, associated with observation $\boldsymbol{z}(k+1)$, and are given by

$$\boldsymbol{i}(k+1) = \mathbf{H}^{\mathsf{T}}(k+1)\mathbf{R}^{-1}\left[\boldsymbol{\nu}(k+1)+\mathbf{H}(k+1)\hat{\boldsymbol{x}}(k+1|k)\right]$$

$$\begin{aligned}\mathbf{I}(k+1) &= \mathbf{H}^{\mathsf{T}}(k+1)\mathbf{R}^{-1}\mathbf{H}(k+1)\\ \boldsymbol{\nu}(k+1) &= \boldsymbol{z}(k+1)-\boldsymbol{h}\left[\hat{\boldsymbol{x}}(k+1|k)\right]\\ \mathbf{H}(k+1) &= \left.\frac{\partial \boldsymbol{h}\left[\boldsymbol{x}(k)\right]}{\partial \boldsymbol{x}}\right|_{\boldsymbol{x}=\hat{\boldsymbol{x}}(k+1|k)}.\end{aligned}$$

4.4.2.3 Optimal Greedy Control

This block takes the estimate $\hat{\boldsymbol{x}}(k|k)$ and an associated estimation error covariance $\mathbf{P}(k|k)$ of the signal landscape map and solves for the optimal greedy maneuver $\boldsymbol{u}^{\star}_{r_i}(k)$ with which the ith receiver, for $i = 1, \ldots, N$, where N is the number of receivers, must move so to minimize a functional of the control input $\mathcal{J}\left[\boldsymbol{u}_{r_i}(k)\right]$. To this end, to specify $\mathcal{J}\left[\boldsymbol{u}_{r_i}(k)\right]$, the D-optimality criterion will be chosen. Recall from Subsection 4.2.2 that the D-optimality criterion is proportional to the volume of the estimation error uncertainty ellipsoid and was demonstrated in Subsection 4.2.6 to be superior to the A- and E-optimality criteria in an RMSEE sense. Hence, this block solves the OGC problem, given by

$$
\begin{aligned}
\underset{\boldsymbol{u}_{r_i}(k)}{\text{minimize}} \quad & \mathcal{J}\left[\boldsymbol{u}_{r_i}(k)\right] = \log\det \mathbf{P}_i(k+1|k+1) \\
\text{subject to} \quad & \boldsymbol{x}_{r_i}(k+1) \;=\; \mathbf{F}_{r_i}\,\boldsymbol{x}_{r_i}(k) + \mathbf{G}_{r_i}\,\boldsymbol{u}_{r_i}(k) + \boldsymbol{w}_{r_i}(k) \\
& \boldsymbol{x}_{s_j}(k+1) \;=\; \mathbf{F}_{s}\,\boldsymbol{x}_{s_j}(k) + \boldsymbol{w}_{s_j}(k), \;\; j = 1, \ldots, m \\
& z_j(k) \;=\; h\left[\boldsymbol{x}_{r_i}(k),\, \boldsymbol{x}_{s_j}(k)\right] + \boldsymbol{v}_{s_j}(k), \;\; j = 1, \ldots, m \\
& \|\boldsymbol{u}_{r_i}(k)\|_2 \;\leq\; a_{r_i,\max}, \\
& \left\| \boldsymbol{u}_{r_i}(k) + \frac{1}{T}\boldsymbol{v}^{\star}_{r_i}(k-1) \right\|_2 \;\leq\; \frac{1}{T} v_{r_i,\max},
\end{aligned}
\tag{4.7}
$$

where $v_{r_i,\max}$ and $a_{r_i,\max}$ are the maximum speed and acceleration, respectively, with which the ith receiver can move. Note that the optimization vector is $\boldsymbol{u}_{r_i}(k)$, whereas $\boldsymbol{v}^{\star}_{r_i}(k-1)$ is a known constant vector representing the velocity commands that resulted from solving the optimization problem in the previous time-step $k-1$ and has already been applied.

4.4.2.4 Actuators

This block applies the optimal control inputs $\boldsymbol{u}_{r_i}^{\star}(k)$ in the form of acceleration commands, which are calculated by the OGC, to command the receiver's next maneuver .

4.4.3 Active Signal Landscape Mapping Architectures

This subsection presents the various active signal landscape mapping architectures. The architectures are essentially classified according to where active decisions about the maneuvers are made, what information is communicated, and where the information is processed [125].

4.4.3.1 Decentralized

In this architecture (depicted in Figure 4.29), each receiver acts individually: it fuses the observations made on the various SOPs to produce its own signal landscape map and makes its own decisions. The observations made by the ith receiver on all the SOPs in the environment are augmented into the vector $\boldsymbol{z}_i \triangleq [z_{r_i,s_1}, \cdots, z_{r_i,s_m}]^{\mathsf{T}}$, which is subsequently processed by the EIF to yield the *local* signal landscape state estimate $\hat{\boldsymbol{x}}_i(k|k)$ and associated estimation error covariance $\mathbf{P}_i(k|k)$. Based on these local estimates, each receiver solves for its own optimal greedy maneuver $\boldsymbol{u}_{r_i}^{\star}(k)$ defined in (4.7).

This architecture has the advantages of simplicity and self-containment, but suffers from the drawback that receivers do not exploit information gathered by other concurrent receivers.

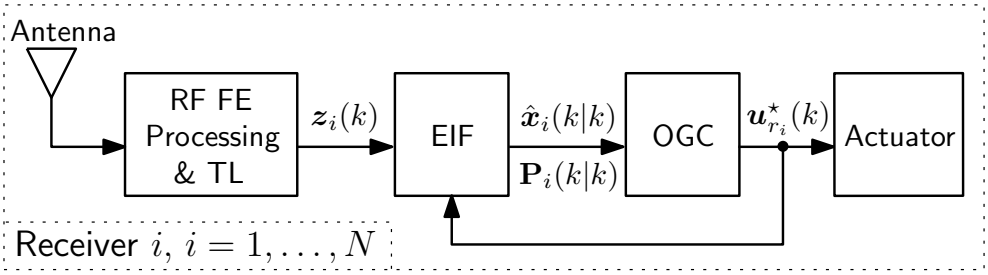

Figure 4.29: Decentralized active signal landscape mapping architecture

4.4.3.2 Centralized

In this architecture (depicted in Figure 4.30), the signal landscape map and decision making are made at a central fusion and decision center (CF & DC). The receivers send their observation vectors $\{\boldsymbol{z}_i\}_{i=1}^N$ to the CF & DC, which fuses such observations through an EIF to produce a *global* signal landscape map with estimate $\hat{\boldsymbol{x}}(k|k)$ and associated estimation error covariance $\mathbf{P}(k|k)$. The CF & DC OGC problem is identical to (4.7), except that it solves for the *global* optimal greedy maneuver for all receivers $\boldsymbol{u}^\star(k) \triangleq \left[[\boldsymbol{u}^\star_{r_1}(k)]^\mathsf{T}, \cdots, [\boldsymbol{u}^\star_{r_N}(k)]^\mathsf{T}\right]^\mathsf{T}$. The optimal maneuvers are communicated to each receiver.

This architecture is optimal; however, it requires two-way communication between the receivers and the CF & DC. Another drawback is that the CF & DC needs to solve a potentially large-scale OGC problem.

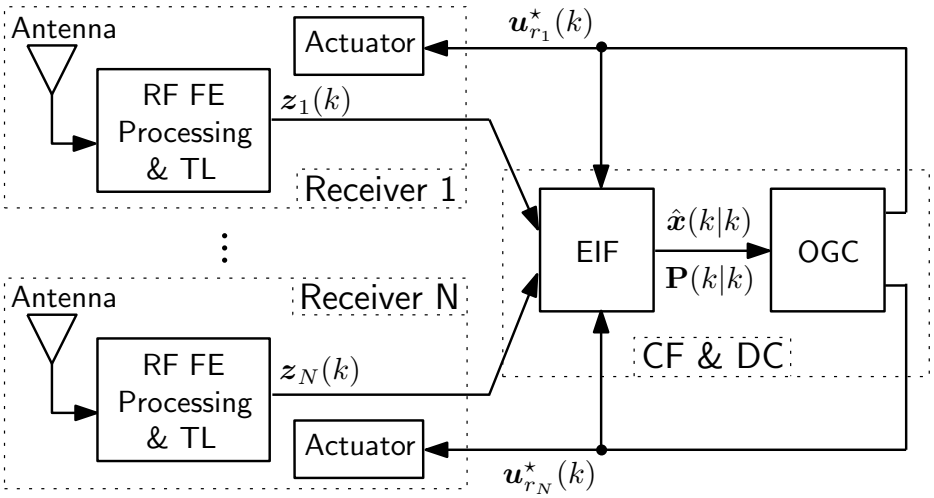

Figure 4.30: Centralized active signal landscape mapping architecture

4.4.3.3 Hierarchical without Feedback

In this architecture (depicted in Figure 4.31), the receivers produce their own signal landscape maps and make their own decisions. Additionally, they send their information contribution vectors and matrices $\{\boldsymbol{i}_{r_i}, \mathbf{I}_{r_i}\}_{i=1}^{N}$ to a central fusion center (CFC). The CFC is composed of an EIF, which maintains a *global* signal landscape map. The CFC EIF's prediction stage computations are made according to the prediction equations given in Subsection 4.4.2.2, while the correction stage computations are made according to

$$\begin{aligned}\hat{\boldsymbol{y}}(k+1|k+1) &= \hat{\boldsymbol{y}}(k+1|k) + \sum_{i=1}^{N} \boldsymbol{i}_{r_i}(k+1) \\ \mathbf{Y}(k+1|k+1) &= \mathbf{Y}(k+1|k) + \sum_{i=1}^{N} \mathbf{I}_{r_i}(k+1).\end{aligned}$$

This architecture has the following advantages: (i) receivers possess their own local maps and (ii) a more accurate global map is available at the

CFC. However, it suffers from the drawback that receivers have no access to the global map.

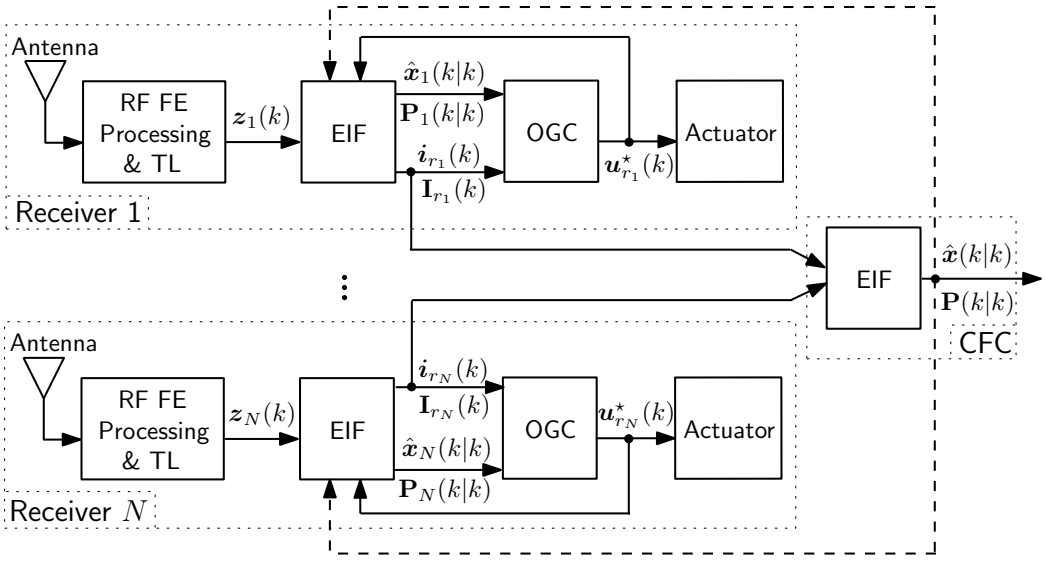

Figure 4.31: Hierarchical active signal landscape mapping architecture without feedback (no dashed line) and with feedback (with dashed line)

4.4.3.4 Hierarchical with Feedback

This architecture (depicted in Figure 4.31), is identical to the one described in subsection 4.4.3.3, except that once the CFC fuses the information from the various receivers to produce the *global* signal landscape map, such map is fed-back to each receiver to replace each receiver's local corrected map.

This architecture eliminates the drawback of the hierarchical without feedback architecture at the expense of requiring communication from the CFC to the receivers.

4.4.4 Simulation Results

This subsection compares the architectures discussed in Subsection 4.4.3 numerically in an environment comprising two receivers with known initial states and four unknown SOPs. For purposes of numerical stability, the clock bias and drift states were defined as $c\delta t$ and $c\dot{\delta}t$, respectively. The receivers' and SOPs' clocks were assumed to be TCXOs and OCXOs, respectively. The simulation settings are given in Table 4.5.

Table 4.5: Collaborative signal landscape mapping simulation settings

Parameter	**Value**
$\boldsymbol{x}_{s_1}(0)$	$[\,0,\ 150,\ 10,\ 0.1\,]^\mathsf{T}$
$\boldsymbol{x}_{s_2}(0)$	$[\,100,\ -150,\ 20,\ 0.2\,]^\mathsf{T}$
$\boldsymbol{x}_{s_3}(0)$	$[\,200,\ 200,\ 30,\ 0.3\,]^\mathsf{T}$
$\boldsymbol{x}_{s_4}(0)$	$[\,-150,\ 50,\ 40,\ 0.4\,]^\mathsf{T}$
$\boldsymbol{x}_{r_i}(0)$	$\sim \mathcal{N}\left[\bar{\boldsymbol{x}}_{r_i}, \mathbf{P}_{r_i}\right]; \quad i = 1, 2$
$\bar{\boldsymbol{x}}_{r_1}$	$[\,60,\ 15,\ 100,\ 10\,]^\mathsf{T}$
$\bar{\boldsymbol{x}}_{r_2}$	$[\,-55,\ 50,\ 100,\ 10\,]^\mathsf{T}$
$\hat{\boldsymbol{x}}_{s_j}(0\|0)$	$\sim \mathcal{N}\left[\boldsymbol{x}_{s_j}(0), \mathbf{P}_{s_j}(0\|0)\right]; \quad j = 1, \ldots, 4$
$\mathbf{P}_{r_i}$	$(10^4) \cdot \mathrm{diag}\left[\,1,\ 1,\ 0,\ 0,\ 1,\ 10^{-2}\,\right]; \quad i = 1, 2$
$\mathbf{P}_{s_j}(0\|0)$	$(10^4) \cdot \mathrm{diag}\left[\,1,\ 1,\ 1,\ 10^{-2}\,\right]; \quad j = 1, \ldots, 4$
h_{0,r_i}	$2 \times 10^{-19}, \quad i = 1, 2$
h_{-2,r_i}	$2 \times 10^{-20}, \quad i = 1, 2$
h_{0,s_j}	$8 \times 10^{-20}, \quad j = 1, \ldots, 4$
h_{-2,s_j}	$4 \times 10^{-23}, \quad j = 1, \ldots, 4$
r_{r_i,s_j}	$500\,\mathrm{m}^2; \quad i = 1, 2;\ j = 1, \ldots, 4$
$\tilde{q}_x, \tilde{q}_y$	$0.1\,(\mathrm{m/s}^2)^2$
$v_{\max}$	$10\,\mathrm{m/s}$
$a_{\max}$	$5\,\mathrm{m/s}^2$
T	$0.1\,\mathrm{s}$

Figure 4.32 shows the receivers trajectories due to the four architectures. Note that the trajectory for the hierarchical without feedback was identical to the decentralized, since receivers had no access to the global map. Figure 4.33 compares the quality of the maps produced by the four architectures for a single run, as measured by the optimal value of the objective functional, denoted $\mathcal{J}^\star = \log\det\left[\mathbf{P}^\star(k+1|k+1)\right]$, which is proportional to the volume of the estimation uncertainty ellipsoid. Here, for meaningful comparison, the same initial conditions, initial state estimates, and process and observation noise realizations were used.

The PoA was calculated as the ensemble average at the end of the simulation time for 25 Monte Carlo simulation runs, where the receivers' initial states, SOPs initial state estimates, and noise realizations were randomized over each run, and is tabulated in Table 4.6. Note that the hierarchial approach with feedback had a negligible PoA; hence, we conclude that it has a comparable performance to the optimal centralized approach.

Table 4.6: Price of anarchy for collaborative signal landscape mapping architectures

Architecture	**Average**	**Standard Deviation**
Decentralized	1.91	0.13
Hierarchical without Feedback	1.18	0.11
Hierarchical with Feedback	1.03	0.04

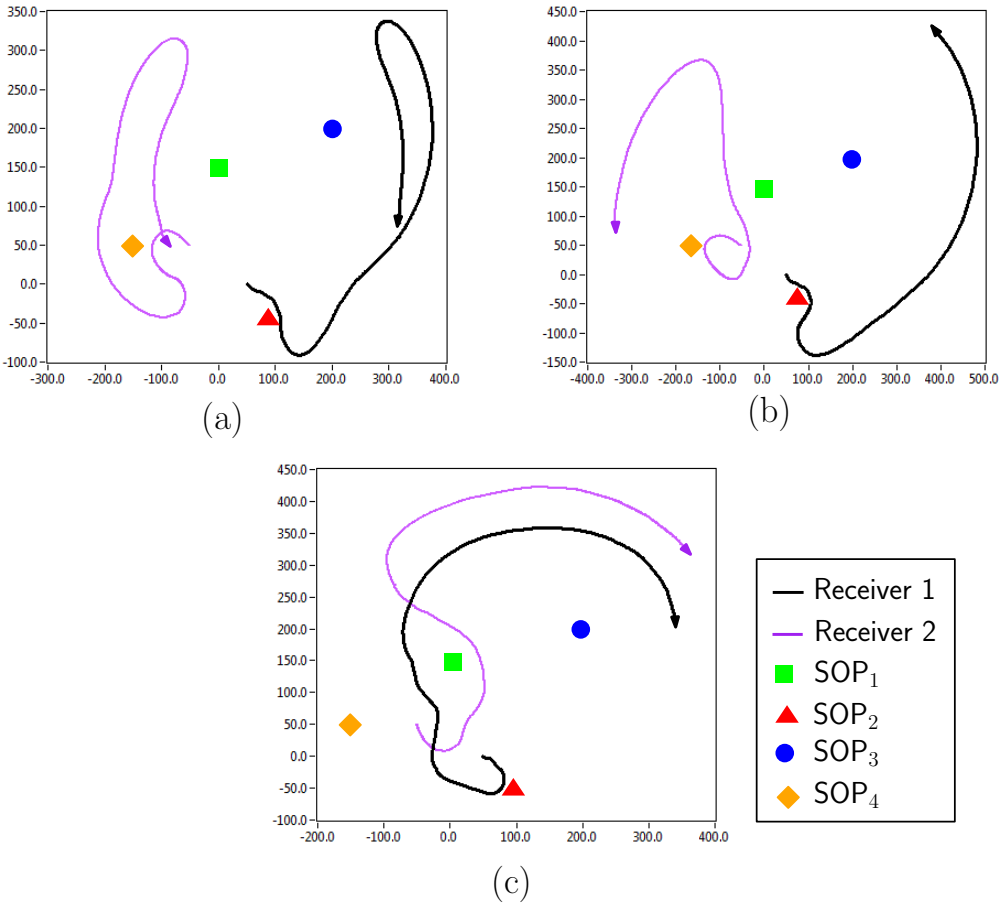

Figure 4.32: Receiver trajectories for (a) centralized, (b) hierarchical with feedback, and (c) decentralized and hierarchical without feedback architectures

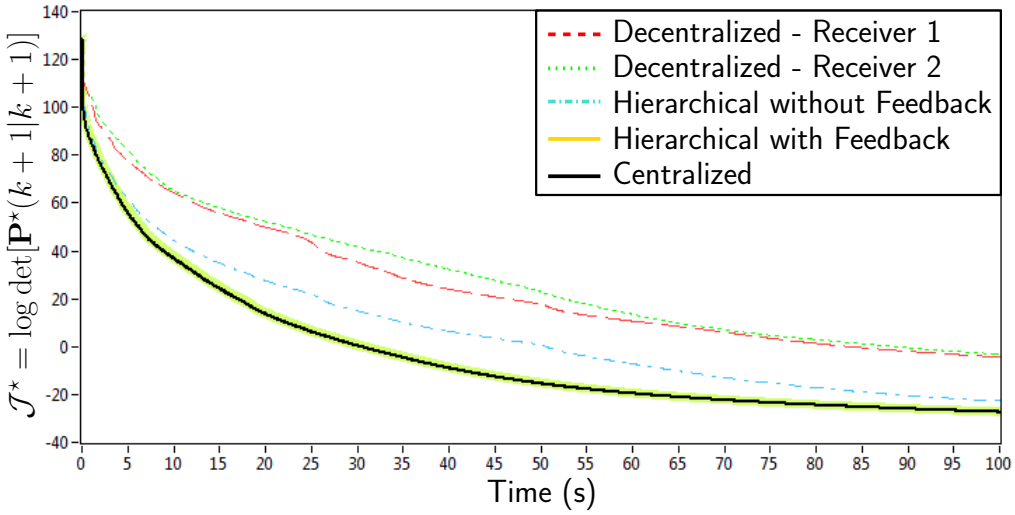

Figure 4.33: Signal landscape map uncertainty

Chapter 5

Conclusion

This dissertation laid down the theoretical foundation and addressed fundamental analysis and synthesis questions pertaining to COpNav. In COpNav, multiple receivers, whether in hand-held devices, in UAVs, UGVs, or manned vehicles share information about ambient radio frequency SOPs to construct and continuously refine a global signal landscape within which the receivers localize themselves in space and time.

The minimal conditions under which a COpNav environment comprising multiple receivers with velocity random walk dynamics making pseudorange observations on multiple terrestrial SOPs were derived. It was shown that the environment is completely observable if the initial states of at least: (i) one receiver is fully-know, (ii) one receiver is partially-known and one SOP is fully-known, or (iii) one SOP is fully-known and one SOP is partially-known. If the receivers can control their maneuvers in the form of acceleration commands, these observability requirement reduce to (i) one receiver is fully-known or (ii) one SOP is fully-known. For scenarios in which the environment is not fully-observable, the observable states in the environment were specified. Moreover, the degree of observability (estimability) of the various states in the

environment was assessed with particular attention paid to the most and least observable directions in the state space. Numerical and experimental demonstrations were presented, which agreed with the theoretical predictions.

Next, various receiver motion planning strategies for optimal information gathering were proposed. In this respect, classical information-based metrics were derived, and it was shown that their associated optimization problems did not possess any convexity properties. Subsequently, novel innovation-based metrics were proposed and derived, whose associated optimization problems were shown to possess strong convexity properties, yielding computationally efficient solutions. Analytical and numerical comparisons between the information- and innovation-based solutions were presented showing that the two sets of metrics perform comparably. In addition, the superiority of receding horizon motion strategies over greedy was assessed. It was demonstrated that such strategies are more beneficial in the case of signal landscape mapping versus the case of simultaneous receiver localization and signal landscape mapping. Also, it was demonstrated that the superiority diminished whenever the environment uncertainty in the form of observation noise intensity increased. Finally, the problem of collaborative signal landscape mapping with multiple receivers was tackled. A number of decision making and information fusion architectures were synthesized: centralized, decentralized, and hierarchical with and without feedback. It was demonstrated that a hierarchical with feedback architecture achieved a minimal price of anarchy.

Chapter 6

Future Work

This chapter outlines a number of future research directions that build upon this dissertation's findings.

6.1 Navigation Security

We are steadily moving towards a world in which UGVs roam the streets side-by-side with human-driven vehicles, and UAVs are integrated into the national airspace. Not only will such future autonomous vehicles demand more accuracy and reliability from their navigation system, but they will also be asked to operate in harsher environments than ever before. Jamming and spoofing these navigation systems will have intolerable consequences. The proposed COpNav framework implicitly protects against jamming and spoofing threats through signal diversification. Near-term research should design appropriate detection and mitigation algorithms against these malicious attacks. Moreover, established receiver autonomous integrity monitoring (RAIM) techniques should be extended to incorporate signals beyond GNSS, namely SOPs.

6.2 Adaptive Estimation

A COpNav receiver entering a new signal landscape cannot assume the availability of high-fidelity models describing the environment's dynamics. Uncertainties in COpNav environments can be classified into dynamical and statistical uncertainties, with the latter being more problematic. Incorrect models jeopardize the estimation optimality and may cause filter divergence. COpNav estimators need to: (*i*) perform on-the-fly signal characterization for discovered SOPs and (*ii*) continuously refine estimates of SOPs' parameters of relevance. To this end, adaptive estimators, which provide a significant improvement over fixed filters through the filter learning process, will be necessary. These adaptive estimator should exploit proper parametrization of different grades of receivers and SOPs oscillators.

6.3 Estimation Architectures

A significant difference between COpNav environments and conventional distributed multi-sensor networks is that COpNav receivers are not merely sensors– they are closed-loop systems composed of feedback tracking loops. Future research should study the performance and limitations of various estimation architectures, such as decentralized, centralized, and hierarchical. Questions pertaining to necessary communication rates, effects of communication delay and disconnectivity, and appropriate estimators and information fusion techniques should be addressed.

Appendix

Appendix 1

Appendix for Chapter 4

1.1 Commutativity of Dynamics Matrices

Proposition 1.1.1. *The matrices* $\mathbf{F}_0'$ *and* $\sum_{i=1}^{2} \mathbf{F}_i u_i$ *are commutative.*

Proof. Denoting $\mathbf{A} \triangleq \mathbf{F}_0'$ and $\mathbf{B} \triangleq \sum_{i=1}^{2} \mathbf{F}_i u_i$, direct calculations reveal that

$$\mathbf{AB} = \mathbf{BA} = \text{diag}\left[\mathbf{F}'_{3,s_a}, \mathbf{F}'_{3,s_1}, \ldots, \mathbf{F}'_{3,s_m}, \mathbf{0}_{(2m+4)\times(2m+4)}\right],$$

$$\mathbf{F}'_{3,s_j} = \begin{bmatrix} 0 & 0 & 0 & 0 \\ 0 & 0 & 0 & 0 \\ 0 & 0 & 0 & 0 \\ \frac{2\,\dot{r}_{s_j}\dot{\theta}_{s_j}\left(u_1 \sin\theta_{s_j} - u2\cos\theta_{s_j}\right)}{r_{s_j}^3} & 0 & 0 & 0 \end{bmatrix},$$

where $j = a, 1, \ldots, m$. □

1.2 Matrix Blocks for Equation (4.4)

$$\mathbf{\Lambda}(k) = \begin{bmatrix} \mathbf{\Lambda}_{s_a} & \mathbf{0}_{4\times4} & \cdots & \mathbf{0}_{4\times4} & \mathbf{0}_{4\times2} \\ \mathbf{\Lambda}_{s_1} & -\mathbf{\Lambda}_{s_1} & \cdots & \mathbf{0}_{4\times4} & \mathbf{0}_{4\times2} \\ \vdots & \vdots & \ddots & \vdots & \vdots \\ \mathbf{\Lambda}_{s_m} & \mathbf{0}_{4\times4} & \cdots & -\mathbf{\Lambda}_{s_m} & \mathbf{0}_{4\times2} \\ \mathbf{\Lambda}_{\text{clk},r} & \mathbf{0}_{2\times4} & \cdots & \mathbf{0}_{2\times4} & \mathbf{0}_{2\times2} \\ \mathbf{0}_{2\times4} & \mathbf{\Lambda}_{\text{clk},s_1} & \cdots & \mathbf{0}_{2\times4} & \mathbf{0}_{2\times2} \\ \vdots & \vdots & \ddots & \vdots & \vdots \\ \mathbf{0}_{2\times4} & \mathbf{0}_{2\times4} & \cdots & \mathbf{\Lambda}_{\text{clk},s_m} & \mathbf{0}_{2\times2} \\ \mathbf{0}_{2\times4} & \mathbf{0}_{2\times4} & \cdots & \mathbf{0}_{2\times4} & \mathbf{\Lambda}_{\text{clk},s_a} \end{bmatrix}.$$

$$\boldsymbol{\Lambda}_{s_j} \triangleq \begin{bmatrix} \boldsymbol{\Lambda}_{r_{s_j},x_r} & \boldsymbol{\Lambda}_{r_{s_j},y_r} & 0 & 0 & 0 & 0 \\ \boldsymbol{\Lambda}_{\theta_{s_j},x_r} & \boldsymbol{\Lambda}_{\theta_{s_j},y_r} & 0 & 0 & 0 & 0 \\ \boldsymbol{\Lambda}_{\dot{r}_{s_j},x_r} & \boldsymbol{\Lambda}_{\dot{r}_{s_j},y_r} & \boldsymbol{\Lambda}_{\dot{r}_{s_j},\dot{x}_r} & \boldsymbol{\Lambda}_{\dot{r}_{s_j},\dot{y}_r} & 0 & 0 \\ \boldsymbol{\Lambda}_{\dot{\theta}_{s_j},x_r} & \boldsymbol{\Lambda}_{\dot{\theta}_{s_j},y_r} & \boldsymbol{\Lambda}_{\dot{\theta}_{s_j},\dot{x}_r} & \boldsymbol{\Lambda}_{\dot{\theta}_{s_j},\dot{y}_r} & 0 & 0 \end{bmatrix}$$

$$\boldsymbol{\Lambda}_{r_{s_j},x_r}=\boldsymbol{\Lambda}_{\dot{r}_{s_j},\dot{x}_r}=\frac{x_r-x_{s_j}}{\|\boldsymbol{r}_r-\boldsymbol{r}_{s_j}\|},\ \boldsymbol{\Lambda}_{r_{s_j},y_r}=\boldsymbol{\Lambda}_{\dot{r}_{s_j},\dot{y}_r}=\frac{y_r-y_{s_j}}{\|\boldsymbol{r}_r-\boldsymbol{r}_{s_j}\|}$$

$$\boldsymbol{\Lambda}_{\theta_{s_j},x_r}=\boldsymbol{\Lambda}_{\dot{\theta}_{s_j},\dot{x}_r}=\frac{-y_r+y_{s_j}}{\|\boldsymbol{r}_r-\boldsymbol{r}_{s_j}\|^2},\ \boldsymbol{\Lambda}_{\theta_{s_j},y_r}=\boldsymbol{\Lambda}_{\dot{\theta}_{s_j},\dot{y}_r}=\frac{x_r-x_{s_j}}{\|\boldsymbol{r}_r-\boldsymbol{r}_{s_j}\|^2}$$

$$\boldsymbol{\Lambda}_{\dot{r}_{s_j},x_r}=\frac{\left[\dot{y}_r(-x_r+x_{s_j})+\dot{x}_r(y_r-y_{s_j})\right](y_r-y_{s_j})}{\|\boldsymbol{r}_r-\boldsymbol{r}_{s_j}\|^3}$$

$$\boldsymbol{\Lambda}_{\dot{r}_{s_j},y_r}=\frac{\left[\dot{y}_r(x_r-x_{s_j})+\dot{x}_r(-y_r+y_{s_j})\right](x_r-x_{s_j})}{\|\boldsymbol{r}_r-\boldsymbol{r}_{s_j}\|^3}$$

$$\boldsymbol{\Lambda}_{\dot{\theta}_{s_j},x_r}=\Big\{\dot{y}_r\left[-(x_r-x_{s_j})^2+(y_r-y_{s_j})^2\right] +2\dot{x}_r(x_r-x_{s_j})(y_r-y_{s_j})\Big\}\Big/\|\boldsymbol{r}_r-\boldsymbol{r}_{s_j}\|^2$$

$$\boldsymbol{\Lambda}_{\dot{\theta}_{s_j},y_r}=\Big\{\dot{x}_r\left[-(x_r-x_{s_j})^2+(y_r-y_{s_j})^2\right] -2\dot{y}_r(x_r-x_{s_j})(y_r-y_{s_j})\Big\}\Big/\|\boldsymbol{r}_r-\boldsymbol{r}_{s_j}\|^2$$

$$\boldsymbol{\Lambda}_{\text{clk},r} \triangleq \begin{bmatrix} \mathbf{0}_{2\times 4} & \mathbf{I}_{2\times 2} \end{bmatrix}$$

$$\boldsymbol{\Lambda}_{\text{clk},s_j} \triangleq \begin{bmatrix} \mathbf{0}_{2\times 2} & \mathbf{I}_{2\times 2} \end{bmatrix}, \quad j = a, 1, \ldots, m.$$

1.3 Linear Functionals Convexity Properties

Lemma 1.3.1. *The functional* $f(\boldsymbol{x}) = \log\left[\det\left(\mathbf{A}_0 + \sum_{i=1}^n x_i\mathbf{A}_i\right)\right]$, *where* $\boldsymbol{x} \in \mathbb{R}^n$ *and* $\mathbf{A}_i \in \mathbb{S}^m$ *is concave on* $\{\boldsymbol{x} : \mathbf{A}_0 + \sum_{i=1}^n x_i\mathbf{A}_i \succ 0\}$.

Proof. Since nonnegative weighting of a concave functional preserves its con-

cavity, consider the functional

$$\begin{aligned} f(\boldsymbol{x}) &= \frac{1}{m}\log\left[\det\left(\mathbf{A}_0+\sum_{i=1}^{n}x_i\mathbf{A}_i\right)\right] \\ &= \log\left\{\left[\det\left(\mathbf{A}_0+\sum_{i=1}^{n}x_i\mathbf{A}_i\right)\right]^{\frac{1}{m}}\right\} \\ &\triangleq h\left[g(\boldsymbol{x})\right] \end{aligned}$$

Using the fact that the functional $g'(\boldsymbol{x}) = -\left[\det\left(\mathbf{A}_0+\sum_{i=1}^{n}x_i\mathbf{A}_i\right)\right]^{\frac{1}{m}}$, where $\boldsymbol{x}\in\mathbb{R}^n$ and $\mathbf{A}_i\in\mathbb{S}^m$ is convex on $\{\boldsymbol{x}:\mathbf{A}_0+\sum_{i=1}^{n}x_i\mathbf{A}_i\succ 0\}$; hence, $g(\boldsymbol{x})\triangleq -g'(\boldsymbol{x})$ is concave. Recognizing that h is concave and nondecreasing, we conclude that f is concave, from applying the composition rule: if $f(\boldsymbol{x})\triangleq h\left[g(\boldsymbol{x})\right]$, with $h:\mathbb{R}\to\mathbb{R}$ and $g:\mathbb{R}^n\to\mathbb{R}$, then f is concave if h is concave and nondecreasing and g is concave [114]. □

Lemma 1.3.2. *The functional* $f(\boldsymbol{x})=\lambda_{\max}\left[\mathbf{A}_0+\sum_{i=1}^{n}x_i\mathbf{A}_i\right]$, *where* $\boldsymbol{x}\in\mathbb{R}^n$ *and* $\mathbf{A}_i\in\mathbb{S}^n$ *is convex.*

Proof. The functional f can be expressed as

$$f(\boldsymbol{x}) = \sup_{\|\boldsymbol{y}\|_2=1}\left[\boldsymbol{y}^{\mathsf{T}}\left(\mathbf{A}_0+\sum_{i=1}^{n}x_i\mathbf{A}_i\right)\boldsymbol{y}\right].$$

Since f is the point-wise supremum of a family of liner functionals of $\boldsymbol{x}$, i.e. $\boldsymbol{y}^{\mathsf{T}}\left(\mathbf{A}_0+\sum_{i=1}^{n}x_i\mathbf{A}_i\right)\boldsymbol{y}$, indexed by $\boldsymbol{y}\in\mathbb{R}^n$, and using the fact that the point-wise supremum of convex functionals is convex, then f is convex. □

Bibliography

[1] R.B. Langley. Navigation 101: Basic navigation with a GPS receiver. *GPS World Magazine*, pages 50–54, October 2000.

[2] R. Charette. Are we getting overly reliant on GPS-intensive systems? *IEEE Spectrum Online*. http://spectrum.ieee.org/riskfactor/aerospace/satellites/are-we-getting-overly-reliant-on-gps-systems, March 2011. Accessed March 9, 2011.

[3] M. Thomas. Global navigation space systems: reliance and vulnerabilities. *The Royal Academy of Engineering*. http://www.raeng.org.uk/news/publications/list/reports/RAoE_Global_Navigation_Systems_Report.pdf, March 2011. Accessed March 9, 2011.

[4] Inside GNSS News. PNT homeland security official links GPS interference to wider cybersecurity concerns. http://www.insidegnss.com/node/3108, June 2012. Accessed June 18, 2012.

[5] K. Moskvitch. BAE Systems' Navsop navigation system rivals GPS. http://www.bbc.com/news/technology-18633917, June 2012. Accessed June 28, 2012.

[6] European GNSS Agency (GSA). GNSS market report. http://www.gsa.europa.eu/sites/default/files/GNSS_Market%20Report_2013_web.pdf, October 2013. Accessed October 17, 2013.

[7] GPS World. LBS market worth $39.87 billion by 2019. http://gpsworld.com/lbs-market-worth-39-87-billion-by-2019, April 2014. Accessed April 11, 2014.

[8] G. Seco-Granados, J.A. Lopez-Salcedo, D. Jimenez-Banos, and G. Lopez-Risueno. Challenges in indoor global navigation satellite systems: unveiling its core features in signal processing. *IEEE Signal Processing Magazine*, 29(2):108–131, March 2012.

[9] Federal Communications Commission. Wireless E911 location accuracy requirements. http://www.fcc.gov/guides/wireless-911-services. Accessed May 1, 2014.

[10] S. Ji, W. Chen, X. Ding, Y. Chen, C. Zhao, and C. Hu. Potential benefits of GPS/GLONASS/GALILEO integration in an urban canyon – Hong Kong. *Journal of Navigation*, 63(04):681–693, October 2010.

[11] T.R. Shields. National advisory board on space-based positioning, navigation, and timing: precise positioning – automated driving & safety communications. http://www.gps.gov/governance/advisory/meetings/2013-12/shields.pdf, December 2013. Accessed December 4, 2013.

[12] J.C. Grabowski. Personal privacy jammers: locating Jersey PPDs jamming GBAS safety-of-life signals. *GPS World Magazine*, pages 28–37, April 2012.

[13] K. Wesson and T.E. Humphreys. Better security measures are needed before drones roam the U.S. airspace. *Scientific American*, 309(5):54–59, November 2013.

[14] A.J. Kerns, D.P. Shepard, J.A. Bhatti, and T.E. Humphreys. Unmanned aircraft capture and control via GPS spoofing. *Journal of Field Robotics*, 2014. to be published.

[15] R. Toledo-Moreo, M.A. Zamora-Izquierdo, B. Ubeda-Miarro, and A.F. Gomez-skarmeta. High-integrity IMM-EKF-based road vehicle navigation with low-cost GPS/SBAS/INS. *IEEE Transactions on Intelligent Transportation Systems*, 8(3):491–511, September 2007.

[16] I. Skog and P. Handel. In-car positioning and navigation technologies - a survey. *IEEE Transactions on Intelligent Transportation Systems*, 10(1):4–21, March 2009.

[17] A. Ramanandan, A. Chen, and J.A. Farrell. Inertial navigation aiding by stationary updates. *IEEE Transactions on Intelligent Transportation Systems*, 13(1):235–248, March 2012.

[18] P.D. Groves. The PNT boom: future trends in integrated navigation. *Inside GNSS*, pages 44–49, March/April 2013.

[19] J. Farrell and M. Barth. *The Global Positioning System and Inertial Navigation*. McGraw-Hill, New York, 1998.

[20] P.D. Groves. *Principles of* GNSS*, Inertial, and Multisensor Integrated Navigation Systems*. Artech House, second edition, 2013.

[21] M.J. Veth. *Fusion of imaging and inertial sensors for navigation*. PhD thesis, Air Force Institute of Technology, Wright-Patterson Air Force Base, Ohio, USA, 2006.

[22] S.S. Saab. A map matching approach for train positioning–part I: development and analysis. *IEEE Transactions on Vehicular Technology*, 49(2):467–475, March 2000.

[23] S.S. Saab. A map matching approach for train positioning–part II: application and experimentation. *IEEE Transactions on Vehicular Technology*, 49(2):476–484, March 2000.

[24] S.S. Saab and Z.M. Kassas. Map-based land vehicle navigation system with DGPS. In *Proceedings of IEEE Intelligent Vehicle Symposium*, volume 1, pages 209–214, June 2002.

[25] S.S. Saab and Z.M. Kassas. Power matching approach for GPS coverage extension. *IEEE Transactions on Intelligent Transportation Systems*, 7(2):156–166, June 2006.

[26] L. Wang, P.D. Groves, and M.K. Ziebart. GNSS shadow matching: improving urban positioning accuracy using a 3D city model with opti-

mized visibility scoring scheme. *NAVIGATION, Journal of the Institute of Navigation*, 60(3):195–207, 2013.

[27] K.A. Fisher. *The navigation potential of signals of opportunity-based time difference of arrival measurements*. PhD thesis, Air Force Institute of Technology, Wright-Patterson Air Force Base, Ohio, USA, 2005.

[28] L.A. Merry, R.M. Faragher, and S.J. Scheding. Comparison of opportunistic signals for localisation. In *Proceedings of IFAC Symposium on Intelligent Autonomous Vehicle*, volume 7, pages 109–114, September 2010.

[29] M.A. Enright and C.N. Kurby. A signals of opportunity based cooperative navigation network. In *Proceedings of the IEEE National Aerospace Electronics Conference*, pages 213–218, July 2009.

[30] D. Borio, C. Mongredien, and G. Lachapelle. Collaborative code tracking of composite GNSS signals. *IEEE Journal of Selected Topics in Signal Processing*, 3(4):613–626, August 2009.

[31] P. Robertson, M.G. Puyol, and M. Angermann. Collaborative pedestrian mapping of buildings using inertial sensors and FootSLAM. In *Proceedings of ION GNSS*, pages 1366–1377, September 2011.

[32] K.M. Pesyna, Z.M. Kassas, J.A. Bhatti, and T.E. Humphreys. Tightly-coupled opportunistic navigation for deep urban and indoor positioning. In *Proceedings of ION GNSS*, pages 3605–3617, September 2011.

[33] J.J. Caffery and G.L. Stuber. Overview of radiolocation in CDMA cellular systems. *IEEE Communications Magazine*, 36(4):38–45, April 1998.

[34] F. Gustafsson and F. Gunnarsson. Mobile positioning using wireless networks: possibilities and fundamental limitations based on available wireless network measurements. *IEEE Signal Processing Magazine*, 22(4):41–53, July 2005.

[35] G. De Angelis, G. Baruffa, and S. Cacopardi. GNSS/cellular hybrid positioning system for mobile users in urban scenarios. *IEEE Transactions on Intelligent Transportation Systems*, 14(1):313–321, March 2013.

[36] C. Yang, T. Nguyen, E. Blasch, and D. Qiu. Assessing terrestrial wireless communications and broadcast signals as signals of opportunity for positioning and navigation. In *Proceedings of ION GNSS*, pages 3814–3824, September 2012.

[37] M. Rabinowitz and J.J. Spilker, Jr. A new positioning system using television synchronization signals. *IEEE Transactions on Broadcasting*, 51(1):51–61, March 2005.

[38] P. Thevenon, S. Damien, O. Julien, C. Macabiau, M. Bousquet, L. Ries, and S. Corazza. Positioning using mobile TV based on the DVB-SH standard. *NAVIGATION, Journal of the Institute of Navigation*, 58(2):71–90, 2011.

[39] J.A. McEllroy. Navigation using signals of opportunity in the AM transmission band. Master's thesis, Air Force Institute of Technology, Wright-Patterson Air Force Base, Ohio, USA, 2006.

[40] V. Moghtadaiee, A.G. Dempster, and S. Lim. Indoor localization using FM radio signals: A fingerprinting approach. In *International Conference on Indoor Positioning and Indoor Navigation*, pages 1–7, September 2011.

[41] J. Biswas and M. Veloso. WiFi localization and navigation for autonomous indoor mobile robots. In *IEEE International Conference on Robotics and Automation*, pages 4379–4384, May 2010.

[42] L. Bruno and P. Robertson. WiSLAM: improving FootSLAM with WiFi. In *International Conference on Indoor Positioning and Indoor Navigation*, pages 1–10, September 2011.

[43] M. Joerger, L. Gratton, B. Pervan, and C.E. Cohen. Analysis of Iridium-augmented GPS for floating carrier phase positioning. *NAVIGATION, Journal of the Institute of Navigation*, 57(2):137–160, 2010.

[44] K.M. Pesyna, Z.M. Kassas, and T.E. Humphreys. Constructing a continuous phase time history from TDMA signals for opportunistic navigation. In *Proceedings of IEEE/ION Position Location and Navigation Symposium*, pages 1209–1220, April 2012.

[45] L.-P. Gill, D. Grenier, and J.-Y. Chouinard. Use of XM radio satellite signal as a source of opportunity for passive coherent location. *IET Radar, Sonar Navigation*, 5(5):536–544, June 2011.

[46] K. Kauffman, J. Raquet, Y. Morton, and D. Garmatyuk. Real-time UWB-OFDM radar-based navigation in unknown terrain. *IEEE Transactions on Aerospace and Electronic Systems*, 49(3):1453–1466, 2013.

[47] A.M. Vegni and M. Biagi. An indoor localization algorithm in a small-cell LED-based lighting system. In *International Conference on Indoor Positioning and Indoor Navigation*, pages 1–7, November 2012.

[48] D. Zheng, G. Chen, and J.A. Farrell. Navigation using linear photo detector arrays. In *IEEE International Conference on Control Applications*, pages 533–538, August 2013.

[49] Z.M. Kassas. Collaborative opportunistic navigation. *IEEE Aerospace and Electronic Systems Magazine*, 28(6):38–41, 2013.

[50] J.J. Spilker, Jr. *Global Positioning System: Theory and Applications*, chapter 2: Overview of GPS Operation and Design, pages 57–119. American Institute of Aeronautics and Astronautics, Washington, D.C., 1996.

[51] H. Durrant-Whyte and T. Bailey. Simultaneous localization and mapping: part I. *IEEE Robotics & Automation Magazine*, 13(2):99–110, June 2006.

[52] T. Bailey and H. Durrant-Whyte. Simultaneous localization and mapping: part II. *IEEE Robotics & Automation Magazine*, 13(3):108–117, Sep. 2006.

[53] R.M. Faragher, C. Sarno, and M. Newman. Opportunistic radio SLAM for indoor navigation using smartphone sensors. In *IEEE/ION Position Location and Navigation Symposium*, pages 120–128, April 2012.

[54] A. Vu, A. Ramanandan, A. Chen, J.A. Farrell, and M. Barth. Real-time computer vision/DGPS-aided inertial navigation system for lane-level vehicle navigation. *IEEE Transactions on Intelligent Transportation Systems*, 13(2):899–913, June 2012.

[55] P. Corcoran, A. Winstanley, P. Mooney, and R. Middleton. Background foreground segmentation for SLAM. *IEEE Transactions on Intelligent Transportation Systems*, 12(4):1177–1183, December 2011.

[56] J.A. Barnes, A.R. Chi, R. Andrew, L.S. Cutler, D.J. Healey, D.B. Leeson, T.E. McGunigal, J.A. Mullen, W.L. Smith, R.L. Sydnor, R.F. Vessot, and G.M. Winkler. Characterization of frequency stability. *IEEE Transactions on Instrumentation and Measurement*, 20(2):105–120, May 1971.

[57] A.R. Thompson, J.M. Moran, and G.W. Swenson. *Interferometry and Synthesis in Radio Astronomy*. John Wiley & Sons, second edition, 2001.

[58] Y. Bar-Shalom, X.R. Li, and T. Kirubarajan. *Estimation with Applications to Tracking and Navigation*. John Wiley & Sons, New York, NY, 2002.

[59] R.G. Brown and P.Y.C. Hwang. *Introduction to Random Signals and Applied Kalman Filtering*. John Wiley & Sons, third edition, 2002.

[60] Z.M. Kassas. Numerical simulation of continuous-time stochastic dynamical systems with noisy measurements and their discrete-time equivalents. In *IEEE International Symposium on Computer-Aided Control System Design*, pages 1397–1402, September 2011.

[61] M.L. Psiaki and S. Mohiuddin. Modeling, analysis, and simulation of GPS carrier phase for spacecraft relative navigation. *Journal of Guidance, Control, and Dynamics*, 30(6):1628–1639, November-December 2007.

[62] Z.M. Kassas and R. Dunia. Discretization of MIMO systems with nonuniform input and output fractional time delays. In *IEEE Conference on Decision and Control*, pages 2541–2546, December 2006.

[63] Z.M. Kassas. Discretisation of continuous-time dynamic multi-input multi-output systems with non-uniform delays. *IET Proceedings on Control Theory & Applications*, 5(14):1637–1647, September 2011.

[64] E. Costa. Simulation of the effects of different urban environments on GPS performance using digital elevation models and building databases.

IEEE Transactions on Intelligent Transportation Systems, 12(3):819–829, September 2011.

[65] R. Hermann and A. Krener. Nonlinear controllability and observability. *IEEE Transactions on Automatic Control*, 22(5):728–740, October 1977.

[66] J.L. Casti. Recent developments and future perspectives in nonlinear system theory. *SIAM Review*, 24(3):301–331, July 1982.

[67] M. Anguelova. *Observability and Identifiability of nonlinear systems with applications in biology*. PhD thesis, Chalmers University Of Technology and Göteborg University, Sweden, 2007.

[68] W. Respondek. Geometry of static and dynamic feedback. In *Lecture Notes at the Summer School on Mathematical Control Theory*, Trieste, Italy, September 2001.

[69] W.J. Rugh. *Linear System Theory*. Prentice Hall, Upper Saddle River, NJ, second edition, 1996.

[70] D. Goshen-Meskin and I.Y. Bar-Itzhack. Observability analysis of piece-wise constant systems–part I: Theory. *IEEE Transactions on Aerospace and Electronic Systems*, 28(4):1056–1067, October 1992.

[71] F.M. Ham and R.G. Brown. Observability, eigenvalues, and Kalman filtering. *IEEE Transactions on Aerospace and Electronic Systems*, 19(2):269–273, March 1983.

[72] J. Andrade-Cetto and A. Sanfeliu. The effects of partial observability in SLAM. In *Proceedings of IEEE Internartional Conference on Robotics and Automation*, volume 1, pages 397–402, April 2004.

[73] J. Andrade-Cetto and A. Sanfeliu. The effects of partial observability when building fully correlated maps. *IEEE Transactions on Robotics*, 21(4):771–777, August 2005.

[74] T. Vida-Calleja, M. Bryson, S. Sukkarieh, A. Sanfeliu, and J. Andrade-Cetto. On the observability of bearing-only SLAM. In *Proceedings of IEEE Internartional Conference on Robotics and Automation*, volume 1, pages 4114–4118, April 2007.

[75] K.W. Lee, W.S. Wijesoma, and I.G. Javier. On the observability and observability analysis of SLAM. In *Proceedings of IEEE Internartional Conference on Intelligent Robots and Systems*, volume 1, pages 3569–3574, October 2006.

[76] Z. Wang and G. Dissanayake. Observability analysis of SLAM using Fisher information matrix. In *Proceedings of IEEE International Conference on Control, Automation, Robotics, and Vision*, volume 1, pages 1242–1247, December 2008.

[77] L.D.L. Perera, A. Melkumyan, and E. Nettleton. On the linear and nonlinear observability analysis of the SLAM problem. In *Proceedings of IEEE Internartional Conference on Mechatronics*, volume 1, pages 1–6, April 2009.

[78] L.D.L. Perera and E. Nettleton. On the nonlinear observability and the information form of the SLAM problem. In *Proceedings of IEEE Internartional Conference on Intelligent Robots and Systems*, volume 1, pages 2061–2068, October 2009.

[79] L.D.L. Perera and E. Nettleton. On stochastically observable directions of the estimation theoretic SLAM state space. In *Proceedings of IEEE/RSJ International Conference on Intelligent Robots and Systems*, pages 4324–4331, October 2010.

[80] L.D.L. Perera and E. Nettleton. Nonlinear observability of the centralized multi-vehicle SLAM problem. In *Proceedings of IEEE International Conference on Robotics and Automation*, pages 3171–3178, May 2010.

[81] G.P. Huang, A.I. Mourikis, and S.I. Roumeliotis. Analysis and improvement of the consistency of extended Kalman filter based SLAM. In *Proceedings of IEEE Internartional Conference on Robotics and Automation*, volume 1, pages 473–479, May 2008.

[82] G.P. Huang, A.I. Mourikis, and S.I. Roumeliotis. Observability-based rules for designing consistent EKF SLAM estimators. *International Journal of Robotics Research*, 29(5):502–528, April 2010.

[83] Z.M. Kassas and T.E. Humphreys. Observability analysis of opportunistic navigation with pseudorange measurements. In *Proceedings of AIAA Guidance, Navigation, and Control Conference*, volume 1, pages 1209–1220, August 2012.

[84] Z.M. Kassas and T.E. Humphreys. Observability analysis of collaborative opportunistic navigation with pseudorange measurements. *IEEE Transactions on Intelligent Transportation Systems*, 15(1):260–273, February 2014.

[85] Z.M. Kassas, J. Bhatti, and T.E. Humphreys. Receding horizon trajectory optimization for simultaneous signal landscape mapping and receiver localization. In *Proceedings of ION GNSS*, pages 1962–1969, September 2013.

[86] Z.M. Kassas and T.E. Humphreys. Receding horizon trajectory optimization in opportunistic navigation environments. *IEEE Transactions on Aerospace and Electronic Systems*, 2014. submitted.

[87] Z.M. Kassas and T.E. Humphreys. Observability and estimability of collaborative opportunistic navigation with pseudorange measurements. In *Proceedings of ION GNSS*, pages 621–630, September 2012.

[88] T.E. Humphreys, J. Bhatti, T. Pany, B. Ledvina, and B. O'Hanlon. Exploiting multicore technology in software-defined GNSS receivers. In *Proceedings of ION GNSS*, pages 326–338, September 2009.

[89] H.J.S. Feder, J.J. Leonard, and C.M. Smith. Adaptive mobile robot navigation and mapping. *International Journal of Robotics Research*, 18(7):650–668, July 1999.

[90] S.E. Hammel. *Optimal observer motion for bearings-only localization and tracking*. PhD thesis, University of Rhode Island, RI, USA, 1988.

[91] J.M. Passerieux and D. Van Cappel. Optimal observer maneuver for bearings-only tracking. *IEEE Transactions on Aerospace and Electronic Systems*, 34(3):777–788, July 1998.

[92] Y. Oshman and P. Davidson. Optimization of observer trajectories for bearings-only target localization. *IEEE Transactions on Aerospace and Electronic Systems*, 35(3):892–902, July 1999.

[93] E.W. Frew. Receding horizon control using random search for UAV navigation with passive, non-cooperative sensing. In *Proceedings of AIAA Guidance, Navigation, and Control Conference*, pages 5864–5876, August 2005.

[94] S. Ponda. Trajectory optimization for target localization using small unmanned aerial vehicles. Master's thesis, Massachusetts Institute of Technology, MA, USA, 2008.

[95] K. Zhou and S.I. Roumeliotis. Optimal motion strategies for range-only constrained multisensor target tracking. *IEEE Transactions on Robotics*, 24(5):1168–1185, October 2008.

[96] R.R. Pitre, X.R. Li, and R. Delbalzo. UAV route planning for joint search and track missions-an information-value approach. *IEEE Trans-*

actions on Aerospace and Electronic Systems, 48(3):2551–2565, July 2012.

[97] F. Bourgault, A.A. Makarenko, S.B. Williams, B. Grocholsky, and H.F. Durrant-Whyte. Information based adaptive robotic exploration. In *IEEE/RSJ International Conference on Intelligent Robots and Systems*, pages 540–545, October 2002.

[98] S. Huang, Z. Wang, and G. Dissanayake. Time optimal robot motion control in simultaneous localization and map building (SLAM) problem. In *IEEE/RSJ International Conference on Intelligent Robots and Systems*, volume 3, pages 3110–3115, September 2004.

[99] R. Sim and N. Roy. Global A-optimal robot exploration in SLAM. In *IEEE International Conference on Robotics and Automation*, pages 661–666, April 2005.

[100] S. Huang, N.M. Kwok, G. Dissanayake, Q.P. Ha, and F. Gu. Multi-step look-ahead trajectory planning in SLAM: possibility and necessity. In *IEEE International Conference on Robotics and Automation*, pages 1091–1096, April 2005.

[101] C. Leung, S. Huang, N. Kwok, and G. Dissanayake. Planning under uncertainty using model predictive control for information gathering. *Robotics and Autonomous Systems*, 54(11):898–910, November 2006.

[102] C. Leung, S. Huang, and G. Dissanayake. Active SLAM using model predictive control and attractor based exploration. In *Proceedings of IEEE/RSJ International Conference on Intelligent Robots and Systems*, pages 5026–5031, October 2006.

[103] G. Lidoris, K. Kuhnlenz, D. Wollherr, and M. Buss. Combined trajectory planning and gaze direction control for robotic exploration. In *IEEE International Conference on Robotics and Automation*, pages 4044–4049, April 2007.

[104] M. Bryson and S. Sukkarieh. Observability analysis and active control for airborne SLAM. *IEEE Transactions on Aerospace and Electronic Systems*, 44(1):261–280, January 2008.

[105] W.G. Cochran. Experiments for nonlinear functions. *Journal of the American Statistical Association*, 68(344):771–781, December 1973.

[106] H. Durrant-Whyte. *Multi Sensor Data Fusion*. 2001.

[107] T.M. Cover and J.A. Thomas. *Elements of Information Theory*. Wiley-Interscience, second edition, 2006.

[108] D. Uciński. *Optimal Measurement Methods for Distributed Parameter System Identification*. CRC Press, 2005.

[109] A.J. Davison and D.W. Murray. Simultaneous localization and map-building using active vision. *IEEE Transactions on Pattern Analysis and Machine Intelligence*, 24(7):865–880, 2002.

[110] A.J. Davison. Real-time simultaneous localisation and mapping with a single camera. In *IEEE International Conference on Computer Vision*, volume 2, pages 1403–1410, 2003.

[111] Z.M. Kassas, A. Arapostathis, and T.E. Humphreys. Greedy motion planning for simultaneous signal landscape mapping and receiver localization. *IEEE Journal of Selected Topics in Signal Processing*, 2014. submitted.

[112] M. Grant and S. Boyd. CVX: Matlab software for disciplined convex programming, version 2.0 beta. `http://cvxr.com/cvx`, September 2013.

[113] J.M. Mendel. *Lessons in Estimation Theory for Signal Processing, Communications, and Control*. Prentice Hall, second edition, 1995.

[114] S. Boyd and L. Vandenberghe. *Convex Optimization*. Cambridge University Press, 2004.

[115] R. Baldick. *Applied Optimization*. Cambridge University Press, 2006.

[116] J. Williams. *Information Theoretic Sensor Management*. PhD thesis, Massachusetts Institute of Technology, MA, USA, 2007.

[117] Z.M. Kassas and T.E. Humphreys. Motion planning for optimal information gathering in opportunistic navigation systems. In *Proceedings of AIAA Guidance, Navigation, and Control Conference*, August 2013. 551–4565.

[118] E. Koutsoupias and C. Papadimitriou. Worst-case equilibria. In *Proceedings of 16th Annual Symposium on Theoretical Aspects of Computer Science*, volume 1563, pages 404–413. March 1999.

[119] E. Kaplan and C. Hegarty. *Understanding* GPS*: Principles and Applications*. Artech House, second edition, 2005.

[120] T. Pany. *Navigation Signal Processing for* GNSS *Software Receivers*. Artech House, 2010.

[121] P. Misra and P. Enge. *Global Positioning System: Signals, Measurements, and Performance*. Ganga-Jamuna Press, second edition, 2010.

[122] Z.M. Kassas, J. Bhatti, and T.E. Humphreys. A graphical approach to GPS software-defined receiver implementation. In *Proceedings of IEEE Global Conference on Signal and Information Processing*, pages 1226–1229, December 2013.

[123] S.J. Julier and J.K. Uhlmann. A non-divergent estimation algorithm in the presence of unknown correlations. In *Proceedings of American Control Conference*, volume 4, pages 2369–2373, June 1997.

[124] G.O. Mutambara. *Decentralized Estimation and Control for Multisensor Systems*. CRC Press, 1998.

[125] Z.M. Kassas and T.E. Humphreys. The price of anarchy in active signal landscape map building. In *Proceedings of IEEE Global Conference on Signal and Information Processing*, pages 165–168, December 2013.

Vita

Zaher (Zak) Kassas received the Bachelor of Engineering (B.E.) degree in Electrical Engineering from The Lebanese American University in 2001. His B.E. Final Project aimed at extending the Global Positioning System (GPS) coverage through a power matching algorithm. He received the Master of Science (M.S.) degree in Electrical and Computer Engineering (ECE) from The Ohio State University in 2003. His M.S. Thesis designed nonlinear Bayesian filters for in-surveillance and out-of-surveillance mobile target tracking via unmanned aerial vehicles (UAVs). From 2004 through 2010 he was a research and development engineer with the Control Design and Dynamical Systems Simulation Research and Development Group at National Instruments Corp. From 2008 through 2011 he was an adjunct professor at Texas State University. He received the Master of Science in Engineering (M.S.E.) degree in Aerospace Engineering from The University of Texas at Austin (UT-Austin) in 2010. His M.S.E. Report designed $\mathcal{H}_2$ and $\mathcal{H}_\infty$ controllers for large segmented telescopes. He has been pursuing the Ph.D. studies at UT-Austin in ECE since 2010.

Permanent address: `zkassas@ieee.org`

This dissertation was typeset with LaTeX[†] by the author.

[†]LaTeX is a document preparation system developed by Leslie Lamport as a special version of Donald Knuth's TeX Program.